

INVESTIGATION OF TURBULENCE MODELS USED IN AUTOMOTIVE
INDUSTRY

A THESIS SUBMITTED TO
THE GRADUATE SCHOOL OF NATURAL AND APPLIED SCIENCES
OF
MIDDLE EAST TECHNICAL UNIVERSITY

BY

UMUR TAŞTAN

IN PARTIAL FULFILLMENT OF THE REQUIREMENTS
FOR
THE DEGREE OF MASTER OF SCIENCE
IN
MECHANICAL ENGINEERING

SEPTEMBER 2011

Approval of the Thesis:

**INVESTIGATION OF TURBULENCE MODELS USED IN AUTOMOTIVE
INDUSTRY**

Submitted by **UMUR TAŞTAN** in partial fulfillment of the requirements for the degree of **Master of Science in Mechanical Engineering Department, Middle East Technical University** by,

Prof. Dr. Canan Özgen _____
Dean, Graduate School of **Natural and Applied Sciences**

Prof. Dr. Suha Oral _____
Head of Department, **Mechanical Engineering**

Instr. Dr. Tahsin A. Çetinkaya _____
Supervisor, **Mechanical Engineering Dept., METU**

Examining Committee Members:

Prof. Dr. Kahraman Albayrak _____
Mechanical Engineering Dept., METU

Instr. Dr. Tahsin A. Çetinkaya _____
Mechanical Engineering Dept., METU

Prof. Dr. M. Haluk Aksel _____
Mechanical Engineering Dept., METU

Asst. Prof. Dr. M. Metin Yavuz _____
Mechanical Engineering Dept., METU

Dr. Tolga Köktürk _____
Mechanical Engineer, TARU A.Ş.

Date:

15.09.2011

I hereby declare that all information in this document has been obtained and presented in accordance with academic rules and ethical conduct. I also declare that, as required by these rules and conduct, I have fully cited and referenced all material and results that are not original to this work.

Name, Last name : Umur Taştan

Signature :

ABSTRACT

INVESTIGATION OF TURBULENCE MODELS USED IN AUTOMOTIVE INDUSTRY

Taştan, Umur

M.Sc., Department of Mechanical Engineering

Supervisor : Instr. Dr. Tahsin A. Çetinkaya

September 2011, 134 pages

In this study; reliability and performance of turbulence models used in CFD softwares to determine the aerodynamics of passenger cars, are tested and compared.

In the analyses, drag forces acting on the car, pressure and velocity distributions and wake flow patterns are determined by using several turbulence models with a commercial software Fluent. Calculated results compared to the experimental results given in the literature.

It is observed that, turbulence models give relatively reliable results for determining aerodynamic properties of the model car. Among the turbulence models, RNG $k-\epsilon$ and standard $k-\omega$ models stand one step ahead of the other models according to results.

Keywords: Road vehicle aerodynamics, turbulence, turbulence modelling, CFD

ÖZ

OTOMOBİL ENDÜSTRİSİNDE KULLANILAN TÜRBÜLANS MODELLERİNİN ARAŞTIRILMASI

Taştan, Umur

Yüksek Lisans, Makina Mühendisliği Bölümü

Tez Yöneticisi : Öğr. Gör. Dr. Tahsin A. Çetinkaya

Eylül 2011, 134 sayfa

Bu çalışmada binek otomobillerin CFD metodlarıyla aerodinamik olarak incelenmesinde kullanılan türbülans modellerinin güvenilirliği incelenmiş ve performansları test edilmiştir.

Yapılan simülasyonlarda araca ait sürüklenme kuvvetleri, yüzey basınç dağılımları, hız dağılımları ve ardiz oluşumları çeşitli türbülans modelleri kullanılarak ticari bir yazılım olan Fluent ile belirlenmiş ve bulunan sonuçlar literatürde bulunan deneysel verilerle karşılaştırılmıştır.

Türbülans modellerinin bu çalışmada incelenen araç modeli için güvenilir sonuçlar verdiği, RNG $k-\varepsilon$ ve standard $k-\omega$ modellerinin ise diğer modellere göre bir adım öne çıktığı gözlemlenmiştir.

Anahtar kelimeler: Otomobil aerodinamiği, türbülans, türbülans modellemesi, HAD

To My Family

ACKNOWLEDGEMENTS

The author wishes to express his appreciation to his supervisor Dr. Tahsin Çetinkaya for their guidance, advice, criticism, encouragements and insight throughout the study.

The author would like to thank Mr. Kerem Taştan for his guidance, suggestions and comments.

The author would also like to thank Mr. Murat İşevcan for his help during the CAD modelling.

The help and encouragement of all friends and relatives throughout the research are particularly appreciated.

The author would like to thank Ms. Seçil Özer, his nearest and dearest, for her love, faith and understanding.

Finally, the author would like to thank and dedicate this thesis to his family for their endless support and love.

TABLE OF CONTENTS

ABSTRACT	iv
ÖZ	v
ACKNOWLEDGEMENTS	vii
TABLE OF CONTENTS	viii
LIST OF TABLES	xi
LIST OF FIGURES	xiii
LIST OF SYMBOLS	xviii
LIST OF ABBREVIATIONS	xxii
CHAPTERS	
1. INTRODUCTION	1
2. LITERATURE SURVEY	5
2.1 Literature Reviews	5
2.2 Assessment of Some Turbulence Models	15
2.2.1 Spalart-Allmaras Model	15
2.2.2 Standard $k-\varepsilon$ Model	15
2.2.3 RNG $k-\varepsilon$ Model	15
2.2.4 Realizable $k-\varepsilon$ Model	16
2.2.5 Standard $k-\omega$ Model	16
2.2.6 SST $k-\omega$ Model	16
2.2.7 Reynolds Stress Model	16

3. AERODYNAMICS OF ROAD VEHICLES	17
3.1 Mechanics of Air Flow Around a Car	17
3.2 Pressure Distribution on a Car	24
3.3 Aerodynamic Forces	26
3.3.1 Drag Force and Drag Coefficient	26
3.3.1.1 Effect of Friction on Drag	27
3.3.1.2 Effect of Pressure on Drag	28
3.3.1.3 Effect of Wheels on Drag	30
3.3.1.4 Effect of Engine Cooling System on Drag	31
3.3.1.5 Effect of Trailing Vortices on Drag	32
3.3.1.6 Effect of Drag on Fuel Consumption	32
3.3.1.7 Effect of Drag on Acceleration	33
3.3.1.8 Effect of Drag on Maximum Speed	34
3.3.2 Lift Force and Lift Coefficient	34
3.3.3 Side Force and Side Force Coefficient	35
4. MATHEMEATICAL FORMULATION	36
4.1 General Equations	36
4.1.1 Continuity Equation	36
4.1.2 Momentum Equation	37
4.1.3 Navier-Stokes Equations	37
4.2 Finite Volume Method and Discretization Methods	40
4.2.1 Numerical Solution of the Navier-Stokes Equations	42
5. TURBULENCE AND ITS MODELING	45
5.1 Time-Averaged Equations for Turbulent Flows	50
5.2 Turbulence Modeling	55
5.2.1 Mixing Length Model	56
5.2.2 Standard k - ε Model	58
5.2.3 RNG k - ε Model	61
5.2.4 Realizable k - ε Model	62
5.2.5 Standard k - ω Model	63
5.2.6 SST k - ω Model	64
5.2.7 Spalart–Allmaras Model	65

5.2.8	Reynolds Stress Model	67
5.2.9	Direct Numerical and Large Eddy Simulations	69
5.3	Near Wall Treatment	70
6.	CFD SIMULATIONS	73
6.1	Vehicle Model	73
6.2	Softwares Used in the Study	76
6.2.1	Rhinoceros	77
6.2.2	Catia	77
6.2.3	Gambit	77
6.2.4	Tgrid	77
6.2.5	Fluent	77
6.3	The Domain	78
6.4	Boundary Conditions and Settings	81
6.5	Results and Discussion	84
7.	CONCLUSION AND RECOMMENDATIONS	115
7.1	Conclusion	115
7.2	Future Work Recommendations	117
	REFERENCES	118
APPENDICIES		
A.	AHMED BODY STUDIES	123
B.	PRELIMINARY STUDIES	129
C.	EXPERIMENTAL LITERATURE RESULTS OF BMW MODEL CAR	132

LIST OF TABLES

TABLES

Table 2.1 Ahmed Body 35° Drag Results of Liu and Moser	8
Table 2.2 Ahmed Body 35° Drag Results of Durand et al.	8
Table 2.3 Ahmed Body Drag Results of Barbone et al.	9
Table 2.4 GTS Model Drag Results	10
Table 2.5 Ahmed Body Drag Results of Örselli	12
Table 2.6 MIRA Model Drag Results of Örselli	12
Table 3.1 Aerodynamic forces and moments	26
Table 3.2 Share of surface friction drag on total drag	28
Table 3.3 Share of form drag on total drag	29
Table 5.1 Mixing lengths for some two-dimensional simple flows	57
Table 6.1 Settings for the boundary conditions	82
Table 6.2 Relaxation factors	84
Table 6.3 C_D values for $V=5$ m/s ($Re=95472$)	84
Table 6.4 C_D values for $V=9$ m/s ($Re=171850$)	85
Table 6.5 C_D values for $V=13$ m/s ($Re=248228$)	85
Table 6.6 C_D values for $V=17$ m/s ($Re=324606$)	85

Table 6.7 C_D values for $V=21$ m/s ($Re=400984$)	86
Table 6.8 C_D values for $V=25$ m/s ($Re=477362$)	86
Table 6.9 C_p values obtained with various turbulence models (ports 1-5)	89
Table 6.10 C_p values obtained with various turbulence models (ports 6-11)	89
Table 6.11 Turbulence model evaluation based on computational efforts	110
Table A.1 Settings for the boundary conditions	125
Table A.2 Drag Results of Ahmed Body	125
Table A.3 C_D Results for all angles	127
Table B.1 Setting for preliminary studies	131
Table B.2 Drag results for different cases	131
Table C.1 Pressure values measured on pressure ports 1-4	132
Table C.2 Pressure values measured on pressure ports 5-8	132
Table C.3 Pressure values measured on pressure ports 9-11	133
Table C.4 Drag results for different velocities	133
Table C.5 Drag results for different velocities-cont.	134

LIST OF FIGURES

FIGURES

Figure 1.1 Effect of drag coefficient on fuel consumption	2
Figure 1.2 Properties affected by aerodynamic characteristics	2
Figure 2.1 Ahmed Body	6
Figure 2.2 Vortex systems in the wake of Ahmed Body	6
Figure 2.3 Ahmed Body drag results for various configurations	7
Figure 2.4 GTS Model	10
Figure 2.5 GTD Pickup Truck Model (experimental and CFD)	11
Figure 2.6 Drag Forces for GTD Model	11
Figure 2.7 TE 54 Open circuit wind tunnel.....	12
Figure 2.8 Variation of C_p with Reynolds Number (ports 1-4)	13
Figure 2.9 Variation of C_p with Reynolds Number (ports 5-8)	13
Figure 2.10 Variation of C_p with Reynolds Number (ports 9-11)	13
Figure 2.11 Variation of drag coefficient with Reynolds number	14
Figure 2.12 Variation of lift coefficient with Reynolds number	14
Figure 3.1 Streamtubes flowing over a car	18
Figure 3.2 Pressure and velocity variation on the upper profile of a moving car	19
Figure 3.3 Boundary layer velocity profile	19
Figure 3.4 Boundary layer development on a flat plate	20
Figure 3.5 Adverse pressure gradients and flow separation	21
Figure 3.6 Separation under adverse pressure gradient	21

Figure 3.7 Comparison of laminar and turbulent boundary layers under adverse pressure gradient (a) Laminar (b) Turbulent	22
Figure 3.8 Local separations inside bubble	23
Figure 3.9 Pressure distribution along the centerline of a car	24
Figure 3.10 Vortex systems in the wake of a car	25
Figure 3.11 Effect of separation on dirt accumulation at the rear	25
Figure 3.12 Aerodynamic forces and moments	26
Figure 3.13 Drag components acting on an object	27
Figure 3.14 Effect of viscosity (a) Theoretical Inviscid Flow (b) Real Viscous Flow	30
Figure 3.15 Air flow recirculation in a wheel well	31
Figure 3.16 Alternative radiator arrangements for reducing the drag due to cooling system	31
Figure 3.17 The three-dimensional nature of the flow around a car	32
Figure 3.18 Influence of drag reduction on fuel saving	33
Figure 3.19 Effect of drag coefficient on acceleration	33
Figure 3.20 Total power against speed for various C_D values	34
Figure 3.21 Aerodynamic forces and moments and the Definition of Yaw Angle (β)	35
Figure 4.1 2-D control volume in cartesian coordinates	41
Figure 4.2 Diagram of projection method	44
Figure 5.1 Leonardo da Vinci's sketch of turbulence	46
Figure 5.2 Two-dimensional image of an axisymmetric water jet	47
Figure 5.3 Turbulent eruption of Klyuchevskoy volcano, Russia	47
Figure 5.4 Turbulent clouds over Carlesbad, New Mexico	48
Figure 5.5 Turbulent blood flow in a stenosed, or narrowed, carotid artery	48
Figure 5.6 Visualization of flow over VW Beetle	48
Figure 5.7 Typical point velocity measurement in turbulent flow	49

Figure 5.8 Subdivisions of near wall region	71
Figure 6.1 CAD model of the car (front perspective view)	73
Figure 6.2 CAD model of the car (rear perspective view)	74
Figure 6.3 CAD model of the car (top view)	74
Figure 6.4 CAD model of the car (front view)	75
Figure 6.5 CAD model of the car (side view)	75
Figure 6.6 Software structure of the study	76
Figure 6.7 Computational domain	78
Figure 6.8 The grid on the car surface	79
Figure 6.9 The grid on the symmetry plane and ground surface	80
Figure 6.10 Prismatic elements on the symmetry plane	80
Figure 6.11 Defined boundary conditions	81
Figure 6.12 Variation of drag coefficient with Reynolds number	87
Figure 6.13 Pressure port locations on the symmetry plane of the car	89
Figure 6.14 Variation of C_p with pressure ports.....	90
Figure 6.15 Pressure contours on the coachwork of a car, front perspective view (RNG $k-\varepsilon$ model)	91
Figure 6.16 Pressure contours on the coachwork of a car, top view (RNG $k-\varepsilon$ model)	92
Figure 6.17 Velocity distribution on the symmetry plane of the car (RNG $k-\varepsilon$ model)	93
Figure 6.18 Streamlines at the symmetry plane (Realizable $k-\varepsilon$ model)	93
Figure 6.19 Streamlines at the symmetry plane (RNG $k-\varepsilon$ model)	94
Figure 6.20 Streamlines at the symmetry plane (Reynolds stress model)	94
Figure 6.21 Streamlines at the symmetry plane (Spalart-Allmaras model)	95
Figure 6.22 Streamlines at the symmetry plane (SST $k-\omega$ model)	95
Figure 6.23 Streamlines at the symmetry plane (Standard $k-\varepsilon$ model)	96
Figure 6.24 Streamlines at the symmetry plane (Standard $k-\omega$ model)	96

Figure A.4 Variation of drag coefficient with slant angle	126
Figure A.5 Attached flow on the slant predicted by standard $k-\omega$	127
Figure A.6 Separated flow on the slant predicted by RSM	128
Figure A.7 Wake flow formation obtained with standard $k-\omega$ model	129
Figure A.8 Turbulence models predictions of wake flow at the critical slant angle 30°	129
Figure B.1 MIRA Model	130

LIST OF SYMBOLS

C_D	Drag coefficient
C_S^*	Slant part pressure drag coefficient
C_B^*	Base pressure drag coefficient
C_K^*	Forebody pressure drag coefficient
C_R^*	Friction drag coefficient
C_W	Total drag coefficient
φ	Ahmed body slant angle, [°]
$C_{D,p}$	Form drag coefficient
$C_{D,f}$	Friction drag coefficient
Re	Reynolds number
ΔP_{avg}	Average pressure difference, [N/m ²]
C_P	Pressure coefficient
C_L	Lift coefficient
C_{MP}	Pitching moment coefficient
ρ	Density of the fluid, [kg/m ³]
V_∞	Free stream velocity, [m/s]
P_∞	Free stream pressure, [N/m ²]
δ	Boundary layer thickness, [m]
x_{cr}	Position of the completed transition, [m]
μ	Dynamic viscosity of the fluid, [kg/m.s]
L	Characteristic length, [m]

ℓ_m	Mixing length, [m]
F_D	Drag force, [N]
F_L	Lift force, [N]
F_S	Side force, [N]
M_R	Rolling moment, [N.m]
M_Y	Yawing moment, [N.m]
M_P	Pitching moment, [N.m]
A	Area, [m ²]
ν	Kinematic viscosity of the fluid, [m ² /s ²]
ω	Turbulent kinetic energy specific dissipation rate, [1/s]
C_S	Side force coefficient
β	Yaw angle, [°]
R_{ij}	Reynolds stress tensor, [N/m ²]
δ_{ij}	Kronecker delta
I	Turbulence intensity of the wind tunnel, [%]
\vec{u}	Velocity vector, [m/s]
u	x component of velocity vector, [m/s]
v	y component of velocity vector, [m/s]
w	z component of velocity vector, [m/s]
$\tau_{xx}, \tau_{yy}, \tau_{zz}$	Normal stresses, [N/m ²]
$\tau_{xy}, \tau_{yz}, \tau_{xz}$	Shear stresses, [N/m ²]
S	Source term
e_{xx}, e_{yy}, e_{zz}	Linear elongating deformation components
e_{xy}, e_{yz}, e_{xz}	Linear shearing deformation components
λ	Second viscosity constant

ϕ	Arbitrary variable
\vec{r}	Displacement vector, [m]
Γ	Diffusion coefficient
$\sigma_k, \sigma_\epsilon$	Turbulence model constants
\vec{S}_f	Surface vector at all faces of the control volume
N_f	Number of nodes on the face
p^*	Guessed value for pressure, [N/m ²]
u^*	Guessed value for velocity, [m/s]
\vec{U}	Mean velocity vector, [m/s]
\vec{u}'	Fluctuating velocity vector, [m/s]
U	x component of mean velocity, [m/s]
V	y component of mean velocity, [m/s]
W	z component of mean velocity, [m/s]
u'	x component of fluctuating velocity, [m/s]
v'	y component of fluctuating velocity, [m/s]
w'	z component of fluctuating velocity, [m/s]
μ_t	Turbulent viscosity of the fluid, [kg/m.s]
σ_t	Prandtl/Schmidt number
Γ_t	Turbulent diffusivity
ν_t	Kinematic turbulent viscosity, [m ² /s ²]
v	Velocity scale, [m/s]
ℓ	Length scale, [m]
κ	von Karman's constant
y^+	The measure of physical distance of the wall adjacent cell centroid, [m]
k	Turbulent kinetic energy, [m ² /s ²]

K	Mean kinetic energy, [m ² /s ²]
$k(t)$	Instantaneous kinetic energy, [m ² /s ²]
ε	The rate of dissipation per unit mass, [m ² /s ³]
μ_{eff}	Effective viscosity, [kg/m.s]
$C_1, C_2, C_{1\varepsilon}, C_{2\varepsilon}, C_{3\varepsilon}$	Turbulence model constants

LIST OF ABBREVIATIONS

CFD	Computational Fluid Dynamics
LES	Large Eddy Simulation
DNS	Direct Numerical Simulation
RSM	Reynolds Stress Model
UDF	User Defined Function
MIRA	Motor Industrial Research Association
RANS	Reynolds-Averaged Navier-Stokes
RNG	Renormalization Group
SST	Shear Stress Transport
PC	Personal Computer
CPU	Central Processing Unit
DDR	Double Data Rated
RAM	Random Access Memory

CHAPTER 1

INTRODUCTION

Automotive industry has become a competitive sector over the years. Manufacturing companies want from their cars to have high qualities in terms of performance, safety, comfort and economy. Therefore, companies allocate huge budgets for research and development studies.

As it is known, fossil fuels have been running out throughout the world. Most of the fossil fuels are consumed by the automobiles in which internal combustion engines are used. Hence effective usage of fuel in automobiles is a very important subject. There are two ways to achieve this goal, one is to increase the efficiency of the engine and the other one is to reduce the resisting forces acting on cars when they are travelling.

Resisting forces acting on cars can be classified in two groups namely; body forces and external forces. Body forces are related with the mass or change in the velocity of the car. On the other hand external forces are the forces that provide or resist the movement of the car and they are not directly related to the mass of the car. Since the forces resisting the movement of the car determine the energy requiring for the motion, they also affect the fuel consumption.

One of the most important resistant force acting on cars is aerodynamic drag force. A passenger car travelling at a speed of 100 km/h spends 60% of its power to overcome aerodynamic drag [1].

Effect of aerodynamic drag force on fuel consumption is shown in Figure 1.1. In this figure, C_D represents the drag coefficient.

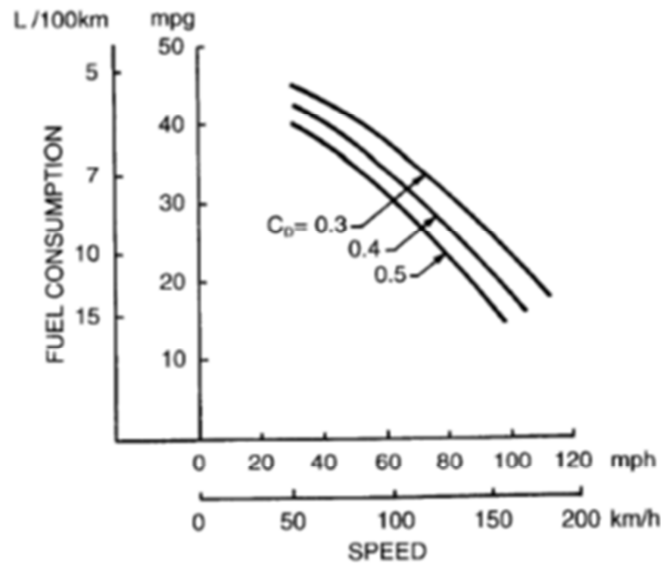


Figure 1.1 Effect of drag coefficient on fuel consumption [2]

Aerodynamic characteristics affect also safety, visibility, comfort and performance of cars beside fuel consumption (Figure 1.2). Therefore determination of aerodynamic characteristics is an important matter.



Figure 1.2 Properties affected by aerodynamic characteristics [22]

Road and wind tunnel tests are conducted to determine the aerodynamic characteristics of cars. Wind tunnel tests are cheaper and easily applicable because in wind tunnel tests, it is possible to use smaller scale models. Full scale models increase the cost of the wind tunnel tests. Although road tests represent the

environment in which car will be used successfully and give more realistic results, wind tunnel tests are often used to determine the aerodynamic characteristics of cars since it is difficult to make any generalizations for different ambient conditions in road tests.

In the last decade, a huge progress in the area of computational fluid dynamics (CFD) and its computational applications have been made. Most of the car manufacturing companies use CFD related package softwares especially in the pre-design stage. These softwares are widely used since they are cheap and fast even for the solution of very complex systems. They also give an opportunity to the designer to see the faults before the production stage without any production cost.

CFD methods need a turbulence model to solve turbulent flows. A lot of turbulence models have been developed and integrated in CFD softwares. Since the chosen turbulence models affect the results directly, the choice of turbulence models should be appropriate for the system under consideration.

Turbulence models can be classified into three categories depending on complexity; Direct Numerical Simulation (DNS), Large Eddy Simulation (LES) and Reynolds Averaged Navier-Stokes (RANS) models. Among those, only DNS can be used to calculate the flow without a numerical model. But this requires huge computational resources. LES assumes that most of the flow energy is contained in the large eddies and these eddies are computed, and small eddies are modeled. RANS models calculate mean flow parameters instead of instantaneous flow parameters. Averaging process is used to derive mean flow equations. With this process some information relevant to turbulence fluctuations is lost. This loss of information appears itself as Reynolds stresses in the mean flow equations and they need to be represented numerically [3].

Flow near a wall can precipitate extra problems for turbulence models. This is because near a wall the velocity profiles and Reynolds stresses change quickly, thus one requires a very fine computational grid to resolve these changes. In order not to use such a fine grid, wall functions are utilized to link the near wall region and fully turbulent region [3].

In this study, firstly fundamentals of aerodynamics and aerodynamic characteristics of passenger cars are mentioned. Then properties of turbulent flows and turbulence models are discussed. Lastly, in order to test the reliability of turbulence models and to compare the performances of them; an aerodynamic CFD analysis of BMW model car is made. In the CFD simulations, the wind tunnel tests of Aka [4] which was made on the same car model, was simulated with using several turbulence models. After all, computational and experimental results are compared.

Analyses in this study were made with Fluent, a CFD software developed by ANSYS. Geometry of the model car was created with Rhinoceros and Catia softwares. Computational mesh was generated with Gambit and Tgrid softwares. At the end; streamlines, velocity and pressure distributions, velocity vectors, drag and pressure coefficients were obtained by using CFD-Post software.

CHAPTER 2

LITERATURE SURVEY

It was the 1960's, after the World War II, when the aerodynamic characteristics of road vehicles were begun to be studied more intensively. At this period with wind tunnel tests, experimental studies became more of an issue when determining aerodynamic properties of road vehicles. The first CFD studies started in 1980's with the progress of computer technology and a new era started in automobile aerodynamics. At present time there is a continuous development in road vehicles aerodynamics with both wind tunnel tests and CFD applications.

2.1 Literature Reviews

Ahmed et al. [5] developed a simplified car model called Ahmed Body (Figure 2.1) and investigated the effect of slant angle on drag force experimentally. Drag coefficients were found as 0.231, 0.23 and 0.378 with the slant angles of 5° , 12.5° and 30° respectively. It was shown that 85% of total drag was formed due to pressure drag and rest of the drag force was due to friction drag. They also studied the wake flow region behind the car and two horseshoe vortices (Figure 2.2) that the strength of which depend on slant angle were observed. Side vortices formed on the side of the car also contributed to wake vortices. Because of the simplicity of the geometry, Ahmed Body has been used in lots of experimental and computational studies and it has become a reference car model. Drag results for various configurations of Ahmed Body are shown in Figure 2.3.

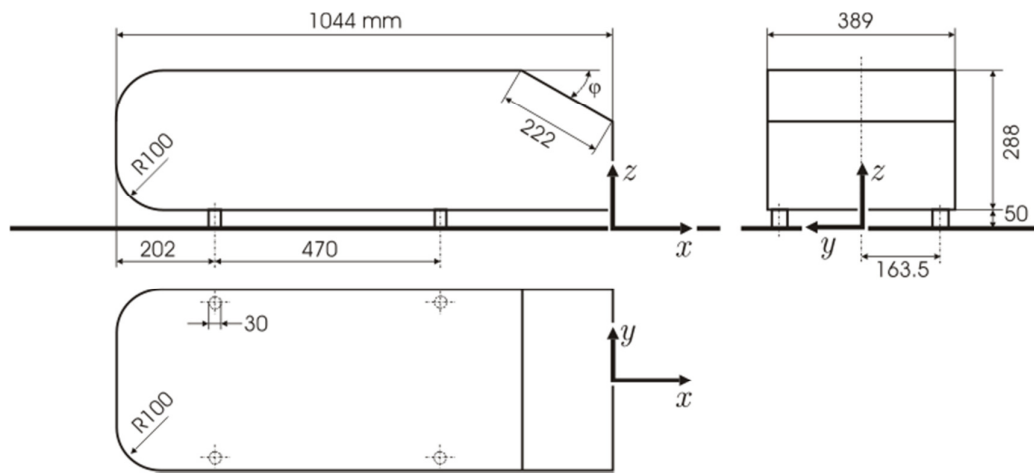


Figure 2.1 Ahmed Body [3]

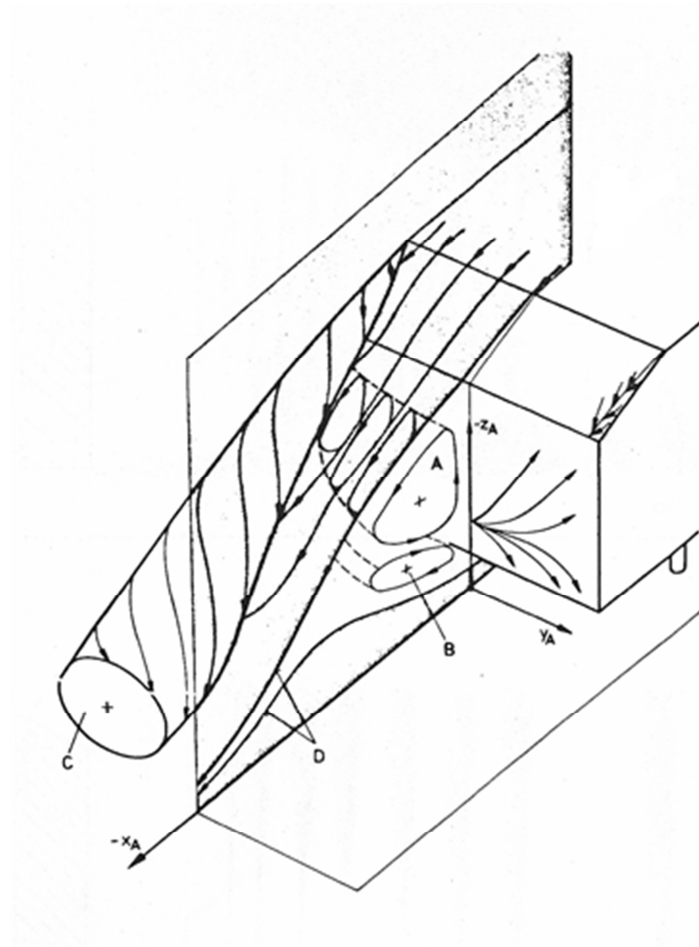


Figure 2.2 Vortex systems in the wake of Ahmed Body [5]

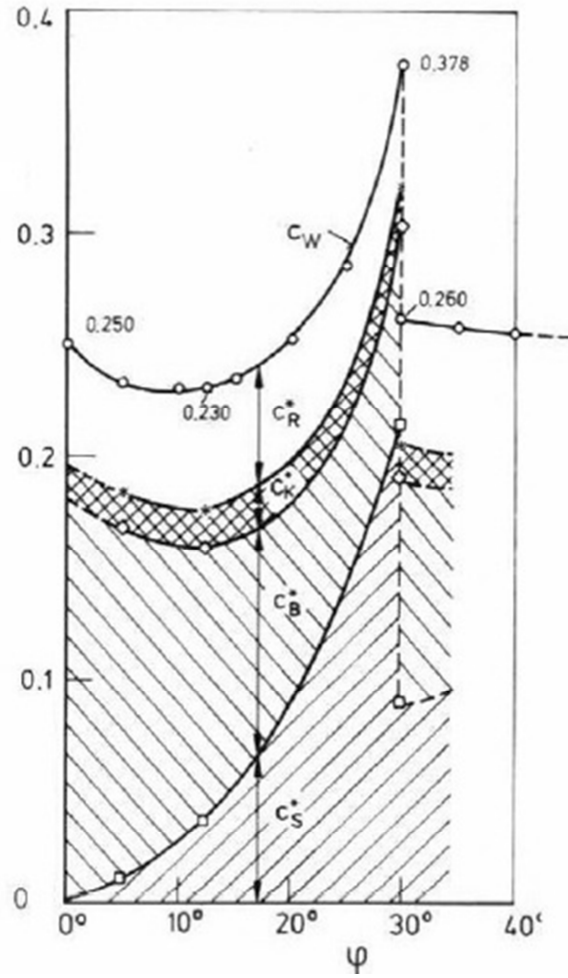


Figure 2.3 Ahmed Body drag results for various configurations [5]

where,

C_S^* : Slant part pressure drag coefficient

C_B^* : Base pressure drag coefficient

C_K^* : Fore-body pressure drag coefficient

C_R^* : Friction drag coefficient

C_W : Total drag coefficient

Liu and Moser [6] studied the Ahmed Body with 35° slant angle by using Reynolds Averaged Navier-Stokes Equations (RANS) based turbulence models; Standard $k-\varepsilon$, Shear Stress Transport (SST) $k-\omega$, Durbin's $k-\varepsilon-\nu^2$ and Reynolds Stress Model (RSM). They showed that $k-\varepsilon-\nu^2$ model gave better results when compared to the other three models in terms of the prediction of drag coefficient and wake flow. Drag coefficients are shown in Table 2.1.

Table 2.1 Ahmed Body 35° Drag Results of Liu and Moser [6]

	C_D	Error
Ahmed [5]	0.260	-
Standard $k-\varepsilon$	0.242	-6.8%
$k-\varepsilon-\nu^2$	0.264	1.5%
RSM	0.282	8.5%
SST $k-\omega$	0.241	-7.3%

Similar to the study of Liu and Moser, Durand et al. [7] investigated the Ahmed Body with 35° slant angle and compared the results obtained with standard $k-\varepsilon$, SST $k-\omega$ and RSM. Drag coefficients are presented in Table 2.2. In computational calculation, the effects of first and second order discretization schemes were also investigated and second order discretization was found to give more accurate results.

Table 2.2 Ahmed Body 35° Drag Results of Durand et al. [7]

Turb. Model	Standard $k-\varepsilon$	SST $k-\omega$	RSM	Experiment (without stilts)
C_D	0.228	0.240	0.199	0.234
Error %	-2.6	2.5	-15	-

Barbone et al. [8] analysed Ahmed Body with slant angles 0°, 25° and 35° by using standard $k-\varepsilon$ and RSM turbulence models. Reasonably fine mesh with 3.5 million elements was used. Drag coefficients of Ahmed Body with 2.78×10^6 Reynolds number are presented in Table 2.3.

Table 2.3 Ahmed Body Drag Results of Barbone et al. [8]

Slant Angle	Standard $k-\varepsilon$	RSM	Experiment
0°	0.313	0.304	0.250
25°	0.310	0.293	0.285
35°	0.284	0.298	0.257

Han [9], one of the first CFD researchers on automobile aerodynamics, used standard linear $k-\varepsilon$ turbulence model to calculate drag coefficients of Ahmed Body with different slant angles. For slant angles between 0° and 20° calculated drag coefficients were higher than measured ones about 30%. Besides, the separation that Ahmed et al. [5] observed could not be calculated. The reason for the difference between CFD and experimental studies may be the turbulence model. Because by Wilcox [3], it was stated that linear $k-\varepsilon$ turbulence model might give wrong results for the flows with adverse pressure gradients and separations.

Han et al. [10] found drag coefficients of three different car model (square rear surface, rear surface with long and short ramps). They compared standard $k-\varepsilon$ and RNG $k-\varepsilon$ models and showed that RNG $k-\varepsilon$ model was more reliable.

Perzon et al. [11] compared the results obtained with StarCD and Fluent softwares by using standard $k-\varepsilon$, RNG $k-\varepsilon$, non-linear eddy viscosity and Reynolds stress model with experimental results of a model of tractor and trailer having a geometric scale of 0.3. It was shown that RNG $k-\varepsilon$ and non-linear eddy viscosity models predicted stagnation pressures and drag coefficient more accurately when compared with other models. They suggested use of a finer mesh could increase the accuracy of the results.

Makowski and Kim [12] tested a model similar to an automobile in Fluent software by using standard, realizable and RNG $k-\varepsilon$ turbulence models with non-equilibrium wall functions. At the end of the study, it was indicated that although RNG $k-\varepsilon$ gave better results, it required more CPU time.

Şahin [13] simulated the flow around a bus model called GTS (Figure 2.3) with Star-CCM+ CFD software. Streamlines, velocity vectors and velocity and pressure

distributions were investigated and compared with experimental results given in the literature. According to results it was shown that $k-\omega$ turbulence models were more favourable to $k-\varepsilon$ models for the investigation of aerodynamics of heavy vehicles such as buses. Results are given in Table 2.4.

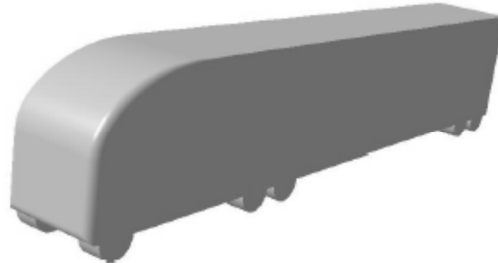


Figure 2.4 GTS Model [13]

Table 2.4 GTS Model Drag Results [13]

	RNG $k-\varepsilon$	Standard $k-\varepsilon$	Standard $k-\omega$	SST $k-\omega$
Pressure drag coefficient, $C_{D,p}$	0.416	0.426	0.407	0.407
Friction drag coefficient, $C_{D,f}$	6.2×10^{-4}	0.003	-5.0×10^{-5}	-5.02×10^{-5}
Overall drag coefficient, C_D	0.417	0.429	0.407	0.407
Experimental results	0.35	0.35	0.35	0.35
Error (%)	19.1	22.6	16.4	16.4

İnce [14] determined the aerodynamic characteristics of a pickup truck by both wind tunnel test and CFD simulation with Fluent software. In CFD simulation standard $k-\varepsilon$, realizable $k-\varepsilon$, RNG $k-\varepsilon$, standard $k-\omega$, SST $k-\omega$ and RSM turbulence models were used to determine drag coefficient, velocity and pressure distributions on the vehicle and the reliability of these turbulence models was tested. It was stated that most of these turbulence models were suitable for this kind of road vehicle analysis but for low velocities RSM and for high velocities standard $k-\varepsilon$ turbulence models were advised since they gave more accurate results. Some suggestions were also made to improve the aerodynamic properties of vehicle shown in Figure 2.5. Drag coefficients obtained with different turbulence models are presented in Figure 2.6.

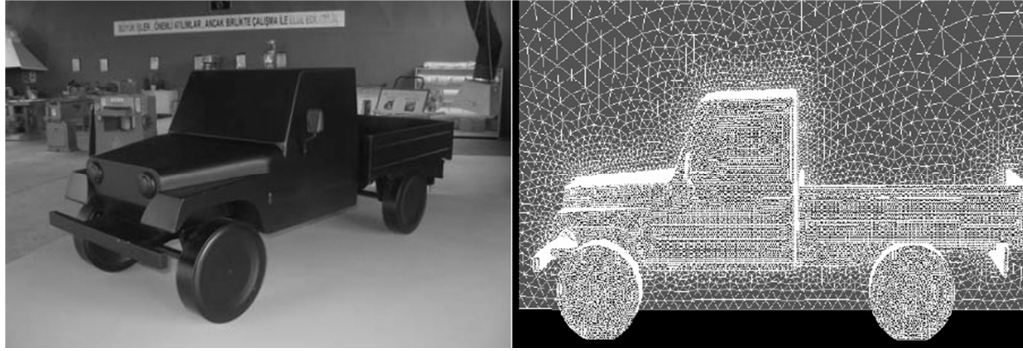


Figure 2.5 GTD Pickup Truck Model (experimental and CFD) [14]

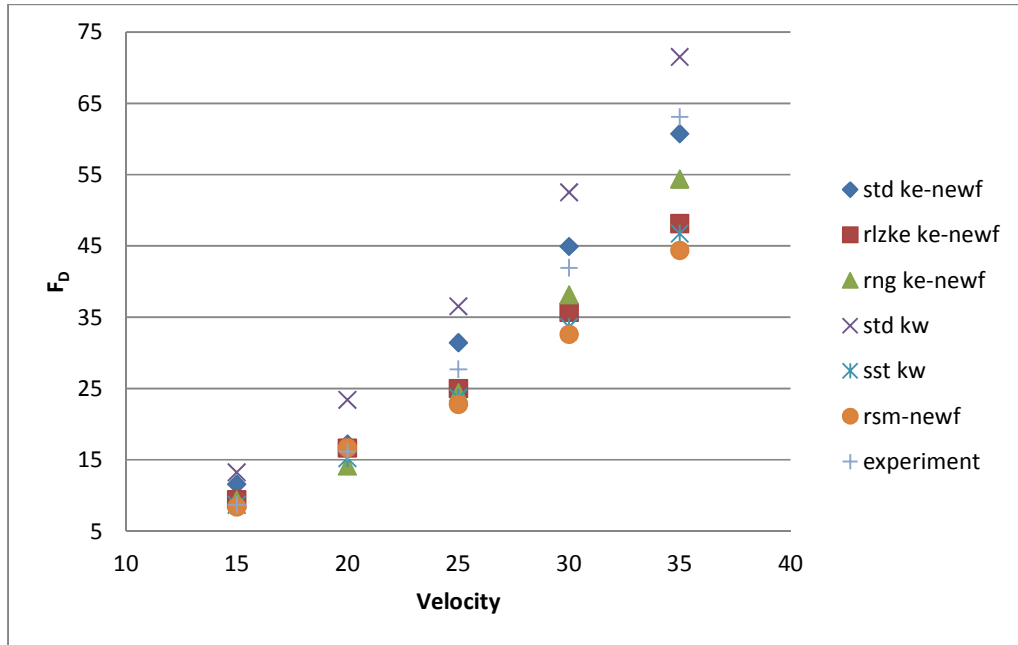


Figure 2.6 Drag forces for GTD Model [14]

Örselli [3] conducted CFD simulations for two different simplified car models known as Ahmed Body and MIRA and tested the performance of three different turbulence models; realizable $k-\varepsilon$, SST $k-\omega$ and RSM. The most reliable results were obtained with RSM model. It was shown that although RSM model required much more CPU time and memory, there was no big difference between RSM and realizable $k-\varepsilon$ models and hence, analyses made with realizable $k-\varepsilon$ turbulence model at the continuation of the study. Drag coefficients are given in Table 2.5 and Table 2.6.

Table 2.5 Ahmed Body Drag Results of Örselli [3]

25° Ahmed	realizable $k-\varepsilon$	SST $k-\omega$	RSM	Exp [5]
Body	C_D	C_D	C_D	C_D
front	0.041	0.034	0.034	0.020
back	0.069	0.080	0.076	0.070
slant	0.115	0.110	0.109	0.140
total	0.289	0.292	0.287	0.285
Error (%)	1.4	2.4	0.7	-

Table 2.6 MIRA Model Drag Results of Örselli [3]

MIRA	Turbulence Model				Exp [47]
	realizable $k-\varepsilon$	realizable $k-\varepsilon$	SST $k-\omega$	RSM	
	first order	second order			
C_D	0.393	0.307	0.309	0.291	0.295
Error (%)	33	4.0	4.7	-1.3	-

Aka [4] determined the aerodynamic characteristics of a 1/16 scaled BMW car model by wind tunnel tests. Drag and lift coefficients, pressure distributions and pitching moments were founded. The wind tunnel which experiments were conducted is given in Figure 2.7 and results are given in Figures 2.8 to 2.12.

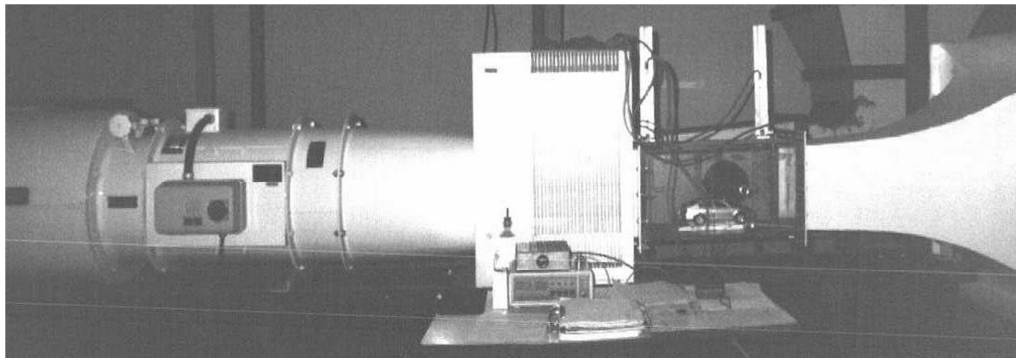


Figure 2.7 TE 54 Open circuit wind tunnel [4]

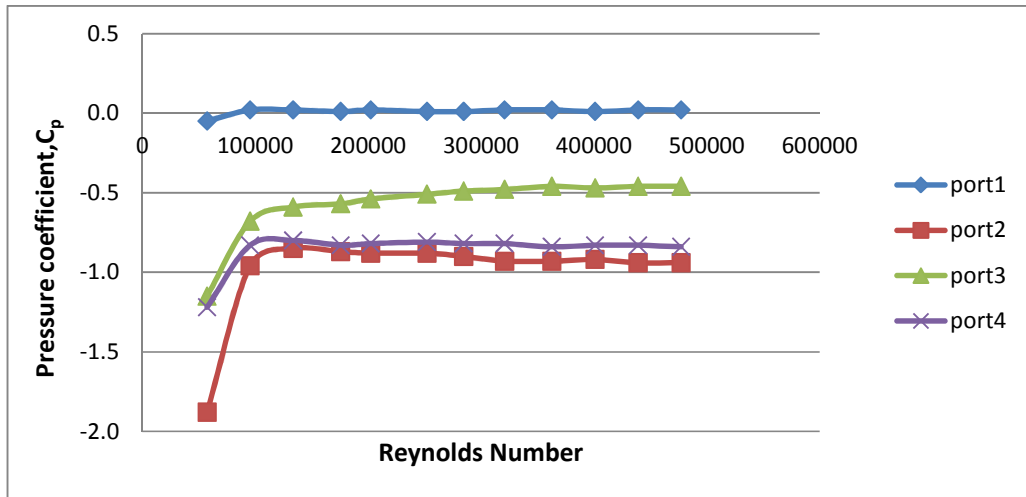


Figure 2.8 Variation of C_p with Reynolds Number (ports 1-4) [4]

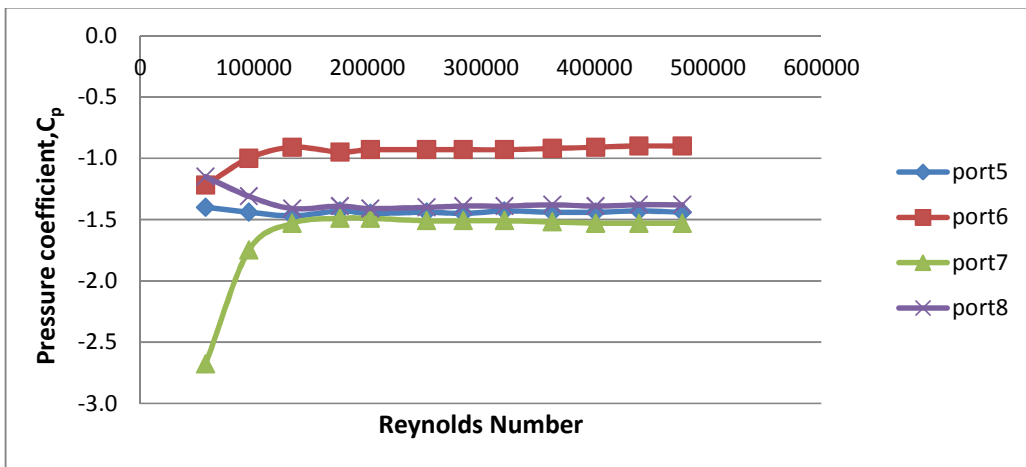


Figure 2.9 Variation of C_p with Reynolds Number (ports 5-8) [4]

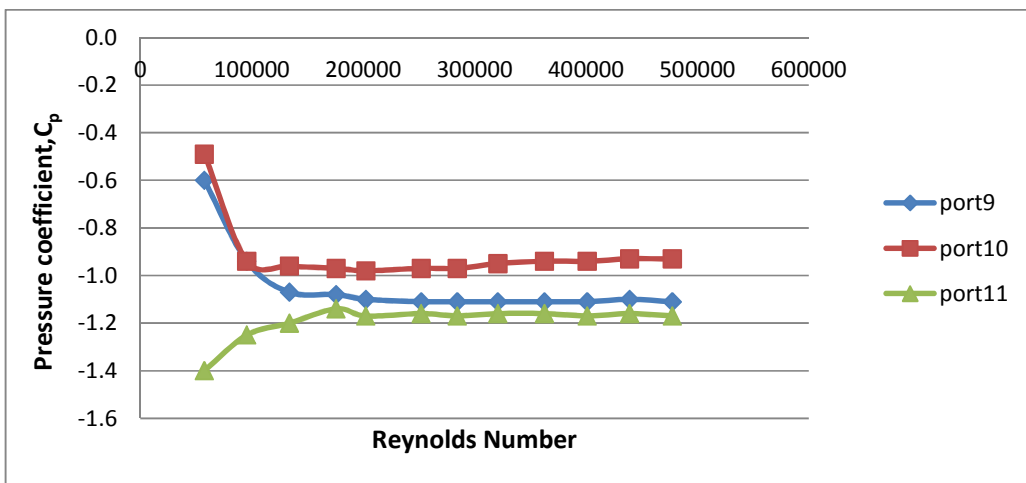


Figure 2.10 Variation of C_p with Reynolds Number (ports 9-11) [4]

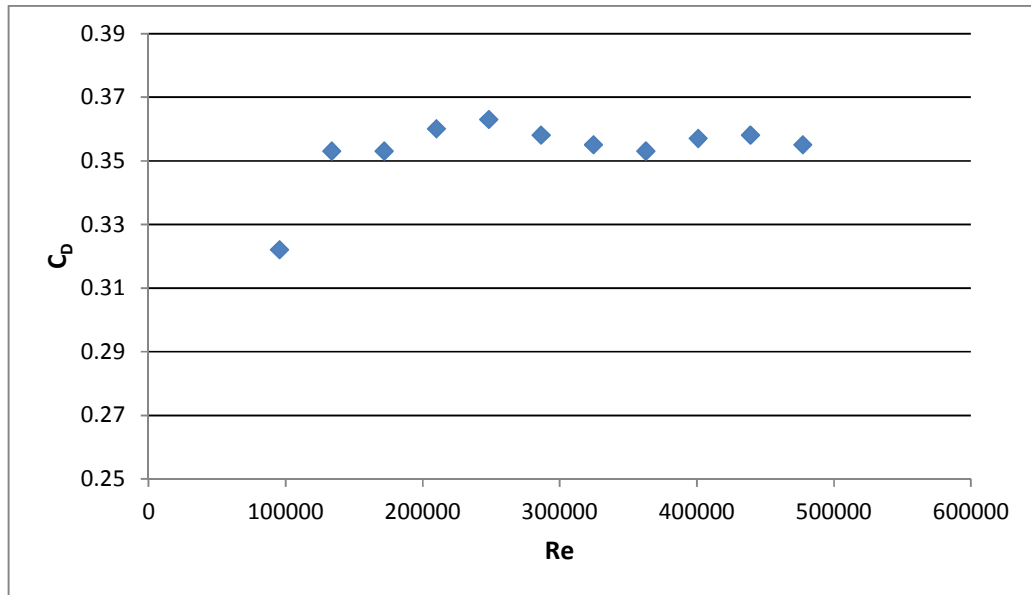


Figure 2.11 Variation of drag coefficient with Reynolds Number [4]

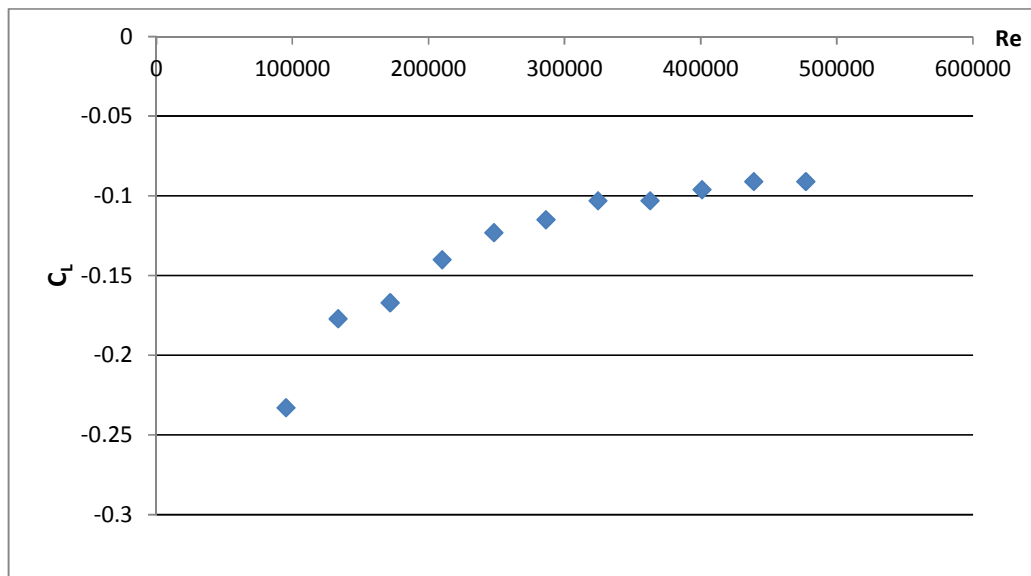


Figure 2.12 Variation of lift coefficient with Reynolds Number [4]

2.2 Assessment of Some Turbulence Models

In this section; according to the literature survey and Fluent [43], brief comments about some turbulence models available in Fluent software will be made and basic properties of them will be presented.

2.2.1 Spalart-Allmaras Model

Spalart-Allmaras model is a single equation turbulence model designed especially for aerospace applications. It also is getting popularity for turbomachinery applications. This model is very economical and suitable for 2-D, quasi 2-D external flows (e.g. airfoils, wings, missiles, ship hulls) but it performs poorly for some complex 3-D flows, flows with strong separation and free shear flows.

2.2.2 Standard $k-\varepsilon$ Model

Standard $k-\varepsilon$ model is the most widely used turbulence model for industrial applications despite of the known limitations. Model parameters are calibrated by using data from a number of benchmark experiments such as pipe flow, flat plate etc. It also has submodels for compressibility, buoyancy, combustion etc.

Most common issue in the literature about standard $k-\varepsilon$ model is performing poorly for flows with hard pressure gradient, strong separation and strong streamline curves.

2.2.3 RNG $k-\varepsilon$ Model

RNG $k-\varepsilon$ model is a version of standard $k-\varepsilon$ model. Constants in the k and ε equations are derived analytically using Renormalization Group Theory, instead of empirically from benchmark experimental data. Important changes in the ε equation improve the ability to model highly strained flows. Additional options aid in predicting swirling and low Reynolds number flows. RNG $k-\varepsilon$ model is proper for intricate flows involving rapid strain, moderate swirl, vortices, and locally transitional flows (e.g. boundary layer separation, vortex shedding, room ventilation).

2.2.4 Realizable k - ε Model

Realizable k - ε model is another version of the standard k - ε model. Its “realizability” originates from the changes which improve the performance of this model. It has similar applications as RNG and offers generally the same benefits. Possibly easier to converge and more accurate than RNG k - ε .

2.2.5 Standard k - ω Model

Standard k - ω model is a two-equation model solving for k and ω . It has several options for shear flow corrections, compressibility effects and transitional flows. It gives excellent performance for free shear, low Reynolds number and wall bounded boundary layer flows. It is also proper for intricate boundary layer flows under adverse pressure gradient and separation (turbomachinery and external aerodynamics). In some conditions separation may be predicted excessive and early.

2.2.6 SST k - ω Model

SST k - ω model is a version of the standard k - ω model. It blends the standard k - ω model for use near walls and the standard k - ε model away from walls using a combining function. It has no option for compressibility and offers generally the same advantages as standard k - ω .

2.2.7 Reynolds Stress Model

The Reynolds stress model (RSM) is a higher level, complicated turbulence model. In RSM, Reynolds stresses are solved directly using transport equations, abstaining isotropic viscosity assumption. It is physically the most elaborate RANS model. More CPU time and memory are required and it is hard to converge. Since it has no particular advantages in practical engineering applications, RSM is not used frequently. It is convenient for very complex 3-D flows with strong rotation/swirl, strong streamline curvatures (e.g. rotating flow passages, swirl combustors, curved ducts, cyclones).

CHAPTER 3

AERODYNAMICS OF ROAD VEHICLES

Aerodynamics mainly investigates the solid objects moving within an air media and the relation between the surfaces of these solid objects and the surrounding media.

The importance of aerodynamics in the automotive industry has been increasing. Requests such as need to reduce the fuel consumption, better driving performance, reduction of wind noise force car manufacturers to study vehicle aerodynamics.

3.1 Mechanics of Air Flow Around a Car

Flow over the body of a car can be explained by the relationship between velocity and pressure given in the simplified form of Bernoulli's Equation

$$P_{static} + P_{dynamic} = P_{total} \quad (3.1)$$

$$P_s + \frac{1}{2}\rho V^2 = P_t \quad (3.2)$$

where; ρ is the density of the fluid and V is the velocity of air (relative to the car)

In this equation it is assumed that flow is incompressible and is subjected to negligible friction. These assumptions are reasonable for automotive aerodynamics.

Considering the vehicle as stationary and the air is moving (as in wind tunnel), the air streams along lines, appropriately called "streamlines". A bunch of streamlines is called "streamtube". Injection of smoke in a wind tunnel makes it possible to see the streamtubes shown in Figure 3.1.



Figure 3.1 Streamtubes flowing over a car [26]

At a certain distance from the car the static pressure is the ambient pressure. On the other hand the dynamic pressure is produced by the relative velocity. As the flow approaches to the car, streamlines divide; some is going above the car and others below. But one streamline must stagnate on the car. The point at which velocity is zero is called stagnation point and the static pressure equals to the total pressure at that point since the dynamic pressure is zero [19].

The streamlines above the hood is firstly directed to upward and curvature is concave in that region. At some distance above the car where the streamlines are still straight, the static pressure is the same as the ambient. For the air stream to be curved upward, the static pressure in that region must be higher than ambient to supply the force necessary to turn the airflow [19]. Since the pressure is higher, velocity must decrease in that region as Bernoulli's Equation dictates.

On the other hand, as the flow turns to follow the hood, pressure must be smaller than ambient pressure and velocity must increase to provide the curvature downward.

The flow around a moving car behaves like the flow in a venturi channel. Flow over the front and back of the car is similar to the one in expanding region of the venturi whereas the flow over the top of the cabin is similar to the one in contracting region of the venturi. While pressure is high and the velocity is low at front and back of the car, pressure is low and velocity is high at the middle (Figure 3.2).

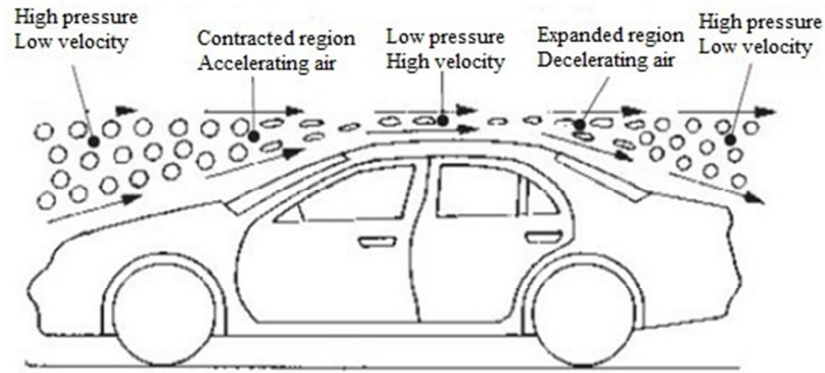


Figure 3.2 Pressure and velocity variation on the upper profile of a moving car [13]

If a relative movement exist between the air layers, an energy loss occurs due to friction since the air has a viscosity. If there is no separation, all the frictional effects can be considered to be confined in a thin region called boundary layer.

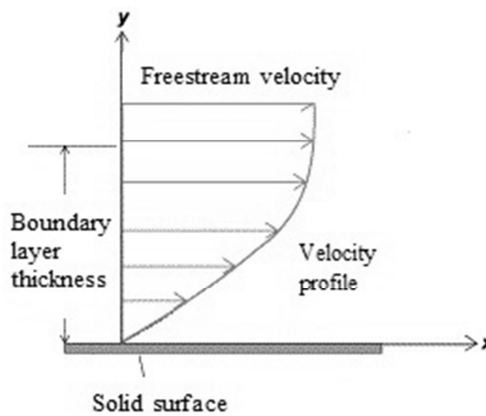


Figure 3.3 Boundary layer velocity profile

When air moves on a solid surface; in the region which is closest to solid surface, relative velocity is zero. As distance from the solid surface increases velocity also increases.

Flow over a flat plate surface of V_∞ velocity and P_∞ pressure is shown in Figure 3.4. With the assumption of no-slip, the flow at the beginning of the plate is steady and laminar.

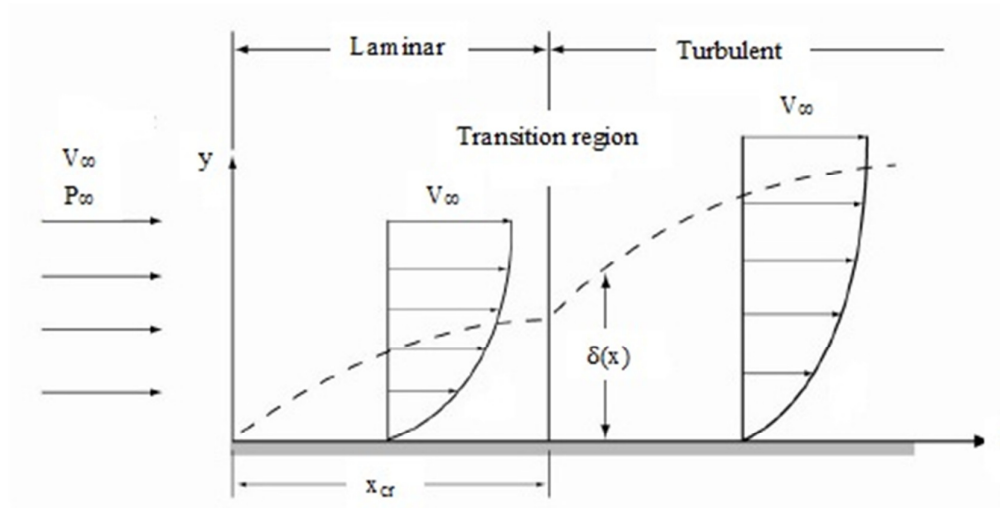


Figure 3.4 Boundary layer development on a flat plate [28]

After a certain distance x_{cr} from the leading edge, turbulent flow conditions occur. The governing parameter determining the regime of the flow is Reynolds number. Reynolds number is defined as the ratio between the inertia forces and viscous forces.

$$\text{Re} = \frac{\text{inertia forces}}{\text{viscous forces}} = \frac{\rho V L}{\mu} \quad (3.3)$$

where; ρ is the density of the fluid, V is the velocity of the fluid, μ is the dynamic viscosity of the fluid and L is the characteristic length of the plate.

For a flat plate surface, transition between turbulence and laminar flow occurs about Reynolds number of 5×10^5 . But this value is only valid for the situations in which pressure gradients are neglected. Flows in which pressure gradients exist, transition may happen at Reynolds number which is lower than the above value. Transition value is also affected by other conditions such as surface roughness.

Laminar and turbulent boundary layers have different characteristics. Since the separation point moves forward in turbulent boundary layer, drag force becomes less when it is compared to laminar boundary layer.

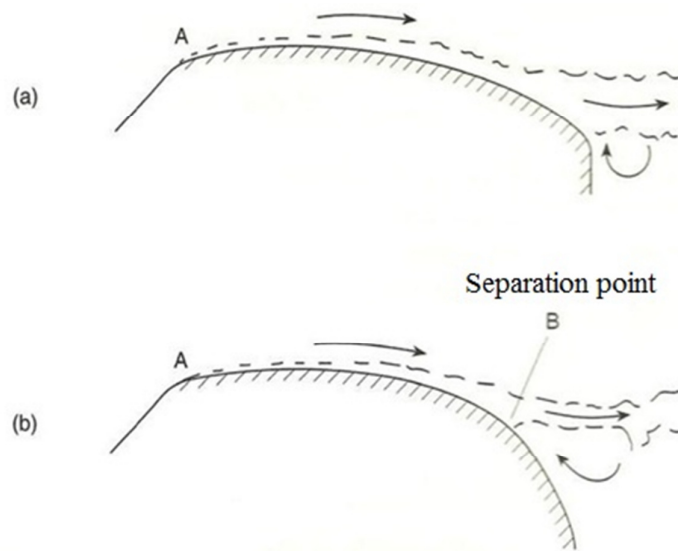


Figure 3.5 Adverse pressure gradients and flow separation [16]

Flows over a top of the two cars are shown in Figure 3.5. At point A velocity is quite high but pressure is low. From this point forward, pressure begins to increase with the decrease in velocity. This means that by continuously losing its velocity and energy, air flows from the low pressure region to high pressure region. Since the flow loses its energy to the friction, it never reaches its free stream velocity and pressure values. If pressure rise occurs progressively as Figure 3.5a; as a result of turbulence and molecular interactions, air molecules at outer layers pull the molecules at inner layers. But if pressure rise occurs potently (Figure 3.5b), boundary layer flow stops and separation occurs.

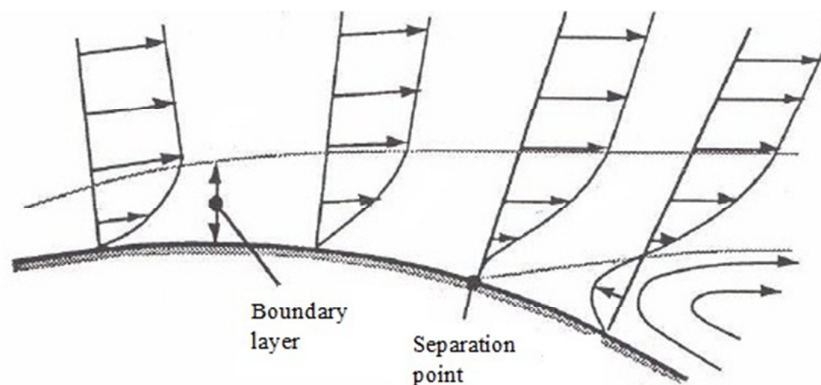


Figure 3.6 Separation under adverse pressure gradient [14]

In a boundary layer, if pressure decreases in the direction of the flow, this type of pressure gradient is called as favourable pressure gradient. Flow is impeded in the boundary layer and separation is not observed for that situation. But, if pressure increases in the direction of flow (adverse pressure gradient), the thickness of boundary layer grows and flow can be separated from the surface easily (Figure 3.6). Turbulent boundary layers are more resistant against separation when compared to the laminar boundary layers under the same adverse pressure gradient. This phenomenon is shown in Figure 3.7.

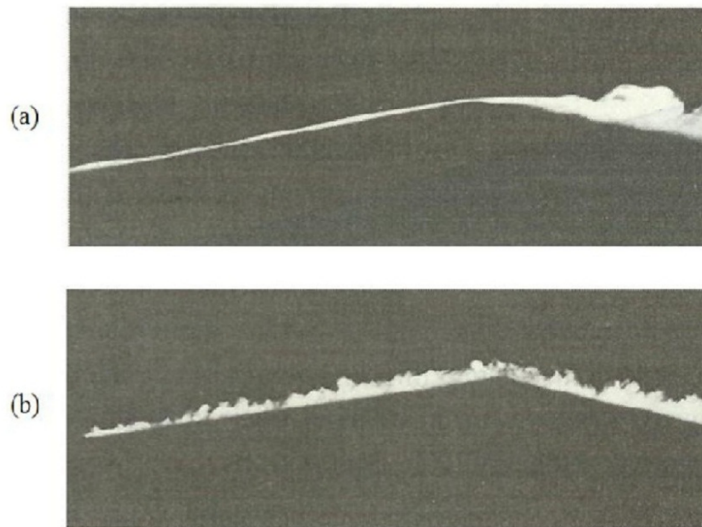


Figure 3.7 Comparison of laminar and turbulent boundary layers under adverse pressure gradient (a) Laminar (b) Turbulent [17]

The most important feature of the separation is the formation of turbulent region behind the car. Part of the momentum of a moving car has transferred to the surrounding air. This air creates a turbulent region with its momentum behind the car. Since the pressure of air at the behind of the car is smaller than the atmospheric pressure, air is tried to suck by the car and this creates a form drag which is in the opposite direction of the motion. Form drag composes the major part of the total aerodynamic drag. Therefore reduction in the form drag affects performance of the car significantly. Most of the studies have been focusing on reducing this force by retarding separation.

For some cases, separated flow may reattach to car surface. This situation is mostly observed in the region between the hood and the windshield (Figure 3.8). But in the back of the car, reattachment of the separated flow to the car surface is not probable. Separation bubbles are formed between separation and reattachment points as seen in Figure 3.8.

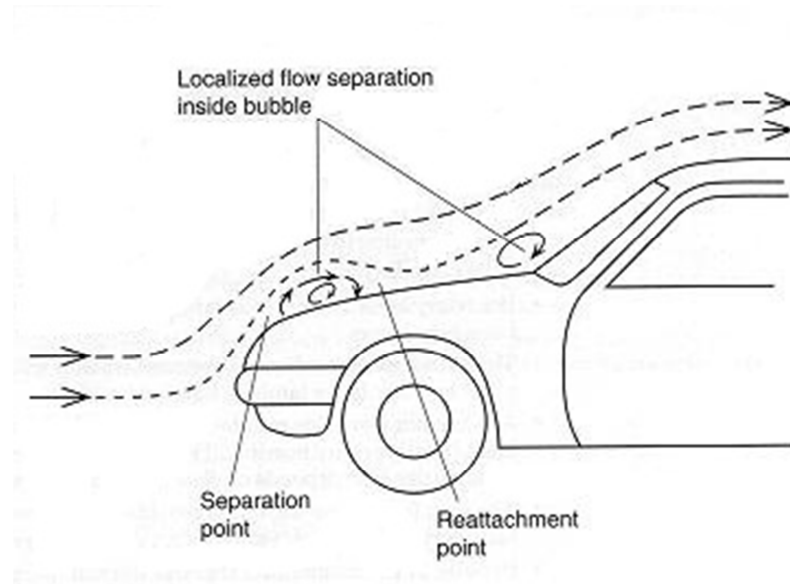


Figure 3.8 Local separations inside bubble [27]

3.2 Pressure Distribution on a Car

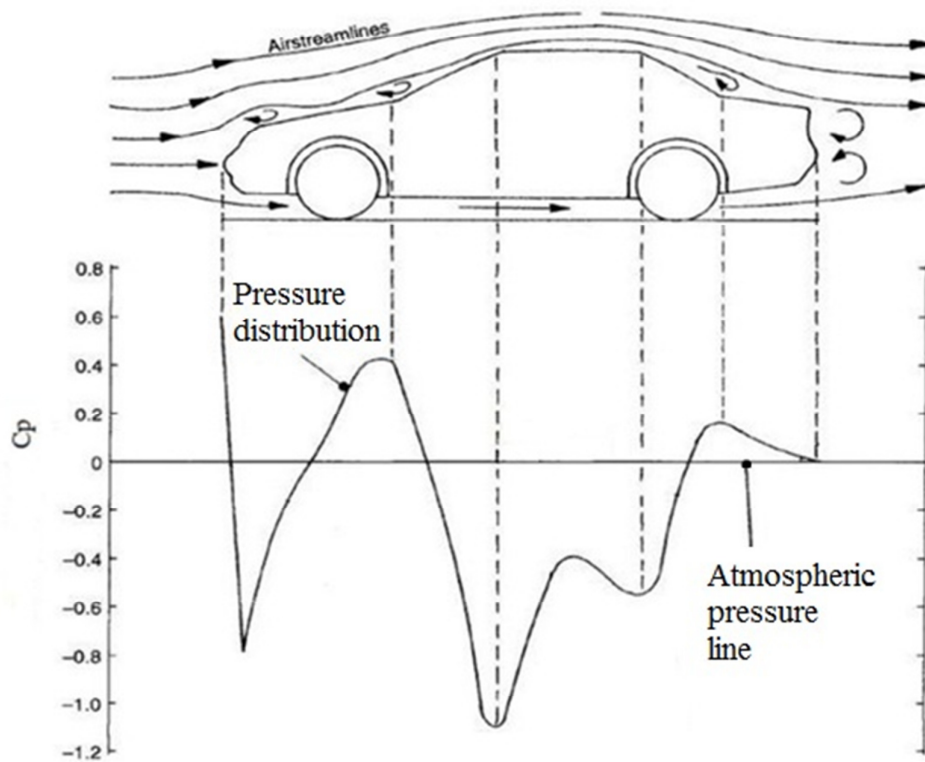


Figure 3.9 Pressure distribution along the centerline of a car [18]

Negative pressure is formed at the front edge of the hood as the flow rising over the front of the vehicle. The adverse pressure gradient in this region has the potential to stop the boundary layer flow. In recent years, studies have been increasing for detailing in front hood line to avoid separation in that region.

The flow must be turned upward near the base of the windshield and cowl where high pressure zone is formed. This high pressure zone is suitable place for inducting air for climate control systems and engine intake. The lower velocities in this region keep the windshield wipers from being disturbed.

Through the roof line the pressure again goes negative as the air flow endeavours to follow the roof contour. The pressure stays low down over the backlite and on the trunk because of the on-going curvature. This area is most probable region for flow separation. Due to the low pressure, the flow along the sides of a car will also try to

feed air into this region and may add to the potential for separation [19]. The general air flow patterns over the car are shown in Figure 3.10. The flow along the sides is participated into the low pressure region in the rear area, combining with the flow over the roof to form vortices trailing off to the back of the vehicle [19].

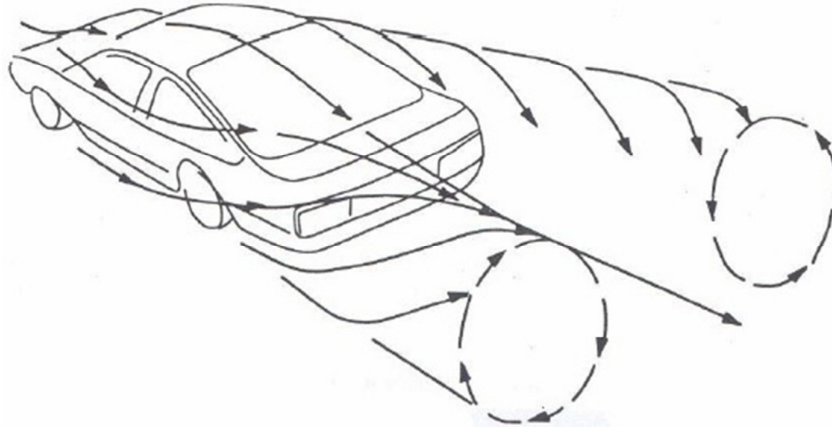


Figure 3.10 Vortex systems in the wake of a car [19]

Another factor in the aerodynamic design at the rear is the potential of dirt accumulation on the rear lights and backlite. The high level of turbulence in the separation area deposits dirt and moisture lifted from the road by the tires. If the separation area includes rear lights and backlite, dirt will be accumulated on these areas and vision will be precluded. Figure 3.11 illustrates this phenomenon.

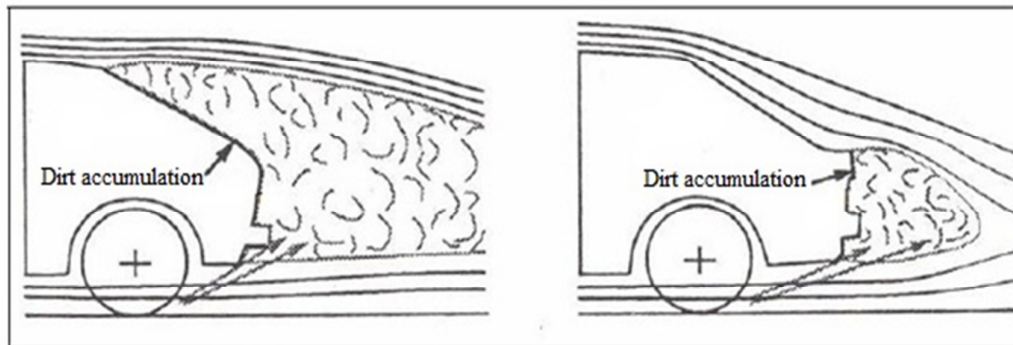


Figure 3.11 Effect of separation on dirt accumulation at the rear [19]

3.3 Aerodynamic Forces

Forces and moments are created as a result of air flow over the car body. These are illustrated in Figure 3.12 as three forces and three moments in principle axes of the car.

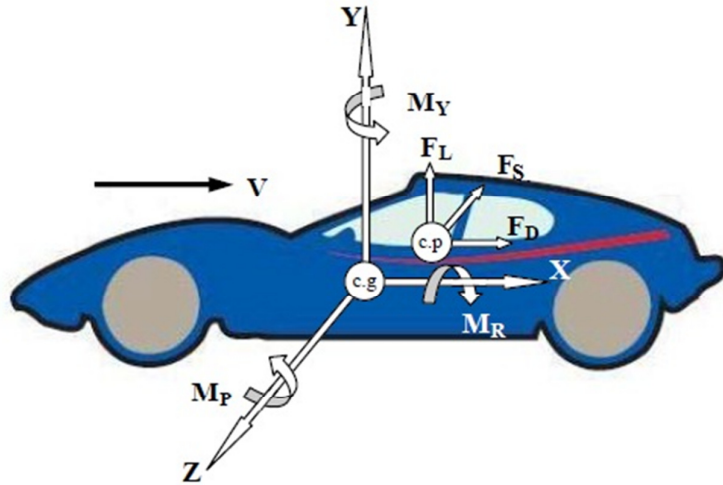


Figure 3.12 Aerodynamic forces and moments [20]

Table 3.1 Aerodynamic Forces and Moments

Direction	Force	Moment
Longitudinal (x -axis, positive rearward)	Drag	Rolling moment
Lateral (z -axis, positive to the right)	Side force	Pitching moment
Vertical (y -axis, positive upward)	Lift	Yawing moment

3.3.1 Drag Force and Drag Coefficient

Drag force is the most important aerodynamic factor for road vehicles and is very effective especially at speeds higher than 60 km/h. Therefore reduction in aerodynamic drag is very important in terms of fuel consumption and car performance.

$$F_D = C_D \frac{1}{2} \rho V^2 A \quad (3.4)$$

Drag force on any object depends on projection area of the object (A), velocity of the object (V), density of the fluid (ρ), and drag coefficient (C_D). Full aerodynamic characteristics of a car may not be explained solely by drag force. Because different drag forces act on cars which having different shapes and speeds. Thus it may not be appropriate to compare the drag force of two different cars. At this point, drag coefficient gives the opportunity to compare vehicles of different shape and velocity. Hence drag coefficient is the base criterion when investigating aerodynamic characteristics of vehicles.

Drag force acting on the car originates from surface friction, pressure, tires and wake vortices. These effects composing 90% of the total drag force of a car. To investigate all these effects one by one, makes it easier to understand the drag coefficient C_D

3.3.1.1 Effect of Friction on Drag

Surface friction drag depends on shear force and the position of the object (Figure 3.13).

$$(F_D)_f = \int_A \tau_w \sin \theta dA \quad (3.5)$$

in which; $(F_D)_f$ is surface friction drag force, τ_w is surface shear stress and dA is the differential area perpendicular to flow direction.

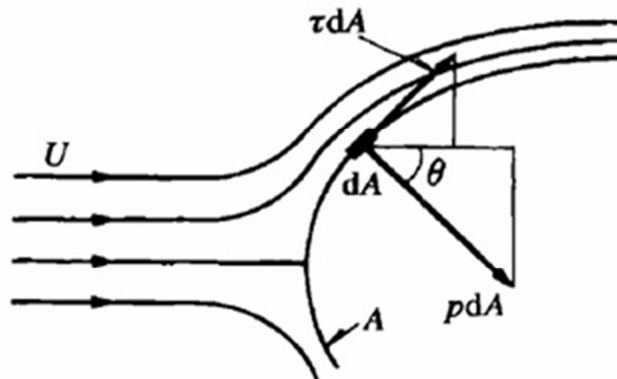
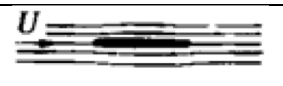
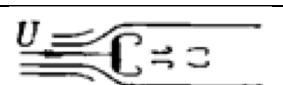


Figure 3.13 Drag components acting on an object [14]

Surface friction drag that perpendicular to flow is zero while it is maximum in parallel flow. Share of surface friction drag on total drag for some geometric shapes is given in Table 3.2

Table 3.2 Share of surface friction drag on total drag [14]

Shape	Share of surface friction drag on total drag (%)
	100
	≈90
	≈10
	0

Surface friction drag is directly related with viscosity of the fluid. When viscosity increases, shear force and surface friction drag also increases.

In laminar boundary layer, velocity gradient ($\partial V/\partial y$) close to the surface is smaller when it is compared to the one in turbulent boundary layer. For this reason shear stress and surface friction drag becomes much higher in turbulent boundary layer. It may seem to be beneficial to get laminar boundary layer in terms of surface friction drag but since the turbulent boundary layer retards the separation it further reduces the total drag force.

3.3.1.2 Effect of Pressure on Drag

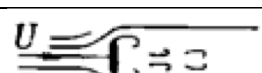
The major part of the total drag is arise from the pressure and known as pressure drag and also called as form drag as it mostly depends on the shape of the object.

$$(F_D)_p = \int_A (p - p_\infty) \cos \theta dA \quad (3.6)$$

in which; $(F_D)_p$ is the form drag force, p is the pressure, p_∞ is ambient pressure and dA is the differential area perpendicular to flow direction.

Share of form drag on total drag for some geometric shapes is presented in Table 3.3

Table 3.3 Share of form drag on total drag [14]

Shape	Share of form drag on total drag (%)
	0
	≈10
	≈90
	100

Form drag can be explained by the pressure distribution on the car. If friction did not exist, flow separation would not be observed. But in real situation adverse pressure gradient and flow separation occurs because of the viscosity.

The effect of viscosity over the flow on a smooth body is shown in Figure 3.14. If viscosity is neglected (Figure 3.14a), right on the nose, the relative air speed is brought to zero. The flow then accelerates, reaching a high relative speed and then slows down as it approaches the tail. The pressure distribution would be symmetrical and would therefore produce equal and opposite forces corresponding forward and rearward parts, there would be thus no drag. In reality (Figure 3.14b), viscosity causes the energy loss. As a consequence of the energy loss, the air cannot return to its initial speed and pressure. The pressure over the rear portion of the shape is lower than over the front, and there will therefore be a net rearward drag force. Almost all of the measures for reducing this drag force are focused on retarding the separation.

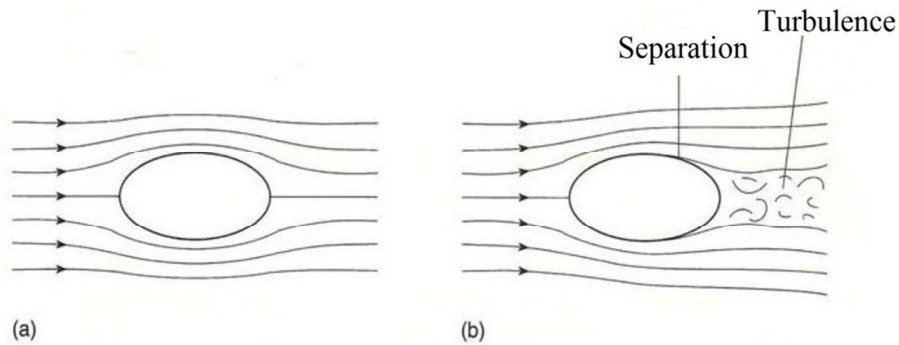


Figure 3.14 Effect of viscosity (a) Theoretical inviscid flow (b) Real viscous flow [16]

3.3.1.3 Effect of Wheels on Drag

Significant drag force is generated due to turbulent, recirculating flow around the wheels and wheel wells. Figure 3.15 illustrates the complex flow patterns in that region. The sharp edges of the wheel cutout provide opportunities to induce flow in the horizontal plane, while rotating wheel tend to induce circulation in the vertical plane. These effects allow the wheel to influence more flow than that of the flow subjected to its frontal area. It is possible to reduce the drag caused by the wheels by aerodynamic shielding of wheels and wheel wells. While this is applicable for rear wheels, it is not easy to implement such a treatment for front wheels due to limitations for steering. Experiments have shown that, reducing the distance between the ground surface and the bottom of the car and minimizing the wheel cavity decrease the aerodynamic drag caused by the wheels.

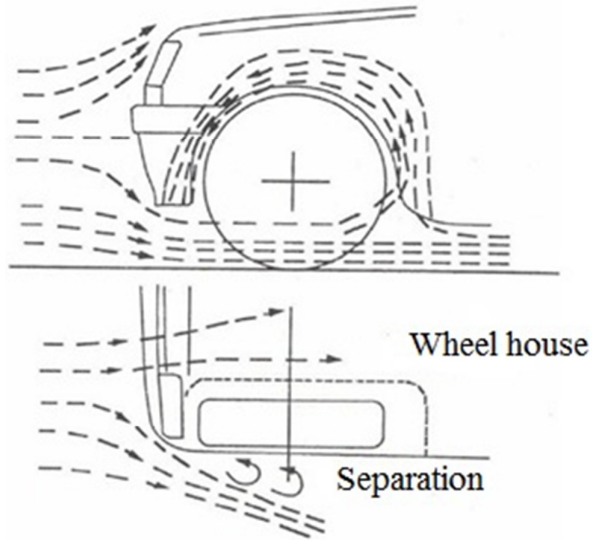


Figure 3.15 Air flow recirculation in a wheel well [19]

3.3.1.4 Effect of Engine Cooling System on Drag

The air needed for engine cooling system is provided by movement of the car and the fan of the radiator. Entrained air is subjected to a significant friction in the compartments of the engine. This complicated shape of the engine makes the flow become turbulent easily and separations are observed at many points. Hence drag force increases. Poorly designed cooling system may increase the total drag up to 10% [21].

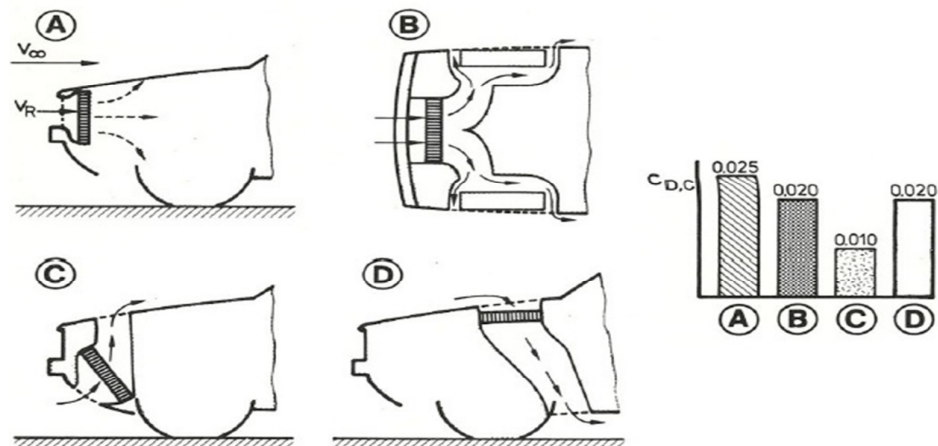


Figure 3.16 Alternative radiator arrangements for reducing the drag due to cooling system [21]

In Figure 3.16 various radiator arrangements are presented. The basic goal in these arrangements is to prevent the separation and occurrence of stagnation points by smoothing the entrance. Hence velocity does not decrease and static pressure is kept low.

3.3.1.5 Effect of Trailing Vortices on Drag

For most of the cars, lower pressures are observed on the roof of the car. An important result of that the air tends to flow from the high pressure underside towards the top surfaces, resulting in the production of vortices in the wake, as illustrated in Figure 3.17. These vortices are called as trailing vortices. A large amount of energy goes into the formation of these swirling masses of air, and it is clear therefore that they represent a source of drag. [16]

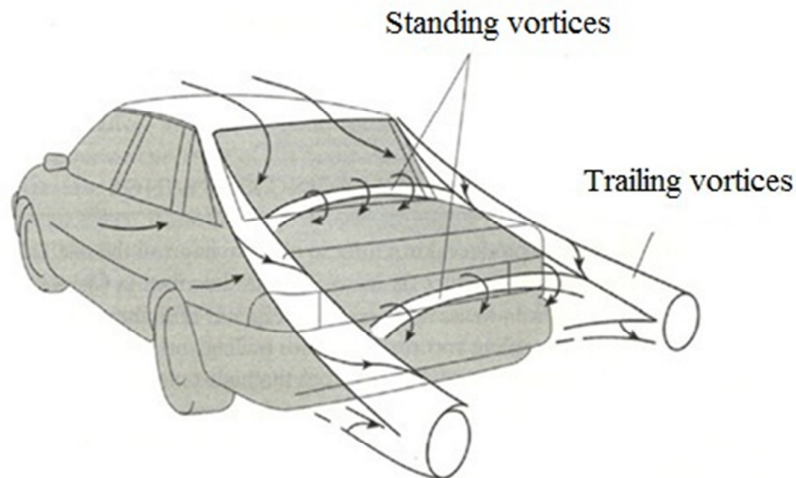


Figure 3.17 The three-dimensional nature of the flow around a car [16]

3.3.1.6 Effect of Drag on Fuel Consumption

It is important to obtain low drag coefficient in terms of fuel consumption because fossil fuel sources have been reducing day by day. Even the slightest decrease in aerodynamic drag can improve the fuel consumption in a positive way. In Figure 3.18 the variation of amount of fuel saving with drag reduction for different road conditions are presented. According to figure, 30% drag reduction causes 14%, 8% and 6% fuel save for level, main road and very difficult route respectively.

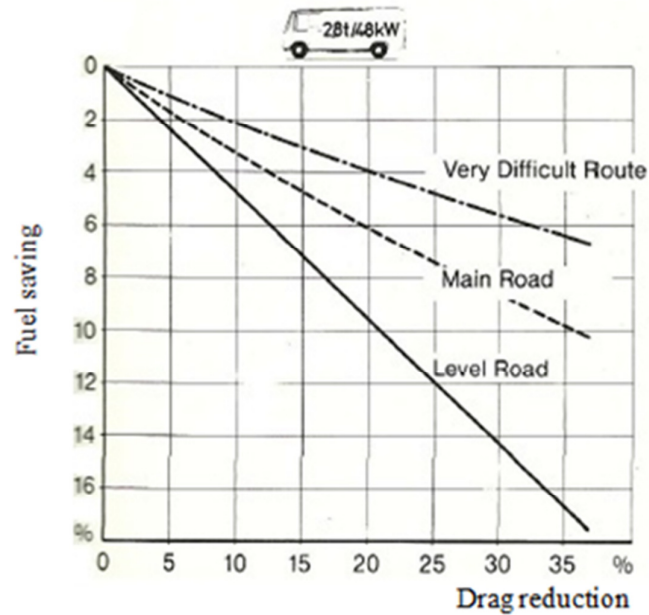


Figure 3.18 Influence of drag reduction on fuel saving [21]

3.3.1.7 Effect of Drag on Acceleration

Power transferred to wheels is smaller than the power produced in the engine during drive. The reasons for that is the power dissipated by the friction during transmission and the loss of power during acceleration. In a race car, power in the wheels can be as low as 40% of the power produced in the engine [16]. Effect of drag coefficient on the acceleration of the car can be seen in Figure 3.19.

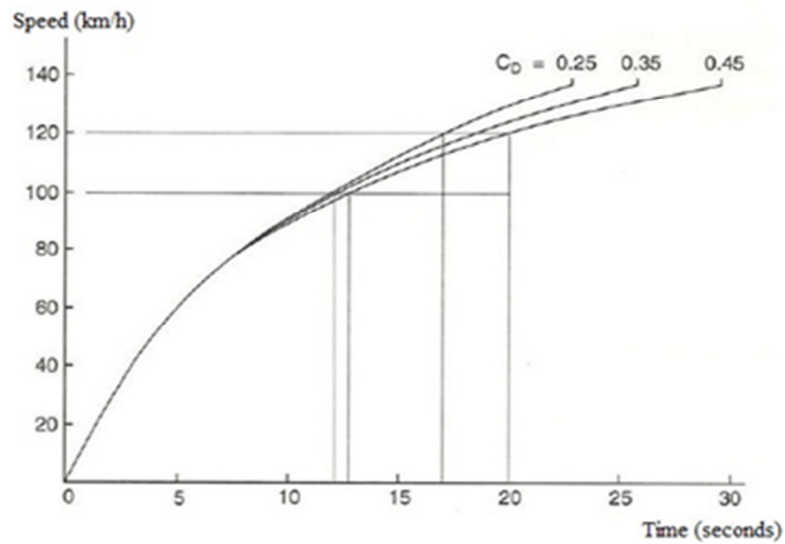


Figure 3.19 Effect of drag coefficient on acceleration [16]

3.3.1.8 Effect of Drag on Maximum Speed

Power transferred to the wheels depends on engine power and transmission losses. For a car to reach a desired speed, a force to overcome the resisting forces should be generated. In Figure 3.20, the relationship between the wheel power and maximum speed for different drag coefficient values is shown. When C_D decreases from 0.45 to 0.25 maximum speed increases to 191 km/h from 160 km/h for 52 kW wheel power.

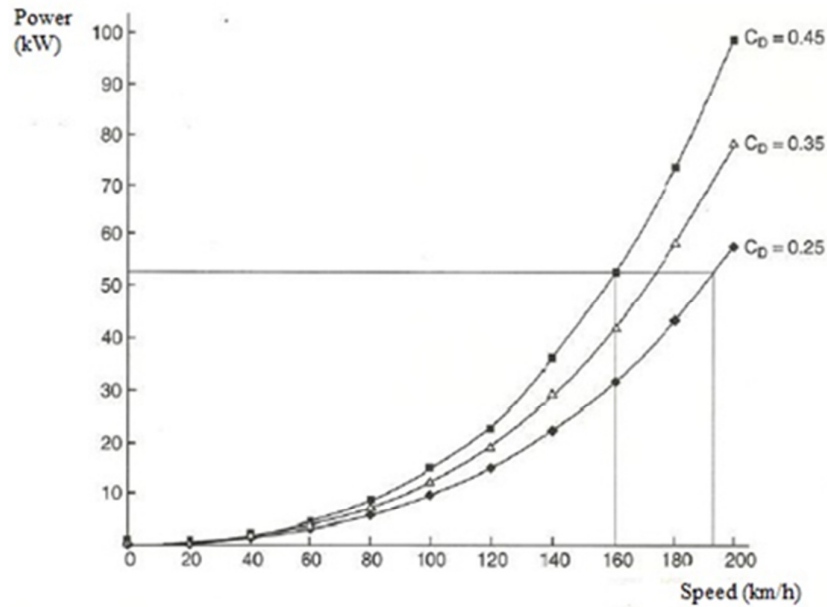


Figure 3.20 Total power against speed for various C_D values [16]

3.3.2 Lift Force and Lift Coefficient

The difference in pressure between top and bottom of the car causes a lift force. Since this lift force acting differently on front and rear shafts, it produces a pitching moment. For speed above 100 km/h, lift force is very important and have a major impact on driving stability.

Lift force coefficient (C_L) is calculated as,

$$C_L = \frac{F_L}{\frac{1}{2} \rho V^2 A} \quad (3.7)$$

in which; F_L is the lift force, ρ is the density of air, V is velocity and A is area.

3.3.3 Side Force and Side Force Coefficient

In real conditions, the directions of the vehicle and the wind do not match all the time. This produces a side force besides lift and drag forces. Side force coefficient (C_s) is found as;

$$C_s = \frac{F_s}{\frac{1}{2}\rho V^2 A} \quad (3.8)$$

in which; F_s is side force, ρ is the density of air, V is velocity and A is area.

Side force affects the stability of the car. Beside the effect of twisting the vehicle around on its axis, side force produces a yawing moment. Side forces are important especially while driving at curves.

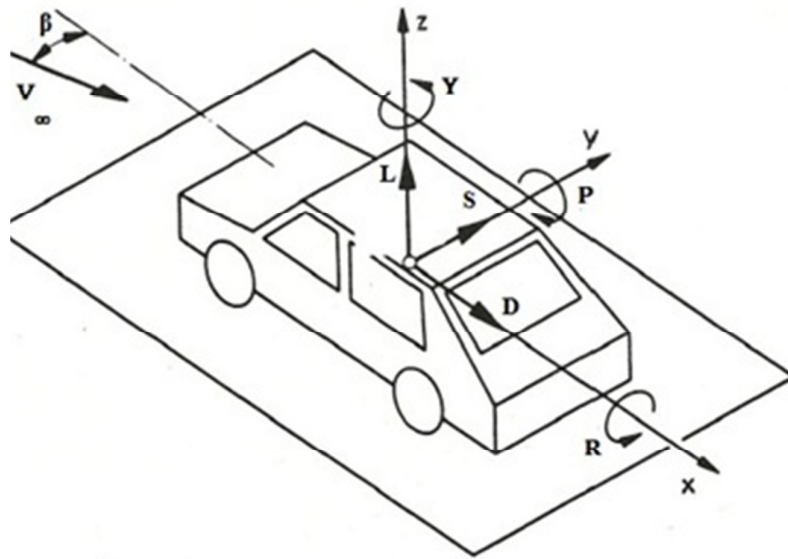


Figure 3.21 Aerodynamic forces and moments acting on a car and the definition of yaw angle (β) [21]

Drag coefficients is determined for $\beta=0$. But it is impossible to ignore the effect of side force on drag coefficient in real road conditions. When β increases, drag force also increases [21].

CHAPTER 4

MATHEMATICAL FORMULATION

4.1 General Equations

4.1.1 Continuity Equation

Continuity equation is expressed by the mass balance of a fluid element. This mass balance can be stated as, rate of increase of mass in fluid element equals to net rate of flow of mass into fluid element.

$$\frac{\partial \rho}{\partial t} + \frac{\partial(\rho u)}{\partial x} + \frac{\partial(\rho v)}{\partial y} + \frac{\partial(\rho w)}{\partial z} = 0 \quad (4.1)$$

If velocity vector expressed as $\vec{u} = u\vec{i} + v\vec{j} + w\vec{k}$, Equation (4.1) becomes

$$\frac{\partial \rho}{\partial t} + \text{div}(\rho \vec{u}) = 0 \quad (4.2)$$

The first term on the left hand side is the rate of change in time of the density. The second term indicates the net flow of mass out of the element across its boundaries and is called convective term [25].

For an incompressible fluid, the density ρ is constant and Equation (4.2) becomes

$$\text{div} \vec{u} = 0 \quad (4.3)$$

or

$$\frac{\partial u}{\partial x} + \frac{\partial v}{\partial y} + \frac{\partial w}{\partial z} = 0 \quad (4.4)$$

4.1.2 Momentum Equation

Newton's second law asserts that the rate of change of momentum of a fluid particle equals to the sum of the forces on the particle. The rates of increase of x , y and z momentum per unit volume of a fluid particle are given by $\rho \frac{Du}{Dt}$, $\rho \frac{Dv}{Dt}$ and $\rho \frac{Dw}{Dt}$ respectively.

Hence, the x , y and z components of the momentum equation are expressed as

$$\rho \frac{Du}{Dt} = \frac{\partial(-p + \tau_{xx})}{\partial x} + \frac{\partial \tau_{yx}}{\partial y} + \frac{\partial \tau_{zx}}{\partial z} + S_{Mx} \quad (4.5a)$$

$$\rho \frac{Dv}{Dt} = \frac{\partial \tau_{xy}}{\partial x} + \frac{\partial(-p + \tau_{yy})}{\partial y} + \frac{\partial \tau_{zy}}{\partial z} + S_{My} \quad (4.5b)$$

$$\rho \frac{Dw}{Dt} = \frac{\partial \tau_{xz}}{\partial x} + \frac{\partial \tau_{yz}}{\partial y} + \frac{\partial(-p + \tau_{zz})}{\partial z} + S_{Mz} \quad (4.5c)$$

respectively. Where,

$\frac{D}{Dt} = \frac{\partial}{\partial t} + u \frac{\partial}{\partial x} + v \frac{\partial}{\partial y} + w \frac{\partial}{\partial z}$ is the total derivative, and p is the pressure, τ is viscous

stresses, S is the source term, τ_{ij} indicates the direction of the viscous stresses. The suffices i and j in τ_{ij} indicate that the stress component acts in the j -direction on a surface normal to the i -direction.

4.1.3 Navier-Stokes Equations

In many fluid flows the viscous stresses can be expressed as functions of the local deformation rate. In 3-D flows the local rate of deformation is composed of the linear deformation rate and volumetric deformation rate. By the assumption of fluids are isotropic, the rate of linear deformation of a fluid element has nine components in three dimensions [25]. There are three linear elongating deformation components,

$$e_{xx} = \frac{\partial u}{\partial x}, \quad e_{yy} = \frac{\partial v}{\partial y}, \quad e_{zz} = \frac{\partial w}{\partial z} \quad (4.6a)$$

and there are also six shearing linear deformation components,

$$e_{xy} = e_{yx} = \frac{1}{2} \left(\frac{\partial u}{\partial y} + \frac{\partial v}{\partial x} \right) \quad (4.6b)$$

$$e_{xz} = e_{zx} = \frac{1}{2} \left(\frac{\partial u}{\partial z} + \frac{\partial w}{\partial x} \right) \quad (4.6c)$$

$$e_{yz} = e_{zy} = \frac{1}{2} \left(\frac{\partial v}{\partial z} + \frac{\partial w}{\partial y} \right) \quad (4.6d)$$

The volumetric deformation is given by

$$\frac{\partial u}{\partial x} + \frac{\partial v}{\partial y} + \frac{\partial w}{\partial z} = \text{div} \bar{u} \quad (4.7)$$

In a Newtonian fluid the viscous stresses are proportional to the rates of deformation [25]. The 3-D form of Newton's law of viscosity for compressible flows, involves two constants of proportionality: the dynamic viscosity μ , and the second viscosity λ . μ relates stresses to linear deformations and λ , relates stresses to the volumetric deformation. The nine viscous stress components are,

$$\tau_{xx} = 2\mu \frac{\partial u}{\partial x} + \lambda \text{div} \bar{u} \quad (4.8a)$$

$$\tau_{yy} = 2\mu \frac{\partial v}{\partial y} + \lambda \text{div} \bar{u} \quad (4.8b)$$

$$\tau_{zz} = 2\mu \frac{\partial w}{\partial z} + \lambda \text{div} \bar{u} \quad (4.8c)$$

$$\tau_{xy} = \tau_{yx} = \mu \left(\frac{\partial u}{\partial y} + \frac{\partial v}{\partial x} \right) \quad (4.8d)$$

$$\tau_{xz} = \tau_{zx} = \mu \left(\frac{\partial u}{\partial z} + \frac{\partial w}{\partial x} \right) \quad (4.8e)$$

$$\tau_{yz} = \tau_{zy} = \mu \left(\frac{\partial v}{\partial z} + \frac{\partial w}{\partial y} \right) \quad (4.8f)$$

For gases $\lambda = -\frac{2}{3}\mu$ suggested in the literature [47]. Liquids are incompressible so that $div\bar{u} = 0$. Therefore viscous stresses are just twice the local rate of linear deformation times the dynamic viscosity.

Using Equations (4.8a), (4.8d) and (4.8e) with Equation (4.5a) gives,

$$\begin{aligned} \rho \frac{Du}{Dt} &= \frac{\partial}{\partial x} \left[-p + 2\mu \frac{\partial u}{\partial x} + \lambda \left(\frac{\partial u}{\partial x} + \frac{\partial v}{\partial y} + \frac{\partial w}{\partial z} \right) \right] + \frac{\partial}{\partial y} \left[\mu \left(\frac{\partial u}{\partial y} + \frac{\partial v}{\partial x} \right) \right] \\ &+ \frac{\partial}{\partial z} \left[\mu \left(\frac{\partial u}{\partial z} + \frac{\partial w}{\partial x} \right) \right] + S_{M_x} \end{aligned} \quad (4.9)$$

$$\begin{aligned} \rho \frac{Du}{Dt} &= -\frac{\partial p}{\partial x} + \frac{\partial}{\partial x} \left[2\mu \frac{\partial u}{\partial x} + \lambda div\bar{u} \right] + \frac{\partial}{\partial y} \left[\mu \left(\frac{\partial u}{\partial y} + \frac{\partial v}{\partial x} \right) \right] \\ &+ \frac{\partial}{\partial z} \left[\mu \left(\frac{\partial u}{\partial z} + \frac{\partial w}{\partial x} \right) \right] + S_{M_x} \end{aligned} \quad (4.10)$$

The viscous terms can be rearranged as follows:

$$\begin{aligned} &\frac{\partial}{\partial x} \left[2\mu \frac{\partial u}{\partial x} + \lambda div\bar{u} \right] + \frac{\partial}{\partial y} \left[\mu \left(\frac{\partial u}{\partial y} + \frac{\partial v}{\partial x} \right) \right] + \frac{\partial}{\partial z} \left[\mu \left(\frac{\partial u}{\partial z} + \frac{\partial w}{\partial x} \right) \right] \\ &= \frac{\partial}{\partial x} \left(\mu \frac{\partial u}{\partial x} \right) + \frac{\partial}{\partial y} \left(\mu \frac{\partial u}{\partial y} \right) + \frac{\partial}{\partial z} \left(\mu \frac{\partial u}{\partial z} \right) + \left[\frac{\partial}{\partial x} \left(\mu \frac{\partial u}{\partial x} \right) + \frac{\partial}{\partial y} \left(\mu \frac{\partial v}{\partial x} \right) + \frac{\partial}{\partial z} \left(\mu \frac{\partial w}{\partial x} \right) \right] \\ &+ \frac{\partial}{\partial x} (\lambda div\bar{u}) = div(\mu gradu) + s_{M_x} \end{aligned} \quad (4.11)$$

Defining a new source term as

$$S_M = S_M + s_M \quad (4.12)$$

and the Navier-Stokes equations can be written in the well-known form

$$\rho \frac{Du}{Dt} = -\frac{\partial p}{\partial x} + div(\mu gradu) + S_{M_x} \quad (4.13)$$

In a similar way, using Equations (4.8b), (4.8d) and (4.8f) with Equation (4.5b) and using Equations (4.8c), (4.8e) and (4.8f) with Equation (4.5c) gives y and z components of Navier-Stokes equations as,

$$\rho \frac{Dv}{Dt} = -\frac{\partial p}{\partial y} + \text{div}(\mu \text{grad}v) + S_{My} \quad (4.14)$$

$$\rho \frac{Dw}{Dt} = -\frac{\partial p}{\partial z} + \text{div}(\mu \text{grad}w) + S_{Mz} \quad (4.15)$$

4.2 Finite Volume Method and Discretization Methods

Generally there are three kinds of discretization methods: Finite difference method, finite element method and finite volume method. Fluent software uses the finite volume method to convert the transport equations to algebraic equations. The finite volume method is based on the integral form of the conservation equation [24]:

$$\frac{\partial}{\partial t} \int_V \rho \phi dV + \int_S \rho \phi V \cdot n dS = \int_S \Gamma \nabla \phi \cdot n dS + \int_V q_\phi dV \quad (4.16)$$

where Γ is the diffusion coefficient of ϕ . The computational domain is decomposed into many control volumes with the computational mesh. Thus, the convective and diffusive terms in Equation (4.16) show the integration of flux through the control volume surfaces (S) (4 in 2-D, 6 in 3-D). Figure 4.1 shows a 2-D grid and “typical” control volume. Fluent uses a co-located scheme that stores velocity and pressure at the cell center. By using the simplest approximation (midpoint rule), the flux through the west side of the cell can be expressed as:

$$F_w = \int_{S_w} f dS = \bar{f} S_w \approx f_w S_w \quad (4.17)$$

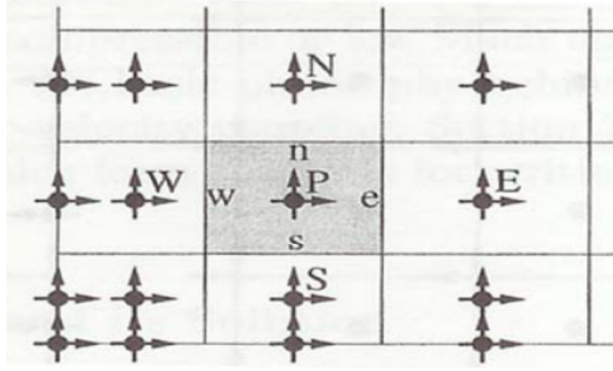


Figure 4.1 2-D control volume in cartesian coordinates [23]

$f = \rho\phi V \cdot n$ in the convective term and $f = \Gamma \nabla \phi \cdot n$ in the diffusive term. Equation (4.17) gives the total flux through the west side of the cell. This method is under the assumption that the averaged flux at west side of the cell is equal to the flux at the middle point of the west side. The next question is; how to calculate f_w ? Since all the variables are stored at cell center P , for getting the value at the surface center, some interpretations are needed. The standard approach is called the upwind scheme. There are four different upwind schemes in Fluent software; first order, second order, power law and QUICK [24]. In order to have consistent order of accuracy the second order upwind scheme is picked up for CFD simulations in this study. In second order approach, the face center value ϕ_f can be expressed as;

$$\phi_f = \phi + \Delta\phi \cdot \vec{r} \quad (4.18)$$

where ϕ is the cell-centered value. $\Delta\phi$ is the gradient at the cell center. \vec{r} is the displacement vector from the upstream cell center to the face center. One remaining issue here is; how to calculate $\Delta\phi$? There are many ways to calculate the gradient vector at the cell center. In Fluent software by applying Gauss Theorem, $\Delta\phi$ can be calculated at the cell center by the following approximation [24];

$$\Delta\phi = \frac{\sum_f \phi_f \vec{S}_f}{V} \quad (4.19)$$

\vec{S}_f is the surface vector at all faces of the control volume and V is the cell volume. ϕ_f is the value at the face center which can be calculated by two different methods in Fluent software. The default method is Green-Gauss Cell-Based evaluation, which

takes the arithmetic average of the values at the neighbouring cell centers. The other method is the Green-Gauss Node-Based evaluation method, which takes the average of the nodal values on the face [24].

$$\phi_f = \frac{\sum_{n=1}^{N_f} \phi_n}{N_f} \quad (4.20)$$

N_f is the number of nodes on the face. The nodal value, ϕ_n , is the weighted average of the cell values surrounding it. The node-based method is more accurate than the cell-based method for unstructured meshes [24]. For this reason the node-based method is picked for CFD simulations in this study.

4.2.1 Numerical Solution of the Navier-Stokes Equations

The unknowns in the continuity and momentum equations are velocity and pressure. Density is constant for incompressible flows and pressure is a function of density. However, there is no independent equation for pressure. Pressure gradients are distributed in the momentum equation. The continuity equation, which does not have a pressure term, is dependent on the velocities contained within the momentum equation. While the momentum equation determines the velocity field, there should be a method to solve pressure and also let the velocities to satisfy the continuity equation. One common way is to combine the continuity and momentum equations. Then the Poisson (pressure correction) equation can be obtained. For cartesian coordinates, it can be expressed as;

$$\frac{\partial}{\partial x_i} \left(\frac{\partial P}{\partial x_i} \right) = - \frac{\partial}{\partial x_i} \left[\frac{\partial}{\partial x_j} (\rho u_i u_j - \tau_{ij}) \right] + \frac{\partial (\rho g_i)}{\partial x_i} + \frac{\partial^2 \rho}{\partial t^2} \quad (4.21)$$

where g is the body force. With constant viscosity and density, Equation (4.21) becomes;

$$\frac{\partial}{\partial x_i} \left(\frac{\partial P}{\partial x_i} \right) = - \frac{\partial}{\partial x_i} \left[\frac{\partial}{\partial x_j} (\rho u_i u_j) \right] \quad (4.22)$$

With the momentum equation and pressure correction equation, a pressure field to solve these equations iteratively needed to assume. This method is called pressure-correction or projection method.

Depending on the flow speed, Fluent software has two types of solver; pressure-based and density-based. In this study pressure-based solver is used because of incompressible flow conditions. The pressure-based solver also has two kinds of algorithms; segregated and coupled. The segregated algorithm solves velocity and pressure separately. The velocity field is first solved using the updated values and the pressure correction equation is solved with the obtained velocity field and mass flux. After updating the velocity field, pressure, mass flux and all other scalars, if any, are solved. There are three options for the pressure-based segregated algorithm; SIMPLE, SIMPLEC and PISO. The other method is called coupled algorithm, which solves momentum and continuity equations at the same time. The difference between the segregated and coupled algorithms is clear; although the coupled algorithm is faster, it will consume more memory than the segregated algorithm. Hence the SIMPLE method is selected for this study. This method uses the pressure-correction (projection) method to solve pressure and velocity iteratively until the solution converges. A pressure field is assumed initially to start. For example, the x -momentum equation ($\phi = u$) can be discretized to;

$$a_p u = \sum_{nb} a_{nb} u_{nb} + \sum p \bar{A} + S \quad (4.23)$$

where nb means the neighbouring points and S is the source term which contains all other forces such as gravity. The guessed and corrected relation of pressure and velocity can be expressed as;

$$p = p^* + p' \quad \text{and} \quad u = u^* + u' \quad (4.24)$$

where p^* , u^* are the guessed values, p' , u' are the correction values, and p , u are the correct values. The idea is to have a guessed pressure field p^* and put it into Equation (4.23), hence,

$$a_p u^* = \sum_{nb} a_{nb} u_{nb}^* + \sum p^* \bar{A} + S \quad (4.25)$$

Subtracting Equation (4.25) from Equation (4.23),

$$a_p (u - u^*) = \sum_{nb} a_{nb} (u_{nb} - u_{nb}^*) + \sum (p - p^*) \bar{A} + S \quad (4.26)$$

For the SIMPLE algorithm, it is assumed that the first term on RHS of Equation (4.26) is zero. That means the velocity values at all neighbouring points are guessed

values. Then the corrected velocity u is used in the continuity equation. The continuity equation is marched with the pressure term. To ensure that pressure and velocity satisfy the continuity equation, the source term should be zero for convergence ($S=0$) [24]. Figure 4.2 describes the projection method schematically.

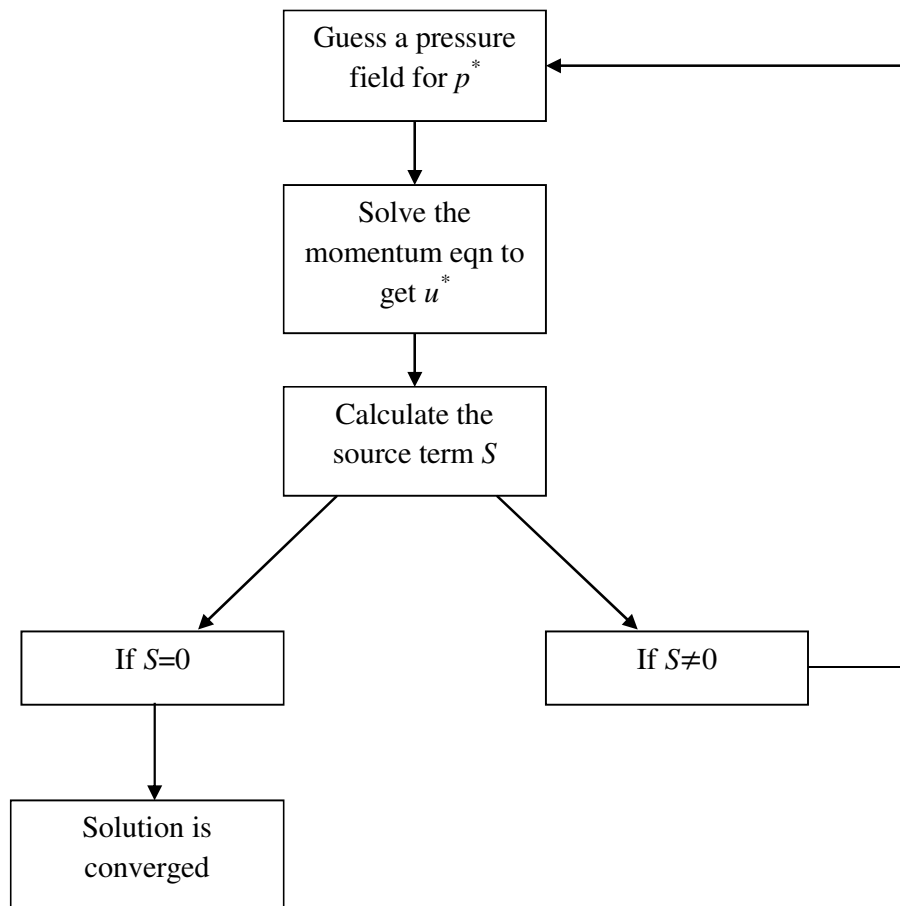


Figure 4.2 Diagram of projection method

CHAPTER 5

TURBULENCE AND ITS MODELING

Today many phenomena in nature could be explained by scientific methods. But some natural phenomena such as turbulence are still not defined and explained completely. Nobel winner physicist Richard Feynman explained turbulence as "the most important unsolved problem of classical physics" [29].

Efforts of understood of turbulence started 500 years ago. Leonardo da Vinci, famous painter, architect, mathematician and engineer of his age, described turbulence as,

“Observe the motion of the surface of the water, which resembles that of hair, which has two motions, of which one is caused by the weight of the hair, the other by the direction of the curls; thus the water has eddying motions, one part of which is due to the principal current, the other to random and reverse motion.” [30]

Another description of Da Vinci gives a significant description with a sketch of turbulent flow which his own painting as follows,

“...the smallest eddies are almost numberless, and large things are rotated only by large eddies and not by small ones, and small things are turned by small eddies and large.” [30]

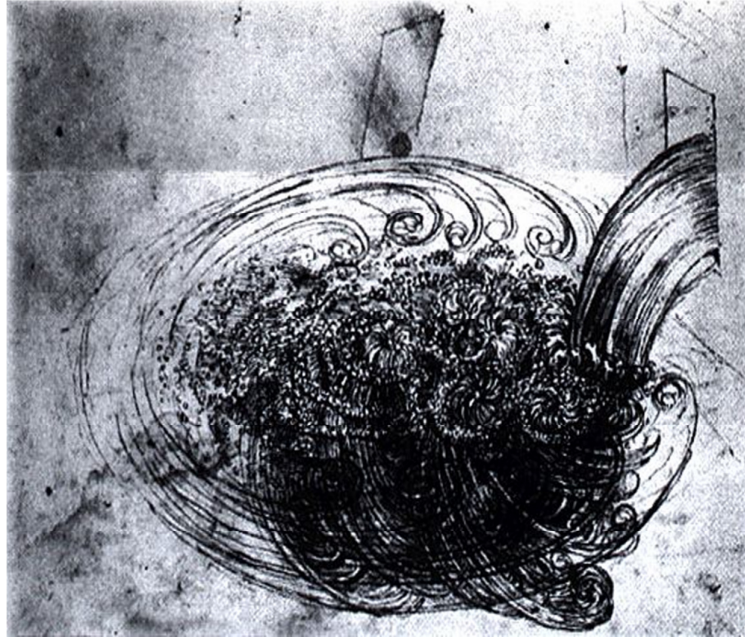


Figure 5.1 Leonardo da Vinci's sketch of turbulence [30]

According to Taylor and Von Karman, turbulence is defined in 1935 as:

“... an irregular motion which in general makes its appearance in fluids, gaseous or liquid, when they flow past solid surfaces or even when neighbouring streams of the same fluid flow past or over one another.” [31]

In 1959, Hinze redefined turbulence based on Taylor and Von Karman in a more precise manner as:

“Turbulent fluid motion is an irregular condition of flow in which the various quantities show a random variation with time and space coordinates, so that statistically distinct average values can be discerned.” [33]

In addition, Cebeci and Smith in 1974 extended the definition of turbulence as:

“... turbulence has a wide range of scales.” [33]

In general, it can be said that turbulent flow is a flow regime characterized by chaotic and stochastic property changes.

All flows experienced in engineering, become unstable above a specific Reynolds number. At low Reynolds numbers, flows are laminar. So the flow is smooth and

contiguous layers of fluid glide past each other in a tidy way. On the other hand; at high Reynolds numbers, flows are noticed to become turbulent. Complex and rapid events come off which ultimately leads to a complete change of the flow form. In the final state the flow manner becomes chaotic and random.

There are countless experiences of turbulent flows accompany us in our daily lives. Examples of turbulent flow abound in environmental, technological and biological applications. The flow around all kind of vehicles, the jet of fluid entering a swimming pool or jacuzzi, rising smoke from a chimney, blood flow through some arteries, erupting volcano into the atmosphere are all turbulent flows. The atmosphere surrounding our world itself is often turbulent. Some examples of turbulent flows are given in Figures 5.2 to 5.6.

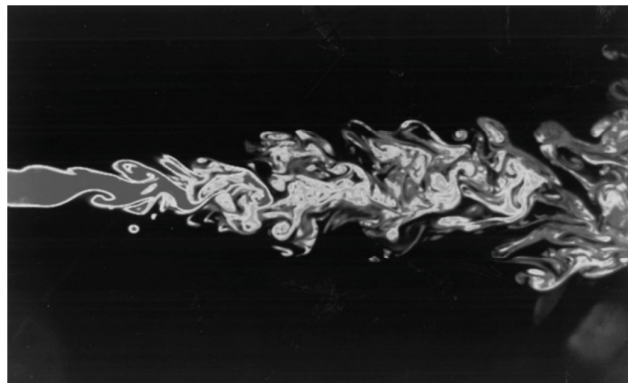


Figure 5.2 Two-dimensional image of an axisymmetric water jet [34]



Figure 5.3 Turbulent eruption of Klyuchevskoy volcano, Russia [35]



Figure 5.4 Turbulent clouds over Carlesbad, New Mexico [36]

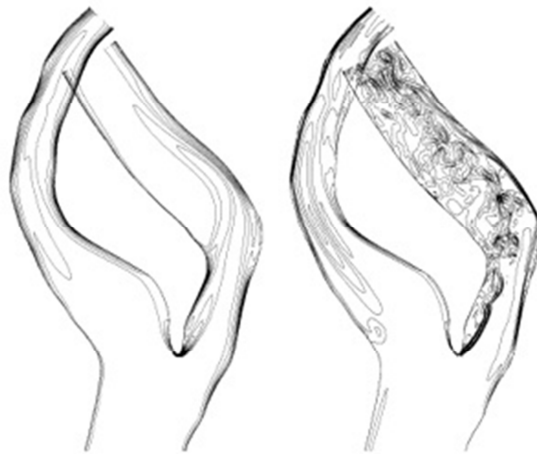


Figure 5.5 Turbulent blood flow in a stenosed carotid artery [37]



Figure 5.6 Visualization of flow over VW Beetle [38]

The momentous difference between laminar and turbulent flows is the occurrence of eddying motions of a wide range of length scales in turbulent flows. A typical flow domain of 0.1 by 0.1 m with a high Reynolds number turbulent flows might contain eddies down to 10 to 100 μm size [25]. To be able to designate processes at all length scales, computational meshes of 10^9 up to 10^{12} points are needed. The fastest events happen with a frequency on the order of 10 kHz therefore time should be discretized into steps of about 100 μs [25]. Speziale [39] states that the direct simulation of a turbulent pipe flow at a Reynolds number of 500000 requires a computer which is 10 million times faster than a current generation CRAY supercomputer. With the present day computing power it has just recently started to become possible to capture the dynamics of very simple turbulent flows at lower Reynolds numbers. The computing requirements for the direct solution of unsteady Navier-Stokes equations of fully turbulent flows at higher Reynolds numbers are truly extraordinary and have to wait for great developments in computer hardware technology [33]. On the other hand, engineers need computational processes which can provide sufficient information about turbulent flows, but which abstained the need to estimate the effects of every single eddy in the flow. Luckily, this category of users is frequently satisfied with information about the time-averaged properties of the flow described below.

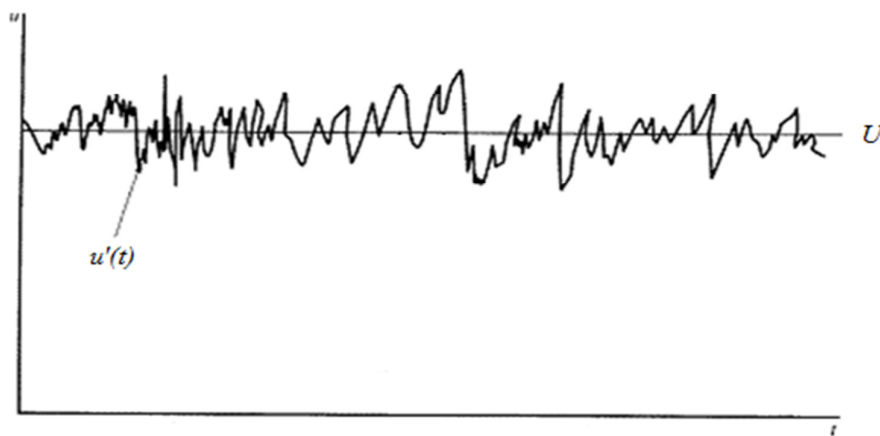


Figure 5.7 Typical point velocity measurement in turbulent flow [25]

In Figure 5.7, a typical point velocity measurement in turbulent flow is shown. The random character of turbulent flows impedes computations based on a complete

explanation of the motion of all fluid particles in the flow. Instead, the velocity in Figure 5.1 can be decomposed into a mean (U) and fluctuating component (u') as, $u(t) = U + u'(t)$. In general, the most appealing way to describe a turbulent flow is using the mean values of flow properties (U, V, W, P etc.) and the statistical properties of their fluctuations (u', v', w', p' etc.) [25].

5.1 Time-Averaged Equations for Turbulent Flows

In order to investigate the effect of turbulent fluctuations on flow properties and to derive time-averaged turbulent flow equations firstly the mean $\bar{\Phi}$ of any flow property ϕ defined as follows

$$\bar{\Phi} = \frac{1}{\Delta t} \int_0^{\Delta t} \phi(t) dt \quad (5.1)$$

The property of flow ϕ is time-dependent and can be considered as a sum of a steady mean component $\bar{\Phi}$ and a time-varying fluctuating component ϕ' . Therefore

$$\phi(t) = \bar{\Phi} + \phi'(t) \quad (5.2)$$

This expression can be written shortly as $\phi = \bar{\Phi} + \phi'$

The time-average of the fluctuations ϕ' is, zero by the definition:

$$\bar{\phi}' = \frac{1}{\Delta t} \int_0^{\Delta t} \phi' dt \equiv 0 \quad (5.3)$$

Before the derivation of the mean flow equations for a turbulent flow, the following rules which govern the time-averages of fluctuating properties $\phi = \bar{\Phi} + \phi'$ and $\psi = \bar{\Psi} + \psi'$ and their combinations, derivatives and integrals are given by using Equations (5.1) and (5.3) as follows,

$$\bar{\phi}' = \bar{\psi}' = 0 \quad (5.4a)$$

$$\bar{\bar{\Phi}} = \bar{\Phi} \quad (5.4b)$$

$$\overline{\phi + \psi} = \bar{\Phi} + \bar{\Psi} \quad (5.4c)$$

$$\overline{\varphi\psi} = \Phi\Psi + \overline{\varphi'\psi'} \quad (5.4d)$$

$$\overline{\varphi\Psi} = \Phi\Psi \quad (5.4e)$$

$$\overline{\varphi'\Psi} = 0 \quad (5.4f)$$

$$\frac{\partial \overline{\varphi}}{\partial s} = \frac{\partial \Phi}{\partial s} \quad (5.4g)$$

$$\overline{\int \varphi ds} = \int \Phi ds \quad (5.4h)$$

Since *div* and *grad* operators are both differentiations, the above rules can be extended to a fluctuating vector quantity $\vec{a} = \vec{A} + \vec{a}'$ and its combinations with a fluctuating scalar $\varphi = \Phi + \varphi'$:

$$\overline{div \vec{a}} = div \vec{A} \quad (5.5a)$$

$$\overline{div(\varphi \vec{a})} = div(\overline{\varphi \vec{a}}) = div(\Phi \vec{A}) + div(\overline{\varphi' \vec{a}'}) \quad (5.5b)$$

$$\overline{div(grad \varphi)} = div(grad \Phi) \quad (5.5c)$$

To express the effects of fluctuations, the flow variables \vec{u} and p in Equation (4.3) and Equations (4.13) to (4.15) are replaced by the sum of mean and fluctuating components. Thus,

$$\vec{u} = \vec{U} + \vec{u}' \quad (5.6a)$$

$$u = U + u' \quad (5.6b)$$

$$v = V + v' \quad (5.6c)$$

$$w = W + w' \quad (5.6d)$$

$$p = P + p' \quad (5.6e)$$

Then the time-average is taken applying the rules stated in Equations (5.5a) to (5.5c). Therefore the continuity equation stated in Equation (4.3) becomes,

$$\overline{\text{div} \vec{u}} = \overline{\text{div}(\vec{U} + \vec{u}')} = 0 \quad (5.7)$$

Using Equation (5.6a), with knowledge of $\overline{\vec{u}'} = 0$,

$$\overline{\text{div} \vec{u}} = \text{div} \vec{U} \quad (5.8)$$

can be written. Then continuity equation for the mean flow becomes,

$$\text{div} \vec{U} = 0 \quad (5.9)$$

A similar process is now carried out on the x -momentum equation stated in Equation (4.13). The time-averages of the individual terms in this equation can be written as follows:

$$\overline{\frac{\partial u}{\partial t}} = \frac{\partial U}{\partial t} \quad (5.10)$$

$$\overline{\text{div}(u\vec{u})} = \text{div}(U\vec{U}) + \text{div}(\overline{u'\vec{u}'}) \quad (5.11)$$

$$-\frac{1}{\rho} \overline{\frac{\partial p}{\partial x}} = -\frac{1}{\rho} \frac{\partial P}{\partial x} \quad (5.12)$$

$$\overline{\nu \text{divgrad} u} = \nu \text{divgrad} U \quad (5.13)$$

If the time-average of x -momentum equation, stated in Equation (4.13), is taken

$$\overline{\frac{\partial u}{\partial t}} + \overline{\text{div}(u\vec{u})} = -\frac{1}{\rho} \overline{\frac{\partial p}{\partial x}} + \overline{\nu \text{div}(grad u)} \quad (5.14)$$

is obtained. Substitution of the terms in Equations (5.10) to (5.13) into Equation (5.14) gives,

$$\underbrace{\frac{\partial U}{\partial t}}_{(i)} + \underbrace{\text{div}(U\vec{U})}_{(ii)} + \underbrace{\text{div}(\overline{u'\vec{u}'})}_{(iii)} = -\underbrace{\frac{1}{\rho} \frac{\partial P}{\partial x}}_{(iv)} + \underbrace{\nu \text{divgrad} U}_{(v)} \quad (5.15)$$

Repetition of this process on Equations (4.14) and (4.15) yields the time-average y and z momentum equations respectively as,

$$\underbrace{\frac{\partial V}{\partial t}}_{(I)} + \underbrace{div(V\bar{U})}_{(II)} + \underbrace{div(\overline{v'u'})}_{(III)} = -\underbrace{\frac{1}{\rho} \frac{\partial P}{\partial y}}_{(IV)} + \underbrace{\nu divgradV}_{(V)} \quad (5.16)$$

$$\underbrace{\frac{\partial W}{\partial t}}_{(I)} + \underbrace{div(W\bar{U})}_{(II)} + \underbrace{div(\overline{w'u'})}_{(III)} = -\underbrace{\frac{1}{\rho} \frac{\partial P}{\partial z}}_{(IV)} + \underbrace{\nu divgradW}_{(V)} \quad (5.17)$$

The terms (I), (II), (IV) and (V) also appear in the instantaneous Equations (4.13) to (4.15). But the process of time-averaging has introduced new terms (III) in the resulting time-averaged momentum equations. The terms involve products of fluctuating velocities and constitute convective momentum transfer due to the velocity fluctuations. If the Equations (5.15) to (5.17) are rearranged to reflect the roles of additional turbulent stresses on the mean velocity components U , V and W , Equations (5.18) to (5.20) are obtained.

$$\frac{\partial U}{\partial t} + div(U\bar{U}) = -\frac{1}{\rho} \frac{\partial P}{\partial x} + \nu divgradU + \left[-\frac{\partial \overline{u'^2}}{\partial x} - \frac{\partial \overline{u'v'}}{\partial y} - \frac{\partial \overline{u'w'}}{\partial z} \right] \quad (5.18)$$

$$\frac{\partial V}{\partial t} + div(V\bar{U}) = -\frac{1}{\rho} \frac{\partial P}{\partial y} + \nu divgradV + \left[-\frac{\partial \overline{u'v'}}{\partial x} - \frac{\partial \overline{v'^2}}{\partial y} - \frac{\partial \overline{v'w'}}{\partial z} \right] \quad (5.19)$$

$$\frac{\partial W}{\partial t} + div(W\bar{U}) = -\frac{1}{\rho} \frac{\partial P}{\partial z} + \nu divgradW + \left[-\frac{\partial \overline{u'w'}}{\partial x} - \frac{\partial \overline{v'w'}}{\partial y} - \frac{\partial \overline{w'^2}}{\partial z} \right] \quad (5.20)$$

The extra stress terms result from six additional stresses, three normal stresses and three shear stresses:

$$\tau_{xx} = -\rho \overline{u'^2} \qquad \tau_{xy} = \tau_{yx} = -\rho \overline{u'v'} \quad (5.21a)$$

$$\tau_{yy} = -\rho \overline{v'^2} \qquad \tau_{xz} = \tau_{zx} = -\rho \overline{u'w'} \quad (5.21b)$$

$$\tau_{zz} = -\rho \overline{w'^2} \qquad \tau_{yz} = \tau_{zy} = -\rho \overline{v'w'} \quad (5.21c)$$

These additional turbulent stresses are named as the Reynolds stresses. In turbulent flows the normal stresses $-\overline{\rho u'^2}$, $-\overline{\rho v'^2}$ and $-\overline{\rho w'^2}$ are always non-zero because they contain squared velocity fluctuations. The shear stresses $-\overline{\rho u'v'}$, $-\overline{\rho u'w'}$ and $-\overline{\rho v'w'}$ are associated with correlations between different velocity components. The turbulent shear stresses are also non-zero and usually very large compared to the viscous stresses in a turbulent flow [25].

In the equations above constant fluid density assumption is made. But generally mean density varies. Bradshaw et al. [40] state that, small density fluctuations do not appear to affect the flow significantly. Hence the density-weighted averaged form of the mean flow equations for compressible turbulent flows where the effects of density fluctuations are negligible but the mean density variations are not can be written as [25],

$$\frac{\partial(\rho U)}{\partial t} + \text{div}(\rho U \bar{U}) = -\frac{\partial P}{\partial x} + \text{div}(\mu \text{grad} U) + \left[-\frac{\partial(\overline{\rho u'^2})}{\partial x} - \frac{\partial(\overline{\rho u'v'})}{\partial y} - \frac{\partial(\overline{\rho u'w'})}{\partial z} \right] \quad (5.22)$$

$$\frac{\partial(\rho V)}{\partial t} + \text{div}(\rho V \bar{U}) = -\frac{\partial P}{\partial y} + \text{div}(\mu \text{grad} V) + \left[-\frac{\partial(\overline{\rho u'v'})}{\partial x} - \frac{\partial(\overline{\rho v'^2})}{\partial y} - \frac{\partial(\overline{\rho v'w'})}{\partial z} \right] \quad (5.23)$$

$$\frac{\partial(\rho W)}{\partial t} + \text{div}(\rho W \bar{U}) = -\frac{\partial P}{\partial z} + \text{div}(\mu \text{grad} W) + \left[-\frac{\partial(\overline{\rho u'w'})}{\partial x} - \frac{\partial(\overline{\rho v'w'})}{\partial y} - \frac{\partial(\overline{\rho w'^2})}{\partial z} \right] \quad (5.24)$$

The symbol ρ stands for the mean density.

5.2 Turbulence Modeling

A turbulence model is a computational procedure to close the system of mean flow equations (Equations 5.22 to 5.24 and 4.2) [25]. In many practical engineering calculations it is redundant to figure out the all details of the turbulent fluctuations. Only the effects of those turbulent fluctuations on the mean flow are generally demanded. Particularly, there is always need expressions for the Reynolds stresses in Equations (5.22) to (5.24). For a turbulence model to be useful in a CFD code it must be simple, accurate, economical and have wide applicability [25]. The most common turbulence models are written below.

- ❖ Mixing length model
- ❖ Spalart-Allmaras model
- ❖ $k-\varepsilon$ model
 - Standard
 - RNG
 - Realizable
- ❖ $k-\omega$ model
 - Standard
 - SST (Shear stress transport)
- ❖ Reynolds stress model
- ❖ Large Eddy Simulation
- ❖ Direct Numerical Simulation

Newton's law of viscosity states, viscous stresses are proportional to the rate of deformation of fluid elements. This gives,

$$\tau_{ij} = \mu \left(\frac{\partial u_i}{\partial x_j} + \frac{\partial u_j}{\partial x_i} \right) \quad (5.25)$$

It was proposed in 1877 by Boussinesq, that Reynolds stresses could be related to mean rates of deformation as

$$\tau_{ij} = -\overline{\rho u_i' u_j'} = \mu_t \left(\frac{\partial U_i}{\partial x_j} + \frac{\partial U_j}{\partial x_i} \right) - \frac{2}{3} \left(\rho k + \mu_t \frac{\partial U_i}{\partial x_j} \right) \delta_{ij} \quad (5.26)$$

where μ_t is a kinematic turbulent or eddy viscosity and k is the turbulent kinetic energy.

5.2.1 Mixing Length Model

Kinematic turbulent viscosity $\nu_t (m^2/s)$ can be expressed as a product of a turbulent velocity scale $v (m/s)$ and a length scale $\ell (m)$. Hence the turbulent viscosity,

$$\nu_t = Cv\ell \quad (5.27)$$

where C is a dimensionless constant of proportionality. The velocity scale for a simple turbulent flows where the only significant Reynolds stress is $\tau_{xy} = \tau_{yx} = -\rho \overline{u'v'}$ and the only significant mean velocity gradient is $\frac{\partial U}{\partial y}$, can be written as

$$v = c\ell \left| \frac{\partial U}{\partial y} \right| \quad (5.28)$$

where c is a dimensionless constant.

By blending Equations (5.27) and (5.28) and absorbing the constants C and c into a new length scale ℓ_m , a new expression can be obtained as,

$$\nu_t = \ell_m^2 \left| \frac{\partial U}{\partial y} \right| \quad (5.29)$$

This is Prandtl's mixing length model. ℓ_m can be expressed as simple algebraic formulae for some two-dimensional flows. These algebraic formulae are given in Table 5.1.

Table 5.1 Mixing lengths for some two-dimensional simple flows [25]

Flow	Mixing length ℓ_m	L
Mixing layer	$0.07 L$	Layer width
Jet	$0.09 L$	Jet half width
Wake	$0.16 L$	Wake half width
Axisymmetric jet	$0.075 L$	Jet half width
Pipes and channels (fully developed flow)	$L \left[0.14 - 0.08(1 - y/L)^2 - 0.06(1 - y/L)^4 \right]$	Pipe radius or channel half width

In Table 5.1, y stand for the distance from the wall. Using Boussinesq approach with noting that $\frac{\partial U}{\partial y}$ is the only important mean velocity gradient, the turbulent Reynolds stress is described by

$$\tau_{xy} = \tau_{yx} = -\rho \overline{u'v'} = \rho \ell_m^2 \left| \frac{\partial U}{\partial y} \right| \frac{\partial U}{\partial y} \quad (5.30)$$

The mixing length is very useful in flows where the turbulence properties develop in proportion to a mean flow length scale, so that ℓ_m can be described as a function of position by means of a simple algebraic formula. This explains its popularity in calculations of flows around wing sections. Successful modifications of the formulae for ℓ_m to designate the effects of small scale separations, pressure gradients, and boundary layer blowing and suction are available [25]. Models conducted by Baldwin and Lomax [41] and Cebeci and Smith [42] are the most popular turbulence models in the aerospace industry.

In 2-D thin shear layers the variations in the direction of flow are very slow that the turbulence can adapt itself to local conditions [25]. If the diffusion and convection of turbulence properties can be neglected, the effect of turbulence on the mean flow can be expressed in terms of the mixing length. If diffusion and convection are considerable, the mixing length is no longer applicable.

5.2.2 Standard k - ε Model

The standard k - ε model is a semi-empirical turbulence model based on two transport equations for the turbulence kinetic energy k and its dissipation rate ε . The transport equation for turbulence kinetic energy (k) is derived from the exact equation on the other hand the transport equation for dissipation rate ε is acquired by using physical reasoning [43].

For turbulent flows; the instantaneous kinetic energy $k(t)$ can be expressed as a sum of mean kinetic energy K and the turbulent kinetic energy k . These terms can be expressed as,

$$k(t) = K + k \quad (5.31)$$

$$K = \frac{1}{2}(U^2 + V^2 + W^2) \quad (5.32)$$

$$k = \frac{1}{2}(\overline{u'^2 + v'^2 + w'^2}) \quad (5.33)$$

Similarly, the rate of deformation of a fluid element in a turbulent flow can be expressed with mean and fluctuating components as,

$$e_{ij}(t) = E_{ij} + e'_{ij} \quad (5.34)$$

where,

$$e_{xx}(t) = E_{xx} + e'_{xx} = \frac{\partial U}{\partial x} + \frac{\partial u'}{\partial x} \quad (5.35a)$$

$$e_{yy}(t) = E_{yy} + e'_{yy} = \frac{\partial V}{\partial y} + \frac{\partial v'}{\partial y} \quad (5.35b)$$

$$e_{zz}(t) = E_{zz} + e'_{zz} = \frac{\partial W}{\partial z} + \frac{\partial w'}{\partial z} \quad (5.35c)$$

$$e_{xy}(t) = e_{yx}(t) = E_{xy} + e'_{yx} = \frac{1}{2}\left(\frac{\partial U}{\partial y} + \frac{\partial V}{\partial x}\right) + \frac{1}{2}\left(\frac{\partial u'}{\partial y} + \frac{\partial v'}{\partial x}\right) \quad (5.35d)$$

$$e_{xz}(t) = e_{zx}(t) = E_{xz} + e_{zx}' = \frac{1}{2} \left(\frac{\partial U}{\partial z} + \frac{\partial W}{\partial x} \right) + \frac{1}{2} \left(\frac{\partial u'}{\partial z} + \frac{\partial w'}{\partial x} \right) \quad (5.35e)$$

$$e_{yz}(t) = e_{zy}(t) = E_{yz} + e_{yz}' = \frac{1}{2} \left(\frac{\partial V}{\partial z} + \frac{\partial W}{\partial y} \right) + \frac{1}{2} \left(\frac{\partial v'}{\partial z} + \frac{\partial w'}{\partial y} \right) \quad (5.35f)$$

An equation for the mean kinetic energy K can be acquired by multiplying Equation (5.18) by U , Equation (5.19) by V and Equation (5.20) by W [44]. After adding the results with some algebraic rearrangements, time-averaged equation governing the mean kinetic energy of the flow can be obtained as follows.

$$\frac{\partial}{\partial t}(\rho K) + \text{div}(\rho K \bar{U}) = \text{div} \left(-P \bar{U} + 2\mu \bar{U} E_{ij} - \rho \bar{U} \overline{u'_i u'_j} \right) - 2\mu E_{ij} \cdot E_{ij} + \overline{\rho u'_i u'_j} \cdot E_{ij} \quad (5.36)$$

Similarly, the governing equation for turbulent kinetic energy k can be obtained by multiplication of each of the instantaneous Navier-Stokes equations, Equations (4.13) to (4.15), by the proper fluctuating velocity components and addition of all the results, followed by a repeat of this process on the Reynolds equations, Equations (5.18) to (5.20), subtraction of the two resulting equations and some rearrangements as [25],

$$\frac{\partial}{\partial t}(\rho k) + \text{div}(\rho k \bar{U}) = \text{div} \left(-\overline{p' \bar{u}'} + 2\mu \overline{\bar{u}' e'_{ij}} - \frac{1}{2} \overline{\rho u'_i \cdot u'_i u'_j} \right) - 2\mu \overline{e'_{ij} \cdot e'_{ij}} - \overline{\rho u'_i u'_j} \cdot E_{ij} \quad (5.37)$$

The last two terms of the right hand side of the Equations (5.36) and (5.37) are named as dissipation and production of mean kinetic energy K and turbulent kinetic energy k respectively. The last terms in both equations are equal in magnitude, but opposite in sign. In two dimensional thin shear layers, it was founded that when mean velocity gradient $\partial U / \partial y$ is positive then the term $-\overline{\rho u' v'}$ is also positive. Hence that term gives a positive contribution in the turbulent kinetic energy equation and symbolizes a production term. However, in the K equation the term is negative, hence it destroys mean flow kinetic energy [25]. This describes the conversion of mean kinetic energy into turbulent kinetic energy mathematically. The term $-\overline{2\mu e'_{ij} \cdot e'_{ij}}$, viscous dissipation, gives a negative contribution to k equation.

The rate of dissipation per unit mass, whose dimensions are $\varepsilon(m^2/s^3)$, is of vital value in the field of turbulence mechanics and is expressed as

$$\varepsilon = 2\nu \overline{e'_{ij} \cdot e'_{ij}} \quad (5.38)$$

In standard k - ε model, Launder and Spalding [45] states two model equations for k and ε . In this model k and ε are used to define velocity scale $v(m/s)$ and length scale $\ell(m)$ as follows,

$$v = k^{1/2} \quad \text{and} \quad \ell = \frac{k^{3/2}}{\varepsilon} \quad (5.39)$$

Carrying out the similar way as in the mixing length model, the turbulent viscosity can be defined as,

$$\mu_t = C\rho v\ell = \rho C_\mu \frac{k^2}{\varepsilon} \quad (5.40)$$

where C_μ is a dimensionless constant.

The standard k - ε model uses the following transport equations used for k and ε :

$$\frac{\partial k}{\partial t} + U_j \frac{\partial k}{\partial x_j} = \tau_{ij} \frac{\partial U_i}{\partial x_j} - \varepsilon + \frac{\partial}{\partial x_j} \left((v + v_t / \sigma_k) \frac{\partial k}{\partial x_j} \right) \quad (5.41)$$

$$\frac{\partial \varepsilon}{\partial t} + U_j \frac{\partial \varepsilon}{\partial x_j} = C_{\varepsilon 1} \frac{\varepsilon}{k} \tau_{ij} \frac{\partial U_i}{\partial x_j} - C_{\varepsilon 2} \frac{\varepsilon^2}{k} + \frac{\partial}{\partial x_j} \left((v + v_t / \sigma_\varepsilon) \frac{\partial \varepsilon}{\partial x_j} \right) \quad (5.42)$$

where the closure coefficients are

$$C_{\varepsilon 1} = 1.44 \quad C_{\varepsilon 2} = 1.92 \quad C_\mu = 0.09 \quad \sigma_k = 1.0 \quad \sigma_\varepsilon = 1.3 \quad (5.43)$$

5.2.3 RNG k - ε Model

Over the years the standard k - ε turbulence model has proved to be both robust and economical. However, it has its deficiencies, such as the incapability to estimate highly strained flow, swirling flow, rotating and separating flow. But, because of the deficiencies of the standard k - ε model, refinements have been made to overcome such issues, which lead to the development of the RNG k - ε model.

The RNG k - ε model was developed using a statistical approach called as Renormalization Group (RNG) methods. The main objective of the development of this turbulence model was to modify the kinematic eddy viscosity and the dissipation transport equation so that they are able to fixed to highly strained flows. The RNG procedure systematically removes the small scales of motion from the governing equations by expressing their effects in terms of larger scale motions and modified viscosity [25].

The RNG k - ε model equations are as follows,

$$\mu_t = \rho C_\mu \frac{k^2}{\varepsilon} \quad (5.44)$$

$$\frac{\partial k}{\partial t} + U_j \frac{\partial k}{\partial x_j} = \tau_{ij} \frac{\partial U_i}{\partial x_j} - \varepsilon + \frac{\partial}{\partial x_j} \left(\alpha_k \mu_{eff} \frac{\partial k}{\partial x_j} \right) \quad (5.45)$$

$$\frac{\partial \varepsilon}{\partial t} + U_j \frac{\partial \varepsilon}{\partial x_j} = C_{1\varepsilon} \frac{\varepsilon}{k} \tau_{ij} \frac{\partial U_i}{\partial x_j} - C_{2\varepsilon} \frac{\varepsilon^2}{k} + \frac{\partial}{\partial x_j} \left(\alpha_k \mu_{eff} \frac{\partial \varepsilon}{\partial x_j} \right) \quad (5.46)$$

where the closure coefficients and auxiliary functions are given as:

$$C_{2\varepsilon}^* = C_{2\varepsilon} + \frac{C_\mu \lambda^3 (1 - \lambda/\lambda_0)}{1 + \beta \lambda^3} \quad \lambda \equiv \frac{k}{\varepsilon} \sqrt{2S_{ij}S_{ji}} \quad (5.47)$$

$$C_{1\varepsilon} = 1.42 \quad C_{2\varepsilon} = 1.68 \quad C_\mu = 0.085 \quad (5.48)$$

$$\sigma_k = \sigma_\varepsilon = 0.72 \quad \beta = 0.012 \quad \lambda_0 = 4.38 \quad (5.49)$$

For highly strained mean flow, the RNG $k-\varepsilon$ model modified the closure coefficient in the dissipation term of the dissipation transport equation. Instead of taking $C_{2\varepsilon}$ as a constant, it has been modified to include mean strain effect. In highly strained mean flow, $C_{2\varepsilon}^*$ will be smaller than $C_{2\varepsilon}$, therefore reducing the effect of dissipation in the dissipation term. This will result in a reduction in the mean turbulent kinetic energy effect and therefore reducing the turbulent eddy viscosity value, μ_t . This will reduce the over diffusive behaviour, experienced in the standard $k-\varepsilon$ model [33].

5.2.4 Realizable $k-\varepsilon$ Model

Although the RNG $k-\varepsilon$ model is an improvement of the standard $k-\varepsilon$ model, it still has limitations. This is due to the transport equation for the dissipation term, ε . Because of the fact that the transport equation for the dissipation term is derived based on physical reasoning and dimensional analysis alone, certain mathematical limitations exist and needs to be satisfied in order to be consistent with the prediction of Reynolds stresses, therefore the turbulence flow [43]. The RNG and standard $k-\varepsilon$ models do not handle these mathematical limitations. Because of that, in 1995 the realizable $k-\varepsilon$ model was developed. In that model, turbulent eddy viscosity term (μ_t) is also modified for adjusting different flow conditions.

The Realizable $k-\varepsilon$ model is defined as:

$$\nu_t = C_\mu \frac{k^2}{\varepsilon} \quad (5.50)$$

$$\frac{\partial k}{\partial t} + U_j \frac{\partial k}{\partial x_j} = \tau_{ij} \frac{\partial U_i}{\partial x_j} - \varepsilon + \frac{\partial}{\partial x_j} \left[\left(\nu + \frac{\nu_T}{\sigma_k} \right) \frac{\partial k}{\partial x_j} \right] \quad (5.51)$$

$$\frac{\partial \varepsilon}{\partial t} + U_j \frac{\partial \varepsilon}{\partial x_j} = C_1 S \varepsilon - C_2 \frac{\varepsilon^2}{k + \sqrt{\nu \varepsilon}} + \frac{\partial}{\partial x_j} \left[\left(\nu + \frac{\nu_T}{\sigma_\varepsilon} \right) \frac{\partial \varepsilon}{\partial x_j} \right] \quad (5.52)$$

where the closure coefficients and the formulation for C_μ are defined as:

$$C_1 = \max \left[0.43, \frac{\eta}{\eta + 5} \right] \quad \eta = S \frac{k}{\varepsilon} \quad C_2 = 1.9 \quad \sigma_k = 1.0 \quad \sigma_\varepsilon = 1.2 \quad (5.53)$$

$$C_\mu = \frac{1}{A_0 + A_s \frac{kU^*}{\varepsilon}} \quad A_0 = 4.04 \quad A_s = \sqrt{6} \cos \phi \quad (5.54)$$

$$\phi = \frac{1}{3} \cos^{-1}(\sqrt{6}W) \quad W = \frac{S_{ij}S_{jk}S_{ki}}{\tilde{S}} \quad \tilde{S} = \sqrt{S_{ij}S_{ij}} \quad (5.55)$$

$$S_{ij} = \frac{1}{2} \left(\frac{\partial U_i}{\partial x_j} + \frac{\partial U_j}{\partial x_i} \right) \quad U^* \equiv \sqrt{S_{ij}S_{ij} + \Omega_{ij}\Omega_{ij}} \quad \Omega_{ij} = \overline{\Omega_{ij}} - \varepsilon_{ijk} \omega_k \quad (5.56)$$

From the equations above, it can be seen that the transport equation of the dissipation term is different from the standard and RNG k - ε models. The dissipation term was modified so that the denominator will not be singular, eliminating the probability of the dissipation term of becoming too big. This will provide a reasonable value for dissipation in the k transport equation and therefore overcoming the problem of non-decaying eddy viscosity [33].

5.2.5 Standard k - ω Model

Standard k - ω is an experimental model that based on turbulent kinetic energy k and specific dissipation ω equations.

$$v_t = \frac{k}{\omega} \quad (5.57)$$

$$\frac{\partial k}{\partial t} + U_j \frac{\partial k}{\partial x_j} = \tau_{ij} \frac{\partial U_i}{\partial x_j} - \beta^* k \omega + \frac{\partial}{\partial x_j} \left[(v + \sigma^* v_t) \frac{\partial k}{\partial x_j} \right] \quad (5.58)$$

$$\frac{\partial \omega}{\partial t} + U_j \frac{\partial \omega}{\partial x_j} = \alpha \frac{\omega}{k} \tau_{ij} \frac{\partial U_i}{\partial x_j} - \beta \omega^2 + \frac{\partial}{\partial x_j} \left[(v + \sigma^* v_t) \frac{\partial \omega}{\partial x_j} \right] \quad (5.59)$$

where the closure coefficients are obtained empirically. The closure coefficients and auxiliary relations are further defined as:

$$\alpha = \frac{13}{25}, \beta = \beta_0 f_\beta \quad \beta^* = \beta_0^* f_{\beta^*} \quad \sigma = \sigma^* = \frac{1}{2} \quad (5.60)$$

$$\beta_0 = \frac{9}{125} \quad f_\beta = \frac{1+70\chi_\omega}{1+80\chi_\omega} \quad \chi_\omega \equiv \left| \frac{\Omega_{ij}\Omega_{jk}S_{ki}}{(\beta_0^*\omega)^3} \right| \quad (5.61)$$

$$\beta_0^* = \frac{9}{100} \quad f_{\beta^*} = \begin{cases} 1 & , \chi_k \leq 0 \\ \frac{1+680\chi_k^2}{1+400\chi_k^2} & , \chi_k > 0 \end{cases} \quad (5.62)$$

$$\chi_k \equiv \frac{1}{\omega^3} \frac{\partial k}{\partial x_j} \frac{\partial \omega}{\partial x_j} \quad (5.63)$$

5.2.6 SST k - ω Model

The shear stress transport (SST) k - ω turbulence model is a two-equation eddy viscosity model. The SST formulation blends the two turbulence models. The use of a standard k - ω formulation in the inner parts of the boundary layer makes the model suitable all the way down to the wall through the viscous sublayer, hence the SST k - ω model can be used as a low Reynolds number turbulence model [15]. The SST formulation also converts to a k - ϵ behaviour in the turbulent core region. Therefore it avoids the general k - ω issue which is the sensitivity of the model to the free stream turbulence properties. SST k - ω model gives fine results in separating flows and adverse pressure gradients [15].

$$v_T = \frac{\alpha_1 k}{\max(\alpha_1 \omega, SF_2)} \quad (5.64)$$

$$\frac{\partial k}{\partial t} + U_j \frac{\partial k}{\partial x_j} = P_k - \beta^* k \omega + \frac{\partial}{\partial x_j} \left[(v + \sigma_k v_T) \frac{\partial k}{\partial x_j} \right] \quad (5.65)$$

$$\frac{\partial \omega}{\partial t} + U_j \frac{\partial \omega}{\partial x_j} = \alpha S^2 - \beta \omega^2 + \frac{\partial}{\partial x_j} \left[(v + \sigma_\omega v_T) \frac{\partial \omega}{\partial x_j} \right] + 2(1-F_1) \sigma_{\omega 2} \frac{1}{\omega} \frac{\partial k}{\partial x_i} \frac{\partial \omega}{\partial x_i} \quad (5.66)$$

where the closure coefficients and auxiliary functions are given as:

$$F_2 = \tanh \left[\left[\max \left(\frac{2\sqrt{k}}{\beta^* \omega y}, \frac{500v}{y^2 \omega} \right) \right]^2 \right] \quad (5.67)$$

$$P_k = \min \left(\tau_{ij} \frac{\partial U_i}{\partial x_j}, 10\beta^* k\omega \right) \quad (5.68)$$

$$F_1 = \tanh \left\{ \left[\min \left[\max \left(\frac{\sqrt{k}}{\beta^* \omega y}, \frac{500\nu}{y^2 \omega} \right), \frac{4\sigma_{\omega 2} k}{CD_{k\omega} y^2} \right] \right]^4 \right\} \quad (5.69)$$

$$CD_{k\omega} = \max \left(2\rho\sigma_{\omega 2} \frac{1}{\omega} \frac{\partial k}{\partial x_i} \frac{\partial \omega}{\partial x_i}, 10^{-10} \right) \quad (5.70)$$

$$\phi = \phi_1 F_1 + \phi_2 (1 - F_1) \quad (5.71)$$

$$\alpha_1 = \frac{5}{9} \quad \alpha_2 = 0.44 \quad \beta^* = \frac{9}{100} \quad (5.72)$$

$$\alpha_{k1} = 0.85 \quad \alpha_{k2} = 1 \quad (5.73)$$

$$\alpha_{\omega 1} = 0.5 \quad \alpha_{\omega 2} = 0.856 \quad (5.74)$$

5.2.7 Spalart–Allmaras Model

Spalart–Allmaras model is a simple one-equation turbulence model which solves a transport equation for the kinematic turbulent viscosity. This exhibits a new category of one-equation models in which calculating a length scale is not necessary. This model was designed especially for external aerospace applications. It gives good results for boundary layers with adverse pressure gradients. In recent years it becomes popular for turbomachinery applications [15].

In Spalart–Allmaras model, the transported variable ($\tilde{\nu}$) is equal to the turbulent kinematic viscosity except in the near wall region. The transport equation for $\tilde{\nu}$ is;

$$\begin{aligned} \frac{\partial \tilde{\nu}}{\partial t} + U_j \frac{\partial \tilde{\nu}}{\partial x_j} = & C_{b1} (1 - f_{t2}) \tilde{S} \tilde{\nu} - \left[C_{\omega 1} f_{\omega} - \frac{C_{b1}}{\kappa^2} f_{t2} \right] \left(\frac{\tilde{\nu}}{d} \right)^2 \\ & + \frac{1}{\sigma} \left[\frac{\partial}{\partial x_j} \left((\nu + \tilde{\nu}) \frac{\partial \tilde{\nu}}{\partial x_j} \right) + C_{b2} \frac{\partial \tilde{\nu}}{\partial x_i} \frac{\partial \tilde{\nu}}{\partial x_i} \right] \end{aligned} \quad (5.75)$$

and the turbulent eddy viscosity is computed from,

$$\mu_t = \rho \tilde{\nu} f_{v1} \quad (5.76)$$

where

$$f_{v1} = \frac{\chi^3}{\chi^3 + C_{v1}^3} \quad (5.77)$$

$$\chi = \frac{\tilde{\nu}}{\nu} \quad (5.78)$$

and ρ is the density, $\nu = \mu/\rho$ is the molecular kinematic viscosity and μ is the molecular dynamic viscosity. Additional definitions are given by the following equations:

$$\tilde{S} = \Omega + \frac{\tilde{\nu}}{\kappa^2 d^2} f_{v2} \quad (5.79)$$

where

$$\Omega = \sqrt{2W_{ij}W_{ij}} \quad (5.80)$$

is the magnitude of the vorticity, d is the distance from the field point to the nearest wall, and

$$f_{v2} = 1 - \frac{\chi}{1 + \chi f_{v1}} \quad (5.81)$$

$$f_{\omega} = g \left[\frac{1 + C_{\omega3}^6}{g^6 + C_{\omega3}^6} \right]^{1/6} \quad (5.82)$$

$$g = r + C_{\omega2} (r^6 - r) \quad (5.83)$$

$$r = \min \left[\frac{\tilde{\nu}}{\tilde{S} \kappa^2 d^2}, 10 \right] \quad (5.84)$$

$$f_{t2} = C_{t3} \exp(-C_{t4} \chi^2) \quad (5.85)$$

$$W_{ij} = \frac{1}{2} \left(\frac{\partial U_i}{\partial x_j} - \frac{\partial U_j}{\partial x_i} \right) \quad (5.86)$$

The constants are

$$C_{b1} = 0.1355 \quad \sigma = 2/3 \quad C_{b2} = 0.622 \quad \kappa = 0.41 \quad (5.87)$$

$$C_{\omega2} = 0.3 \quad C_{\omega3} = 2 \quad C_{v1} = 7.1 \quad C_{t3} = 1.2 \quad (5.88)$$

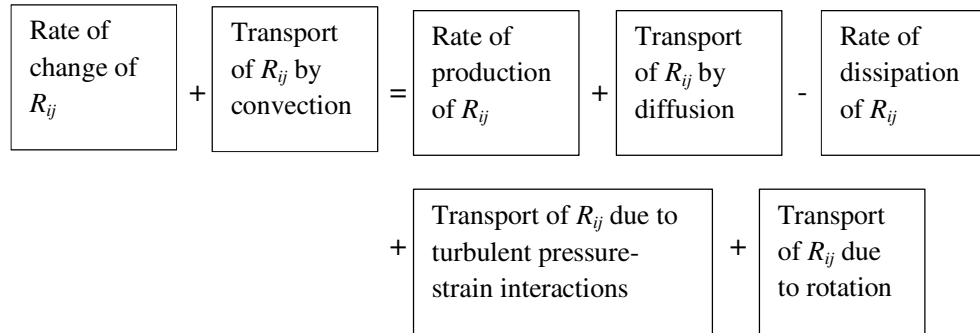
$$C_{t4} = 0.5 \quad C_{\omega1} = \frac{C_{b1}}{\kappa^2} + \frac{1 + C_{b2}}{\sigma} \quad (5.89)$$

5.2.8 Reynolds Stress Model

The Reynolds stress model (RSM) is the most complicated Reynolds averaging based turbulence model. Without using the isotropic turbulent viscosity hypothesis, the RSM closes the Reynolds averaged Navier-Stokes (RANS) equations by solving transport equations for the Reynolds stresses, together with an equation for the dissipation rate. This means five and seven extra transport equations are required in 2-D and 3-D flows respectively.

The exact equation for the transport of Reynolds stress, $R_{ij} = -\frac{\tau_{ij}}{\rho} = \overline{u'_i u'_j}$, given in the following form,

$$\frac{DR_{ij}}{Dt} = P_{ij} + D_{ij} - \varepsilon_{ij} + \Pi_{ij} + \Omega_{ij} \quad (5.90)$$



For the six independent Reynolds stresses, Equation (5.90) represents six partial differential equations.

Computational fluid dynamics computations with the Reynolds stress transport equations retain the production term in its exact form [25]

$$P_{ij} = - \left(R_{im} \frac{\partial U_j}{\partial x_m} + R_{jm} \frac{\partial U_i}{\partial x_m} \right) \quad (5.91)$$

To obtain a solvable form of Equation (5.90); models for the dissipation rate, diffusion, and pressure-strain correlation terms on the right hand side are needed.

The diffusion term D_{ij} can be modelled with the assumption that the rate of transport of Reynolds stresses by diffusion is proportional to the gradients of Reynolds stresses. Commercial CFD codes often favour the simplest form

$$D_{ij} = \frac{\partial}{\partial x_m} \left(\frac{\nu_t}{\sigma_k} \frac{\partial R_{ij}}{\partial x_m} \right) = \text{div} \left(\frac{\nu_t}{\sigma_k} \text{grad} (R_{ij}) \right) \quad (5.92)$$

$$\text{with } \nu_t = C_\mu \frac{k^2}{\varepsilon} \quad C_\mu = 0.09 \quad \sigma_k = 1.0 \quad (5.93)$$

The dissipation rate ε_{ij} is modelled with the assumption of isotropy of the small dissipative eddies. It is set so that it affects the normal Reynolds stresses ($i=j$) only and in equal measure [25]. This can be achieved by

$$\varepsilon_{ij} = \frac{2}{3} \varepsilon \delta_{ij} \quad (5.94)$$

where ε the dissipation rate of turbulent kinetic energy is defined by Equation (5.38) and δ_{ij} is the Kronecker's delta.

The pressure-strain interactions are the most arduous and important term in Equation (5.90). A comprehensive model that accounts for all the effects of pressure-strain interactions on Reynolds stresses is given in Launder et al. [46]. They also give the following simpler form favoured by some commercially available CFD codes:

$$\Pi_{ij} = -C_1 \frac{\varepsilon}{k} \left(R_{ij} - \frac{2}{3} k \delta_{ij} \right) - C_2 \left(P_{ij} - \frac{2}{3} P \delta_{ij} \right) \quad (5.95)$$

with $C_1 = 1.8$ and $C_2 = 0.6$

The rotational term is given by

$$\Omega_{ij} = -2\omega_k \left(R_{jm} e_{ikm} + R_{im} e_{jkm} \right) \quad (5.96)$$

where ω_k is the rotation vector and e_{ijk} is the alternating symbol.

Turbulent kinetic energy k is needed in the Equation (5.95) and can be found by adding the three normal stresses together

$$k = \frac{1}{2} (R_{11} + R_{22} + R_{33}) = \frac{1}{2} (\overline{u_1'^2} + \overline{u_2'^2} + \overline{u_3'^2}) \quad (5.97)$$

5.2.9 Direct Numerical Simulation and Large Eddy Simulation

The ideal method to obtain accurate results for turbulence flow is to directly solve for the Reynolds stresses and in turn the non-linear Navier-Stokes and continuity equations. This can be achieved by using either the method of Direct Numerical Simulation (DNS) or by using Large Eddy Simulation (LES). DNS and LES are also known as the unsteady viscous methods [33].

In DNS, unsteady Navier Stokes equations are solved directly without any modeling of the turbulence. The fluctuating velocity and viscous force components within the body surface and in the computational domain is obtained together with components of Reynolds stresses. On the other hand, the LES approach directly solves the large eddies motions using the unsteady Navier-Stokes equations and models the small eddies. The motivation behind this lie on the fact that small eddies has a more universal character. They are more isotropic and dissipative in nature, which makes its behaviour independent to the flow. Large eddies are highly anisotropic and unsteady in nature, which makes it dependent to the flow [33].

DNS requires grid points that increase with 9/4 power of Reynolds number. For instance; it has been estimated that to capture the effect of the smallest turbulence motion and solves the flow around a vehicle, grid points around 10^{18} would be needed. This value makes DNS so impractical in using vehicle aerodynamics in the immediate future [16].

LES approach is a more preferred option because it requires significantly less computer capacity than DNS, and yet at the same time promises to be more accurate and robust than the conventional RANS approach.

5.3 Near Wall Treatment

The existence of the wall affects the turbulent flow characteristics significantly. This because the no slip condition has to be satisfied at the wall boundaries. Near a wall, viscous damping reduces tangential velocity fluctuations on the other hand kinematic blocking reduces the normal fluctuations. Nevertheless, outside the boundary layer turbulence quickly grows up by the production of turbulence kinetic energy (k) due to the large gradients in the mean velocity.

Turbulence models are divided into two categories which are high Reynolds number and low Reynolds number models. High Reynolds number models are designed to solve turbulent core flows and they need wall functions to model the near wall region. Unlike high Re models, low Re models both cover the turbulent core and near wall region in their formulations and do not need wall functions. RSM and $k-\varepsilon$ models are both high Reynolds number models whereas the $k-\omega$ models and Spalart-Allmaras are low Re number models.

The use of wall functions reduces the computational time and memory requirements as the near wall region is calculated by wall functions. This way, very fine grid near the wall region is not necessary.

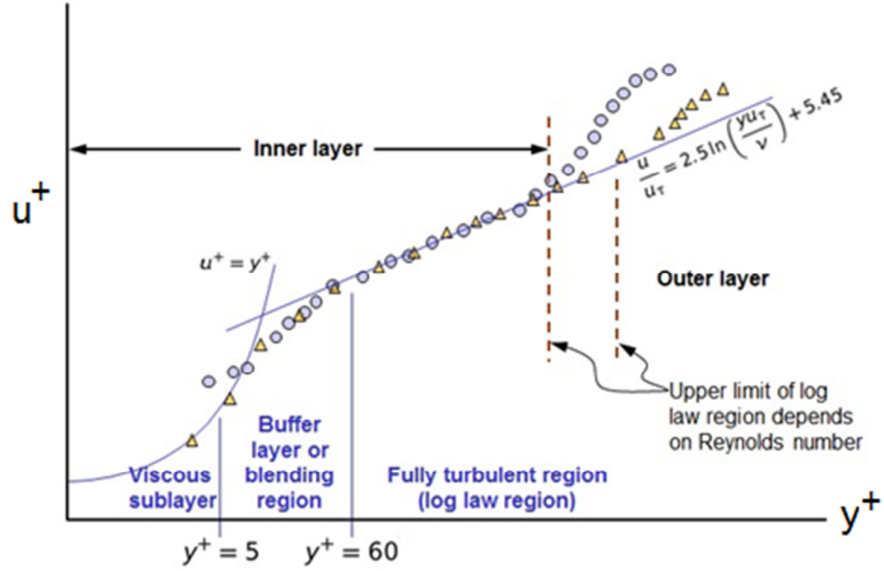


Figure 5.8 Subdivisions of near wall region [15]

In Figure 5.8, u^+ is the non-dimensional velocity and y^+ is the non-dimensional distance of the cell to the wall where

$$u^+ = \frac{u}{u_\tau} \quad (5.98)$$

$$y^+ = \frac{yu_\tau}{\nu} \quad (5.99)$$

$$u_\tau = \sqrt{\frac{\tau_{wall}}{\rho}} \quad (5.100)$$

In Equations (5.98) to (5.100); u_τ is the friction velocity, y is the distance from the cell to the wall and τ_{wall} is the wall shear stress.

The measure of the physical distance from the wall is determined by y^* value and it is formulated as,

$$y^* = \frac{\rho C_\mu^{1/4} k_p^{1/2} y_p}{\mu} \quad (5.101)$$

where

ρ : density of the fluid

C_μ : modeling constant (=0.09)

k_p : turbulent kinetic energy at point P

y_p : distance from point P to the wall

μ : dynamic viscosity of the fluid

Fluent provides two wall functions namely standard wall function and non-equilibrium wall function. These wall functions are valid in the range of $30 < y^* < 300$ and the distance of the centroid of wall adjacent cells should be adjusted to fall in this range.

CHAPTER 6

CFD SIMULATIONS

In this chapter, in order to test the reliability of turbulence models and compare the performances of them; an aerodynamic CFD analysis with several turbulence models of a model car was made by simulating the wind tunnel tests of Aka [4] which was conducted with the same car model. At the end of the simulations; streamlines, velocity and pressure distributions were determined for different sections in the solution domain. Besides drag and pressure coefficients were found for different velocities.

6.1 Vehicle Model

In this study, a model of BMW 3-series passenger car having a geometric scale of 1/16 was used. A CAD model of a car which was drawn by using Rhinoceros and Catia softwares can be seen from different views in Figures 6.1 to 6.5. For simplicity, in CFD analyses some details were extracted from the CAD model.

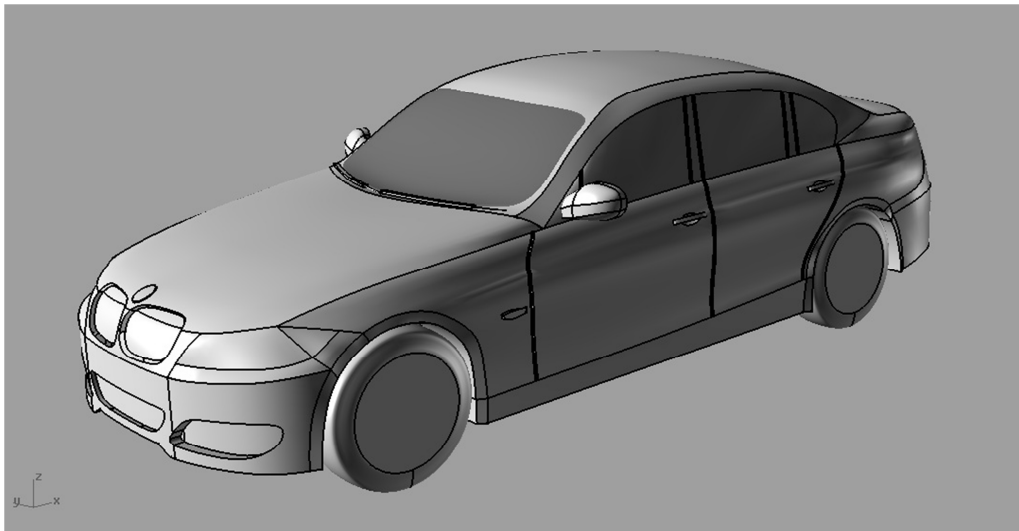


Figure 6.1 CAD model of the car (front perspective view)

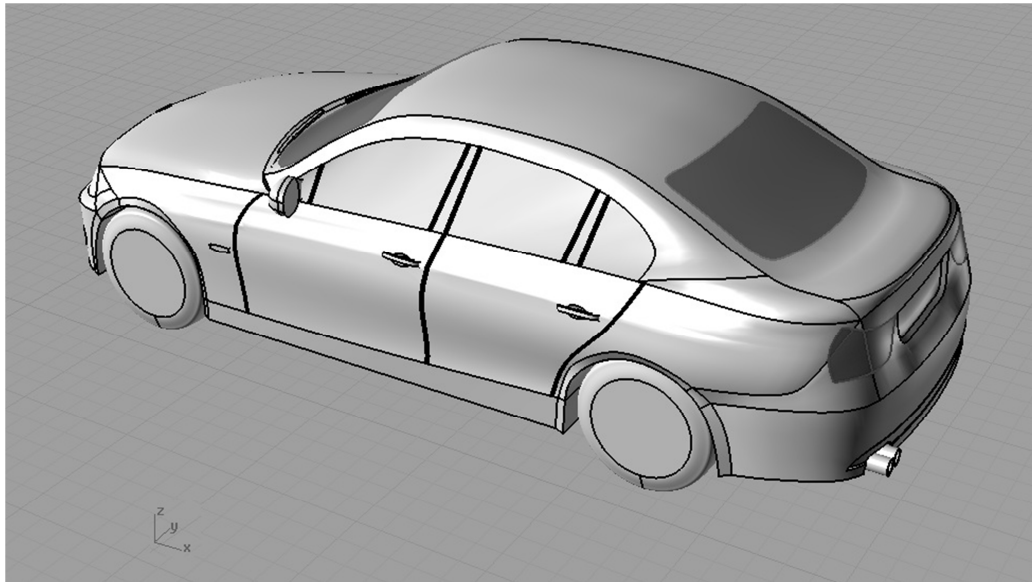


Figure 6.2 CAD model of the car (rear perspective view)

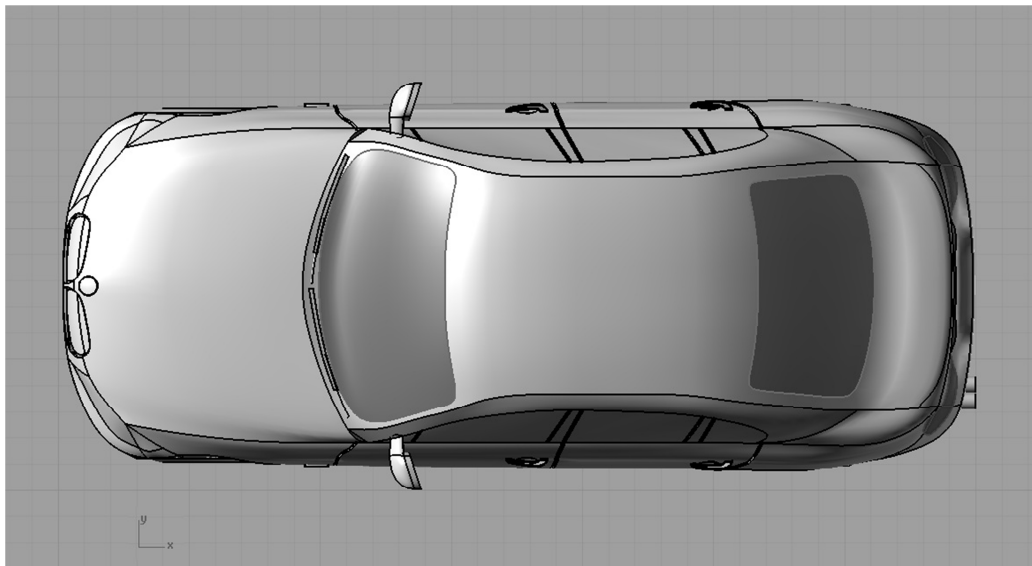


Figure 6.3 CAD model of the car (top view)

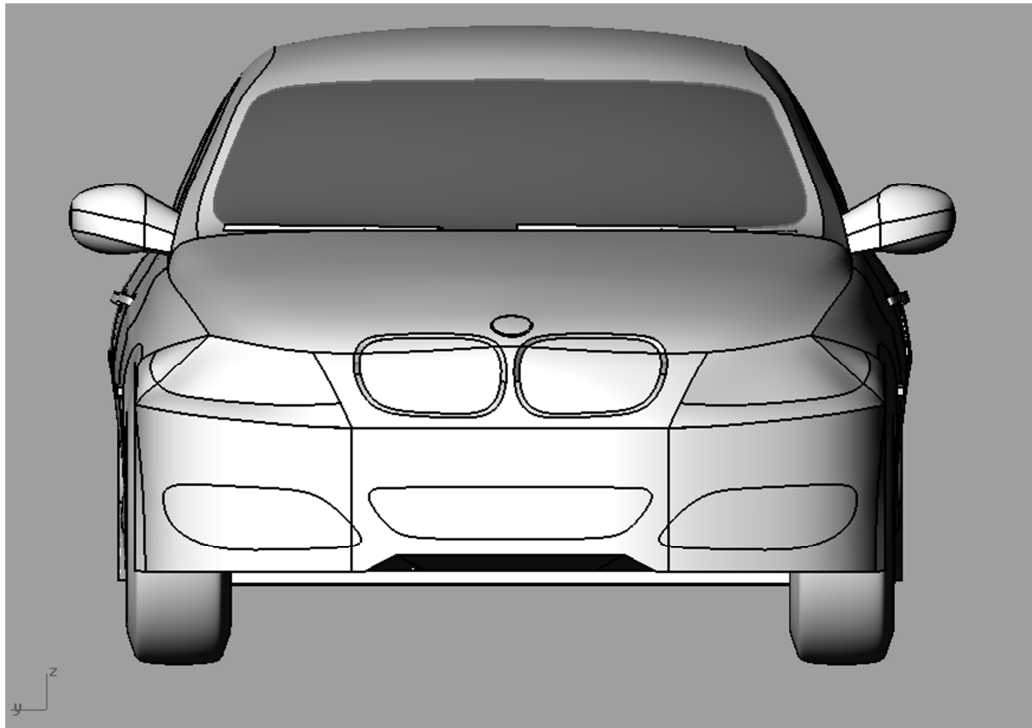


Figure 6.4 CAD model of the car (front view)

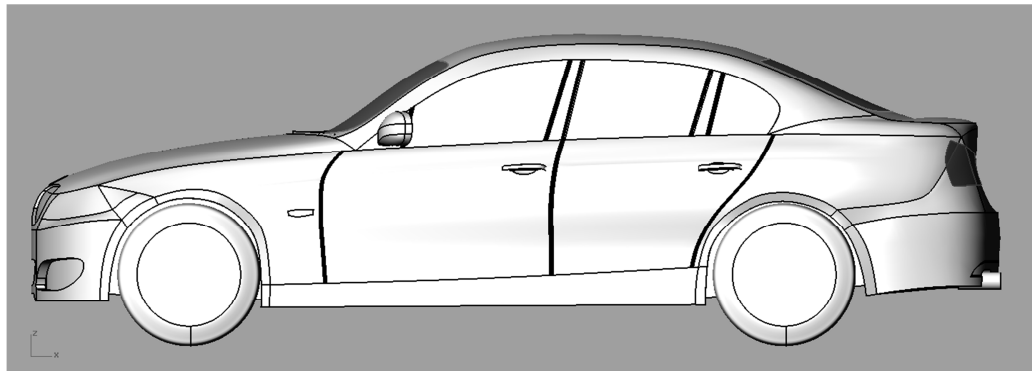


Figure 6.5 CAD model of the car (side view)

6.2 Softwares Used in the Study

The car model was drawn by using Rhinoceros and Catia softwares and saved as “.iges” file. Then it was imported to Gambit software in which the domain was created and surface meshing was done. Volume meshing process was done in Tgrid software. After all of this, a mesh file was imported to Fluent and CFD analyses were done. In Figure 6.6, softwares used in this study and relations between them are presented schematically.

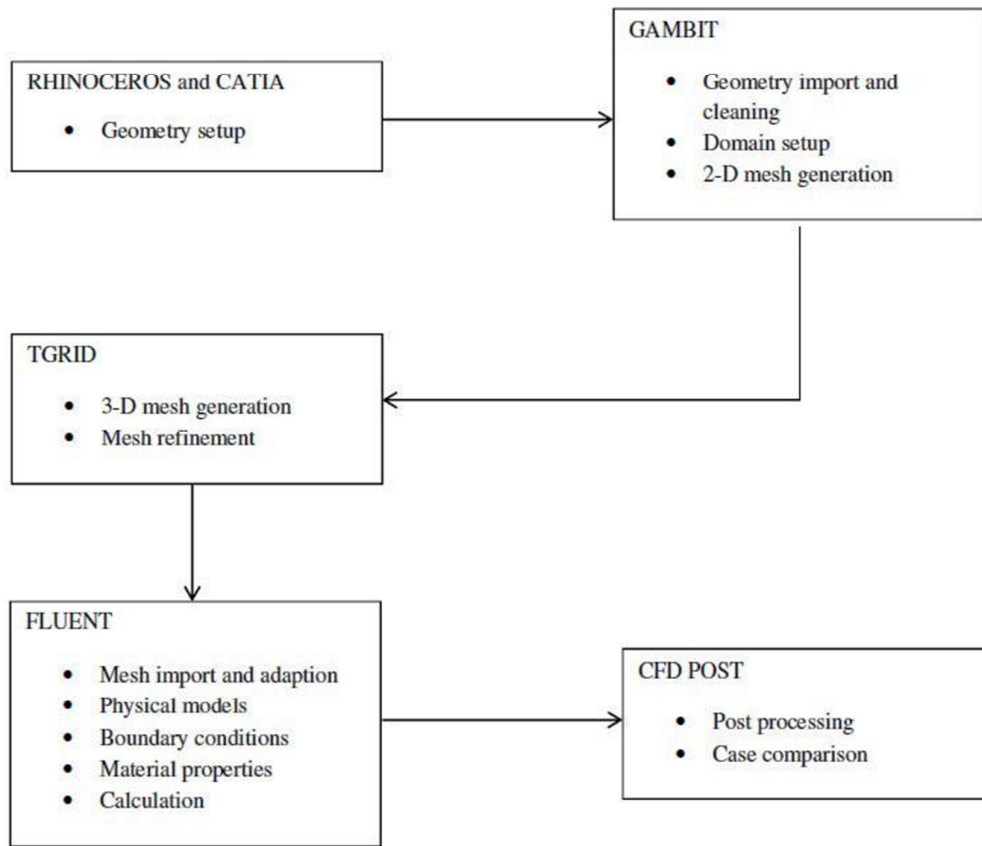


Figure 6.6 Software structure of the study

6.2.1 Rhinoceros

Rhinoceros is a 3-D modeling CAD software especially designed for industrial applications. It is suitable for particularly 3-D prototyping. Allowance of Rhinoceros to various file extensions, accelerates the work flow. It is widely used in industrial, architectural and vehicle design.

6.2.2 Catia

Catia is CAD/CAM/CAE software developed by French Dassault company and marketing by IBM. The pioneer companies in automotive, defence, aviation and shipping are using this software.

6.2.3 Gambit

Gambit is a pre-processor software which is designed for Fluent. Two and three-dimensional structured or unstructured meshing and geometric modeling can be accomplished. The files prepared in other CAD softwares can be imported as “.iges” and “.step” files.

6.2.4 Tgrid

Tgrid is another pre-processor designed for Fluent. In this software volume meshes are generated from the surface meshes imported from Gambit or other third party softwares. It is superior to Gambit in volume meshing because of its efficient memory usage and simplicity.

6.2.5 Fluent

Fluent developed in 1983 is a CFD software using finite volume method. It has become one of the most popular CFD softwares used in various branches of industry.

It can solve problems related to fluid mechanics and heat transfer in the areas of automotive, aviation, air-conditioning, turbomachinery etc.

With its user-friendly interface, it gives the user an opportunity to evaluate the performance of the product and to solve the problems related to it in design stage.

6.3 The Domain

In this study, the wind tunnel tests conducted by Aka [4] were simulated by using CFD software. To reduce the computational efforts (CPU time and memory), the symmetry property of the flow was utilized and the halves of the car and wind tunnel were modeled.

Experiments of Aka [4] had been conducted in open circuit wind tunnel having 0.3m×0.3m cross-section and 0.9m length of test section situated at Aerodynamics Laboratory of Gazi University Faculty of Engineering.

Computational domain for CFD simulations are constituted based on experiments of Aka [4]. The half domain extends are $w \times h \times l = 0.15 \times 0.3 \times 0.9$ meters. The clearances of the model from front and the back of the car were 0.9 and 1.2 times of the model car length respectively. The computational domain is presented in Figure 6.7.

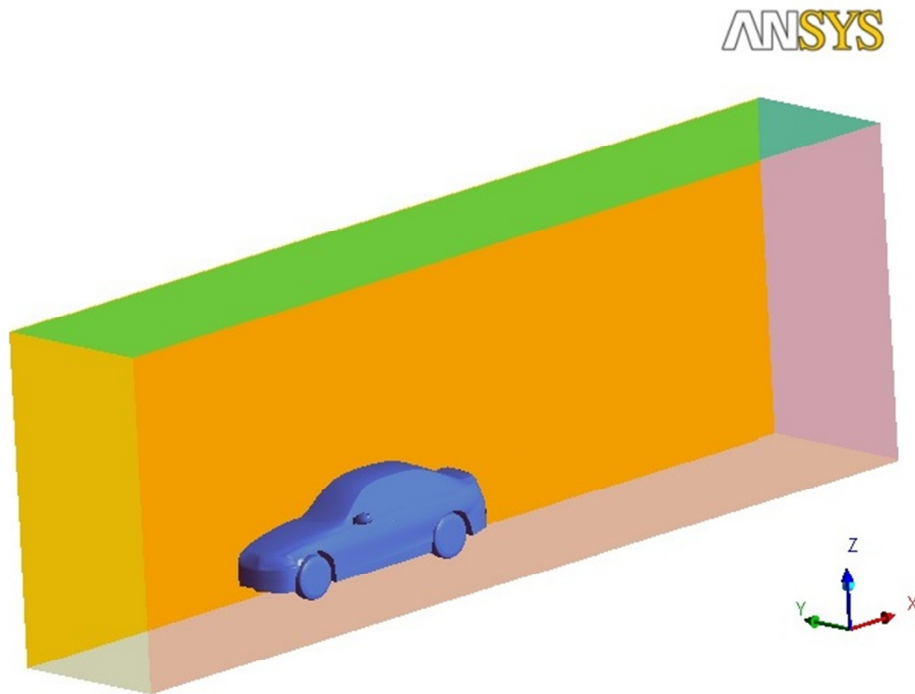


Figure 6.7 Computational domain

Meshing of surfaces was generated in Gambit by using triangular elements. After that, elements were checked in terms of skewness and elements having high skewness (higher than 0.6) were corrected by using the virtual geometry feature of the Gambit, since the elements of high skewness may cause the solution to diverge [14]. Then, boundary types were defined and the surfaces were entitled.

2-D model was imported to Tgrid. To be able to obtain smooth elements near the wall region where the viscosity is effective, prismatic elements were extruded with 20% growth rate from the surface elements. The rest of the domain was filled with tetrahedral 3-D elements which were intensified from far to near the walls of the car. The grid generated according to these processes consisted of approximately 2×10^6 elements for CFD simulations. One of the main aims in the meshing process was obtain a mesh resolution to prevent the wall adjacent cells from being placed in the buffer layer ($y^+ = 5 \sim 30$) in order to use wall functions. By determining proper first cell height, this criterion was satisfied for the mesh used in this study. In Figures 6.8 to 6.10, the grid on different surfaces of domain can be seen.

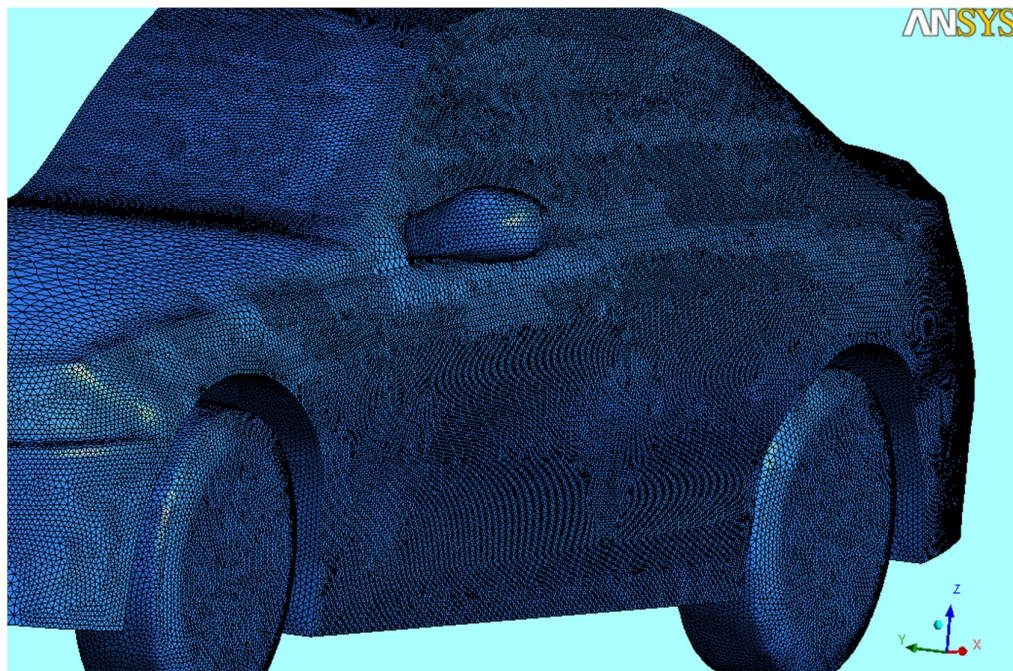


Figure 6.8 The grid on the car surface

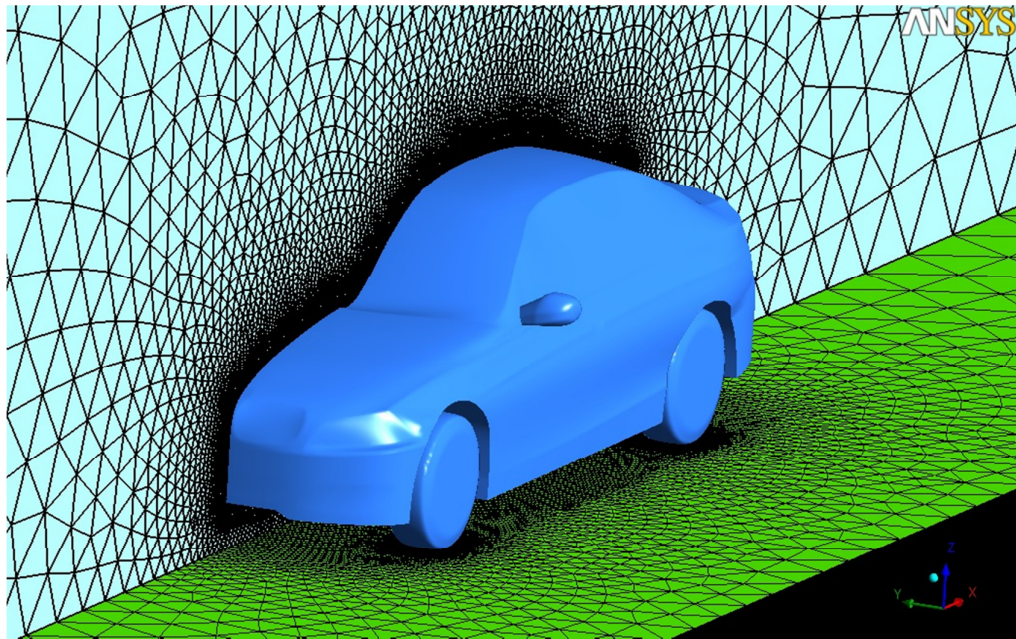


Figure 6.9 The grid on the symmetry plane and ground surface

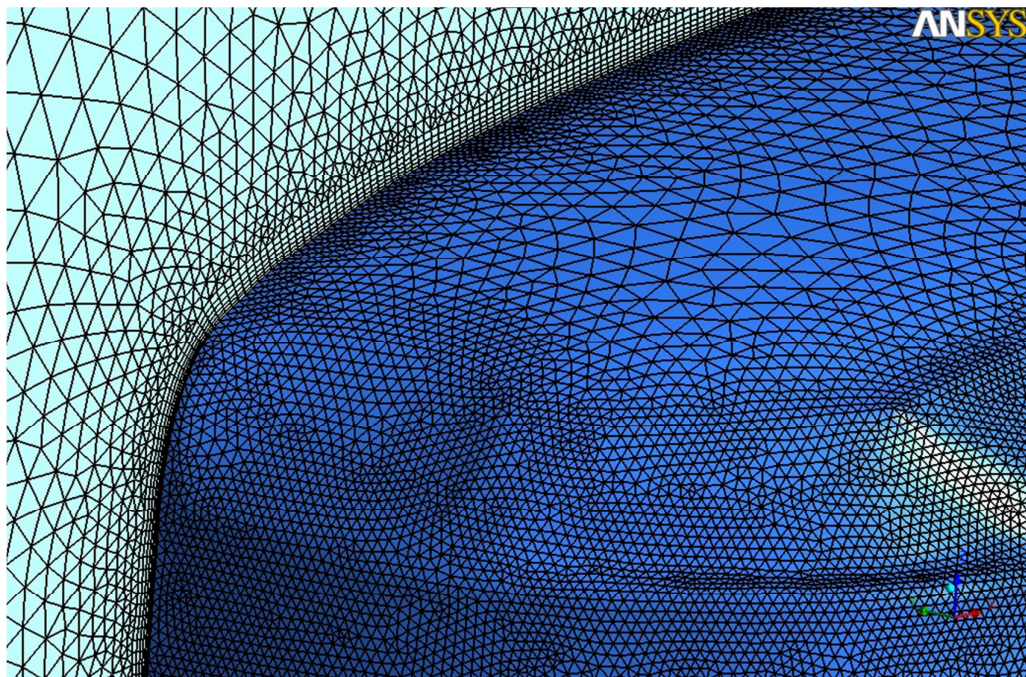


Figure 6.10 Prismatic elements on the symmetry plane

6.4 Boundary Conditions and Settings

The defined boundary conditions of computational domain are shown in Figure 6.11.

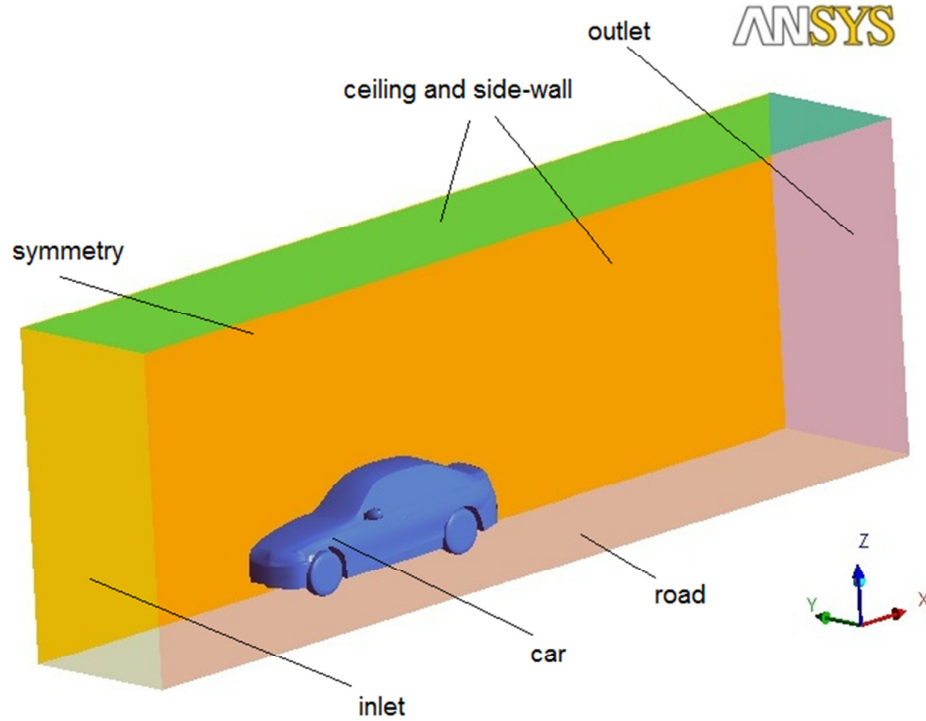


Figure 6.11 Defined boundary conditions

Inlet: Velocity inlet. Magnitude and direction of the velocity and turbulence quantities were defined for this boundary. Fluent offers four options for defining these quantities. “Intensity and hydraulic diameter” is the most appropriate option for the simulations in this study. The hydraulic diameter is calculated from the equation below,

$$D_h = 4 \frac{\text{cross sectional area of duct}}{\text{wetted perimeter of duct}} \quad (6.1)$$

On the other hand, turbulence intensity is usually provided by wind tunnel producers in their manuals or catalogues. Unfortunately, for the wind tunnel that was used in this study, there is no such data available. Nevertheless, an approximate intensity value can be taken. In the literature, turbulence intensity value is taken below 0.5%

for similar wind tunnels. For modern wind tunnels, this value may even drop 0.1%. In the simulations of this study, turbulence intensity was selected as 0.2% depending the past studies and similar wind tunnel data.

Outlet: Pressure outlet. Pressure value at the outlet and turbulence parameters were defined for this boundary. As outlet condition, pressure measurements of Aka [4] were used.

Ceiling, side-wall and road: No-slip walls

Car: No-slip wall. Viscosity is effective and air stick at the car coachwork.

Symmetry plane: At that plane the symmetry boundary condition was used.

The values for these boundary conditions are summarized in Table 6.2.

Table 6.1 Settings for the boundary conditions

Test Section ($w \times h \times l$) m	0.15×0.3×0.9
Velocity (m/s)	5, 9, 13, 17, 21, 25
ρ (kg/m ³)	1.222 @10 ⁰ C
μ (kg/ms)	1.789×10 ⁻⁵ @10 ⁰ C
Hydraulic diameter (m)	0.2
Turbulence intensity (%)	0.2
Outlet pressure (Pa)	-12, -41, -81, -130, -214, -288
Frontal area (m ²)	4.838×10 ⁻³

In this study, calculations were performed on a PC which has Intel Core i5-760 processor and 4 GB DDR3 RAM hardware.

In the analyses; to test the reliability and performance of turbulence models, Spalart-Allmaras, standard $k-\epsilon$, RNG $k-\epsilon$, realizable $k-\epsilon$, standard $k-\omega$, SST $k-\omega$ and Reynolds stress turbulence models were investigated. These are most widely used models due

to their lower computational cost and reasonable accuracy in industry and for that reason they are selected in the scope of this thesis.

High Reynolds number turbulence models need wall functions for solution. In Fluent there are two wall functions namely; standard wall function and non-equilibrium wall function. Fluent recommends [48] non-equilibrium wall function for external aerodynamic simulations. Besides, past studies [3] and preliminary studies have shown that, non-equilibrium wall function predicts the turbulent boundary layer behaviour more accurate than standard wall function and especially it is preferred for external flows with pressure gradients and separation. Therefore, in this study non-equilibrium wall function was used with $k-\varepsilon$ (standard, RNG and realizable) and RSM turbulence models. $k-\omega$ (standard, SST) and Spalart-Allmaras are low Reynolds number turbulence models so there is no need to use wall functions with that turbulence models.

Convergence criterion for residuals of flow and other flow equations was chosen as 10^{-5} . All the simulations are performed until the solution is converged.

As explained in Chapter 4, Green-Gauss node-based gradient option is turned on. Because Green-Gauss node-based is preferred over Green-Gauss cell-based since it performs better for unstructured meshes like the one that used in this study.

Since the numerical discretization errors (numerical diffusion) are larger for first order scheme [48], second order discretization was used for pressure, momentum and turbulence quantities. It is also suggested in the literature that, one can get more accurate results with triangular or tetrahedral grids by applying second order discretization scheme [15]. These suggestions on first order scheme were also verified in the preliminary studies.

Properties of air at the conditions that experiments were conducted were used in simulations.

Relaxation factors are presented in Table 6.2.

Table 6.2 Relaxation factors

Pressure	0.3
Density	1
Body forces	1
Momentum	0.7
Turbulent kinetic energy	0.8
Turbulent dissipation rate	0.8
Turbulent viscosity	1

6.5 Results and Discussion

In this section, the results of CFD simulations which were made by using various turbulence models will be presented. Results will be investigated in terms of drag coefficient, pressure and velocity distributions, computational efforts and general flow pattern around the car.

Drag forces and drag coefficients for different velocities are presented in Tables 6.3 to 6.8 for various turbulence models.

Table 6.3 C_D values for $V=5$ m/s ($Re=95472$)

Turbulence Model	$(F_D)_p$ (N)	$(F_D)_f$ (N)	$(F_D)_t$ (N)	C_D	Error (%)
Realizable $k-\varepsilon$	0.021	0.010	0.031	0.420	30.4
RNG $k-\varepsilon$	0.025	0.006	0.031	0.420	30.4
Reynolds Stress	0.026	0.004	0.030	0.407	26.4
SST $k-\omega$	0.021	0.005	0.026	0.352	9.3
Standard $k-\varepsilon$	0.025	0.007	0.032	0.434	34.8
Standard $k-\omega$	0.023	0.005	0.028	0.380	18
Spalart-Allmaras	0.022	0.009	0.031	0.420	30.4
Experiment [4]	-	-	-	0.322	-

Table 6.4 C_D values for $V=9$ m/s ($Re=171850$)

Turbulence Model	$(F_D)_p$ (N)	$(F_D)_f$ (N)	$(F_D)_t$ (N)	C_D	Error (%)
Realizable $k-\varepsilon$	0.074	0.014	0.088	0.368	4.2
RNG $k-\varepsilon$	0.064	0.026	0.090	0.376	6.5
Reynolds Stress	0.074	0.014	0.088	0.368	4.2
SST $k-\omega$	0.068	0.013	0.081	0.339	-4
Standard $k-\varepsilon$	0.065	0.028	0.093	0.389	10.2
Standard $k-\omega$	0.073	0.015	0.088	0.368	4.2
Spalart-Allmaras	0.081	0.015	0.096	0.402	13.9
Experiment [4]	-	-	-	0.353	-

Table 6.5 C_D values for $V=13$ m/s ($Re=248228$)

Turbulence Model	$(F_D)_p$ (N)	$(F_D)_f$ (N)	$(F_D)_t$ (N)	C_D	Error (%)
Realizable $k-\varepsilon$	0.138	0.037	0.175	0.351	-3.3
RNG $k-\varepsilon$	0.134	0.044	0.178	0.357	-1.7
Reynolds Stress	0.137	0.036	0.173	0.347	-4.4
SST $k-\omega$	0.134	0.033	0.167	0.335	-7.7
Standard $k-\varepsilon$	0.136	0.047	0.183	0.367	1.1
Standard $k-\omega$	0.142	0.039	0.181	0.363	0
Spalart-Allmaras	0.149	0.043	0.192	0.385	6.1
Experiment [4]	-	-	-	0.363	-

Table 6.6 C_D values for $V=17$ m/s ($Re=324606$)

Turbulence Model	$(F_D)_p$ (N)	$(F_D)_f$ (N)	$(F_D)_t$ (N)	C_D	Error (%)
Realizable $k-\varepsilon$	0.242	0.046	0.288	0.338	-4.8
RNG $k-\varepsilon$	0.235	0.061	0.296	0.347	-2.3
Reynolds Stress	0.236	0.051	0.287	0.337	-5.1
SST $k-\omega$	0.242	0.041	0.283	0.332	-6.5
Standard $k-\varepsilon$	0.244	0.054	0.298	0.349	-1.7
Standard $k-\omega$	0.246	0.062	0.308	0.361	1.7
Spalart-Allmaras	0.257	0.064	0.322	0.378	6.5
Experiment [4]	-	-	-	0.355	-

Table 6.7 C_D values for $V=21$ m/s ($Re=400984$)

Turbulence Model	$(F_D)_p$ (N)	$(F_D)_f$ (N)	$(F_D)_t$ (N)	C_D	Error (%)
Realizable $k-\varepsilon$	0.354	0.076	0.430	0.330	-7.6
RNG $k-\varepsilon$	0.366	0.075	0.441	0.339	-5
Reynolds Stress	0.383	0.066	0.449	0.345	-3.4
SST $k-\omega$	0.371	0.056	0.427	0.328	-8.1
Standard $k-\varepsilon$	0.360	0.083	0.443	0.340	-4.8
Standard $k-\omega$	0.384	0.079	0.463	0.356	-0.3
Spalart-Allmaras	0.393	0.088	0.481	0.370	3.6
Experiment [4]	-	-	-	0.357	-

Table 6.8 C_D values for $V=25$ m/s ($Re=477362$)

Turbulence Model	$(F_D)_p$ (N)	$(F_D)_f$ (N)	$(F_D)_t$ (N)	C_D	Error (%)
Realizable $k-\varepsilon$	0.505	0.095	0.600	0.325	-8.5
RNG $k-\varepsilon$	0.544	0.072	0.616	0.334	-5.9
Reynolds Stress	0.548	0.084	0.632	0.343	-3.4
SST $k-\omega$	0.532	0.074	0.606	0.329	-7.3
Standard $k-\varepsilon$	0.541	0.053	0.594	0.322	-9.3
Standard $k-\omega$	0.576	0.089	0.665	0.361	1.7
Spalart-Allmaras	0.531	0.106	0.637	0.345	-2.8
Experiment [4]	-	-	-	0.355	-

As seen in Tables 6.3 to 6.8, the decisive component of drag force is form drag. According to drag results it can be said that, approximately 85% of total drag comprised from drag and only 15% of it from the viscous drag. This results support the previous studies [5].

The variation of drag coefficients with Reynolds number for various turbulence models are presented in Figure 6.12.

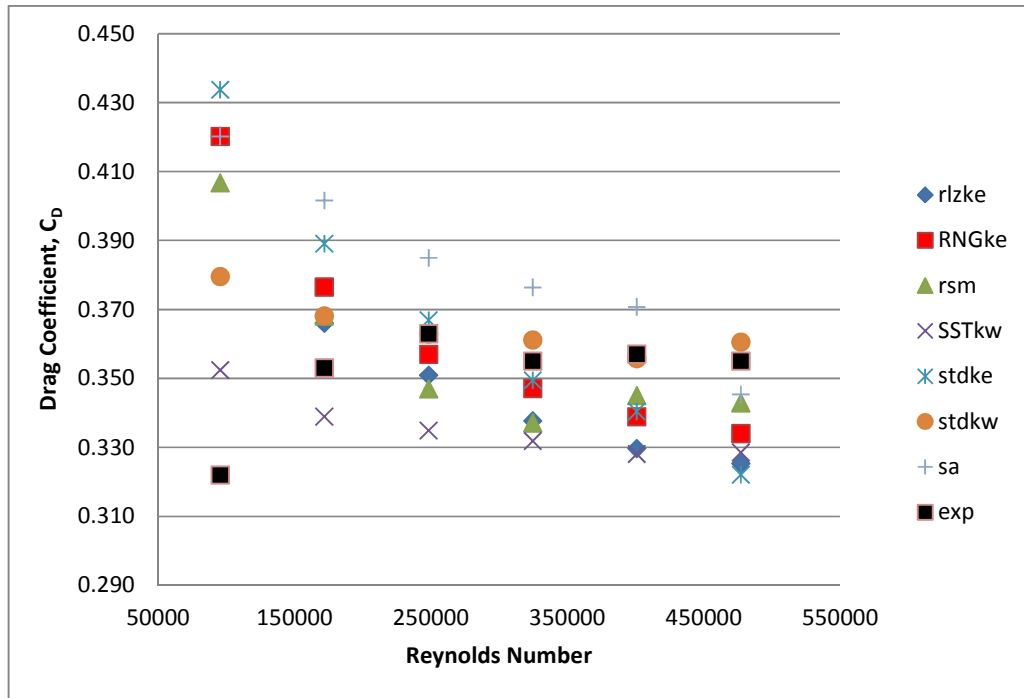


Figure 6.12 Variation of drag coefficient with Reynolds number

Generally, the results obtained at low speeds contain more errors than the results obtained at high speeds. Especially in the analyses made with 5m/s velocity ($Re=95472$), C_D was overestimated by the turbulence models. One of the reasons of it may be the unreliability of wall function approach at low Reynolds numbers. This comment is supported by the fact that $k-\omega$ turbulence models which are low Reynolds number models and do not need any wall functions, gave more accurate results at that speed. In order to obtain more accurate results with high Reynolds number turbulence models ($k-\epsilon$ models and RSM), enhanced wall treatment option of Fluent may be used. But this requires very fine mesh near the wall and hence more computational effort. Furthermore in the experiments of Aka [4] there was a fluctuation at C_D for 5m/s velocity. The reason of it was the uncertainty in the force drag force and the freestream velocity. For instance, let us consider two force and velocity measurements taken at 5 m/s and 25 m/s. There were 0.04 N and 0.1 m/s difference between two successive force and velocity measurements respectively;

a) Velocity: 5m/s		b) Velocity: 25m/s	
$V_1=5$ m/s	$V_2=5.1$ m/s	$V_1=25$ m/s	$V_2=25.1$ m/s
$F_{D1}= 0.03$ N	$F_{D2}=0.07$ N	$F_{D1}=1.26$ N	$F_{D2} =1.30$ N
$\rho=1.22$ kg/m ³		$\rho=1.22$ kg/m ³	
$A=0.0095$ m ²		$A=0.0095$ m ²	
$C_{D1}=0.21$	$C_{D2} =0.46$	$C_{D1}=0.35$	$C_{D2} =0.36$

As it is seen the difference between two C_D measurements is 0.25 for 5 m/s while it is 0.01 for 25 m/s. This situation explains the variability of C_D values in experiments obtained at low speeds.

In low speed CFD simulations, most accurate C_D value were obtained with SST $k-\omega$ turbulence model. For instance, C_D was calculated as 0.352 with SST $k-\omega$ which is 9.4% higher than experimental value 0.322 for 5 m/s velocity.

As the velocity increases, drag coefficients calculated with different turbulence models become more accurate. The best results were obtained with standard $k-\omega$, for which error was under 2% at the velocities 21 m/s and 25 m/s.

In order to determine the pressure distribution on the car, pressure coefficients were calculated for $V=25$ m/s at different ports on the symmetry plane of the car shown in Figure 6.13 with different turbulence models. At that pressure ports there are experimental pressure coefficient values available from Aka's wind tunnel tests [4].

CFD simulation and wind tunnel test C_p results at pressure ports are presented in Tables 6.9 and 6.10.

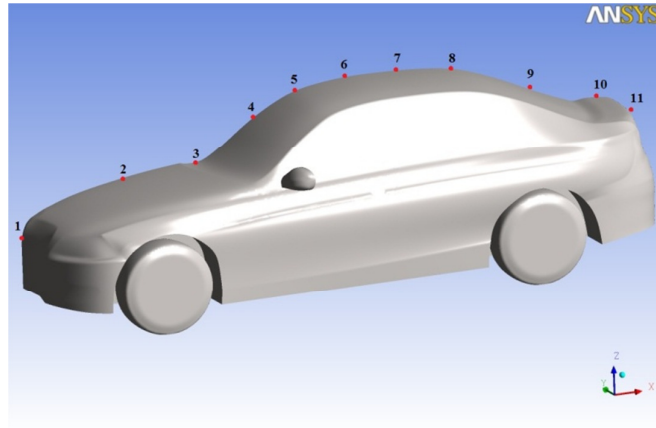


Figure 6.13 Pressure port locations on the symmetry plane of the car

Table 6.9 C_p values obtained with various turbulence models (ports 1-5)

Turbulence Model	Port 1	Port 2	Port 3	Port 4	Port 5
Realizable $k-\varepsilon$	0.01	-0.93	-0.42	-0.71	-1.27
RNG $k-\varepsilon$	0.01	-0.92	-0.37	-0.87	-1.41
Reynolds Stress	0.01	-0.89	-0.40	-0.77	-1.44
SST $k-\omega$	0.02	-0.91	-0.46	-0.85	-1.36
Standard $k-\varepsilon$	0.01	-0.92	-0.40	-0.78	-1.36
Standard $k-\omega$	0.02	-0.92	-0.46	-0.84	-1.35
Spalart-Allmaras	0.01	-0.91	-0.45	-0.68	-1.43
Experiment [4]	0.02	-0.94	-0.46	-0.84	-1.44

Table 6.10 C_p values obtained with various turbulence models (ports 6-11)

Turbulence Model	Port 6	Port 7	Port 8	Port 9	Port 10	Port 11
Realizable $k-\varepsilon$	-1.45	-1.34	-1.36	-0.97	-0.89	-0.88
RNG $k-\varepsilon$	-1.29	-1.37	-1.36	-0.92	-0.91	-0.95
Reynolds Stress	-1.46	-1.31	-1.39	-0.92	-0.86	-0.88
SST $k-\omega$	-1.40	-1.31	-1.35	-1.01	-0.86	-0.87
Standard $k-\varepsilon$	-1.48	-1.36	-1.34	-1.03	-0.84	-0.93
Standard $k-\omega$	-1.32	-1.38	-1.36	-1.09	-0.90	-0.95
Spalart-Allmaras	-1.41	-1.38	-1.35	-0.81	-0.92	-0.71
Experiment [4]	-0.89	-1.53	-1.37	-1.11	-0.92	-1.17

Variation of C_p with pressure ports can be seen in Figure 6.14.

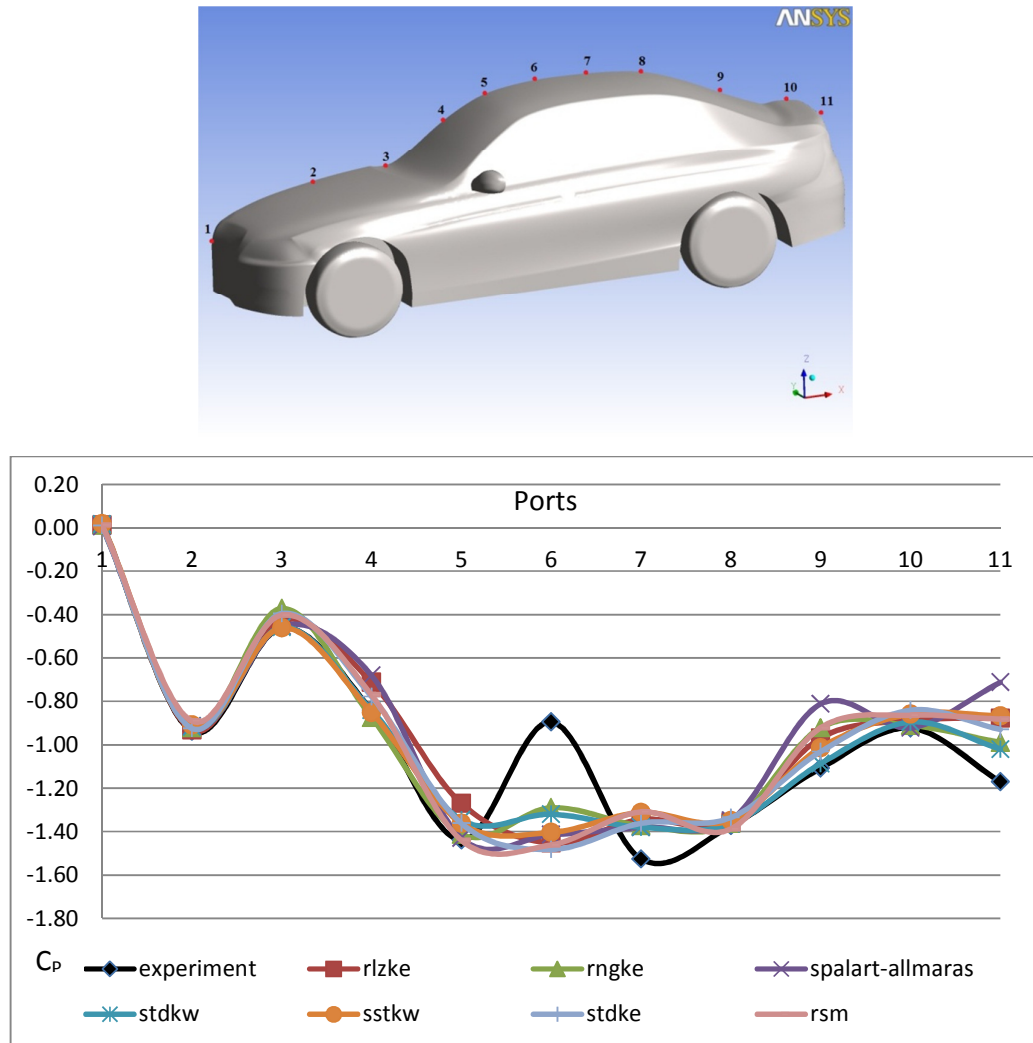


Figure 6.14 Variation of C_p with pressure ports

As it is seen in Figure 6.14, general trend of C_p is predicted accurately by using turbulence models except for ports 6, 7 and 11.

All turbulence models were not able to capture the pressure peak at port 6 which is at the beginning of the ceiling. In this region flow slows down suddenly and then accelerates again until reaches port 7. At these ports RNG $k-\epsilon$ model gives relatively good results compared to other turbulence models. In experiments an adverse pressure gradient observed in that region which might cause separation at the

beginning of the ceiling. However in CFD analyses the pressure in that region calculated is almost constant and no separation was observed.

Port 11 is at the back of the car and located after separation point. Calculated pressure values are bigger than the experimental ones about 20%. At this port relatively good results were obtained with RNG $k-\varepsilon$ and standard $k-\omega$ models.

Maximum pressure was calculated at port 1 which is near the bottom of the front grills. On the other hand minimum pressure was calculated at port 6. At that region flow accelerates and pressure decreases. However, minimum pressure was obtained at port 7 which is at the middle of the ceiling in the wind tunnel tests. All turbulence models overpredicted the pressure value at this port.

According to C_p values obtained at all ports; it can be said that, RNG $k-\varepsilon$ model gives more accurate results compared to other turbulence models.

In Figures 6.15 and 6.16, pressure coefficient contours on the car obtained with RNG $k-\varepsilon$ model is presented.

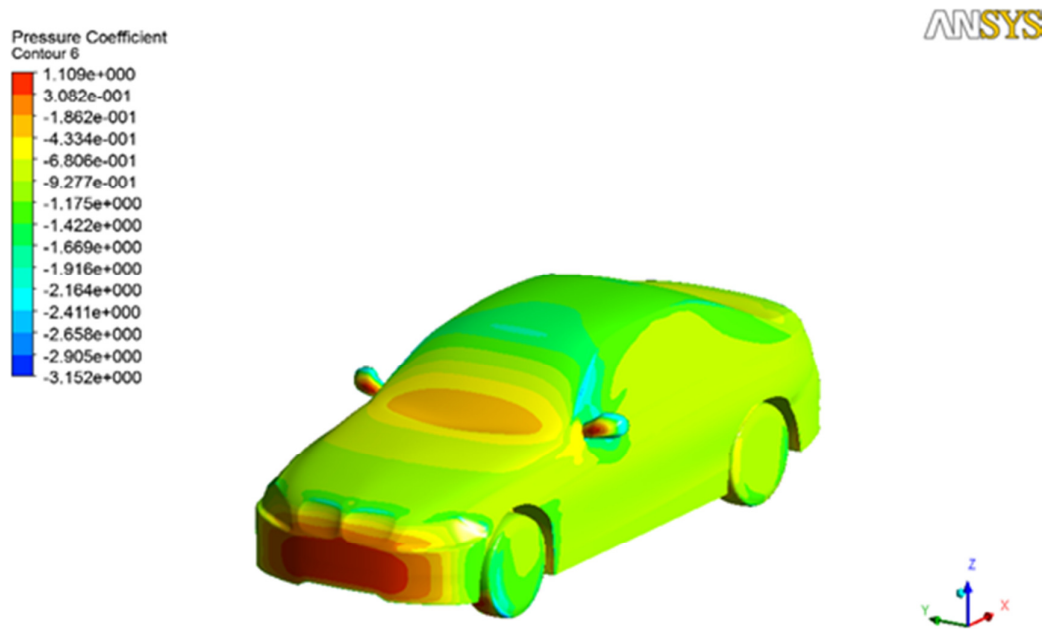


Figure 6.15 Pressure coefficient contours on the coachwork of a car, front perspective view (RNG $k-\varepsilon$ model)

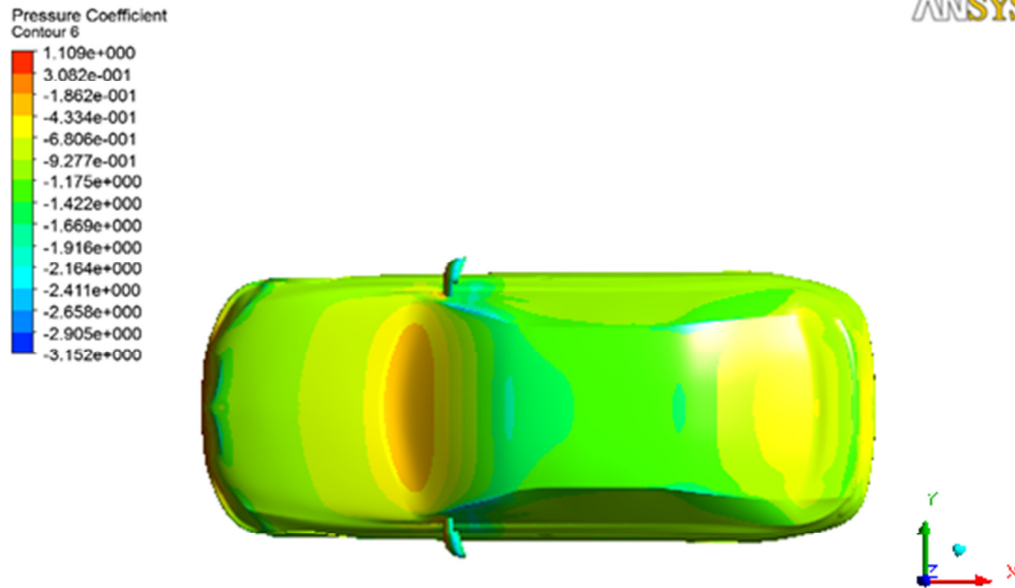


Figure 6.16 Pressure coefficient contours on the coachwork of a car, top view
(RNG $k-\varepsilon$ model)

High pressures were obtained at the front bumper, side mirrors and lower part of the front wheels in Figure 6.15 and 6.16. It can be said that; flow accelerates from the front bumper to the edge of the hood, then decelerates along the hood, then accelerates again from the windshield to top of the car, then remains almost at constant velocity along the top of the car and then decelerates again from the rear window to the end of the hood. Velocity distribution on the symmetry plane of the car can be seen in Figure 6.17.



Figure 6.17 Velocity distribution on the symmetry plane of the car (RNG $k-\varepsilon$ model)

In this part, how the turbulence models interpret the flow around the car is investigated by presenting 2-D and 3-D streamlines and velocity vectors at different locations on the flow domain. In Figures 6.18 to 6.24, streamlines predicted by the different turbulence models at 25 m/s velocity are shown.

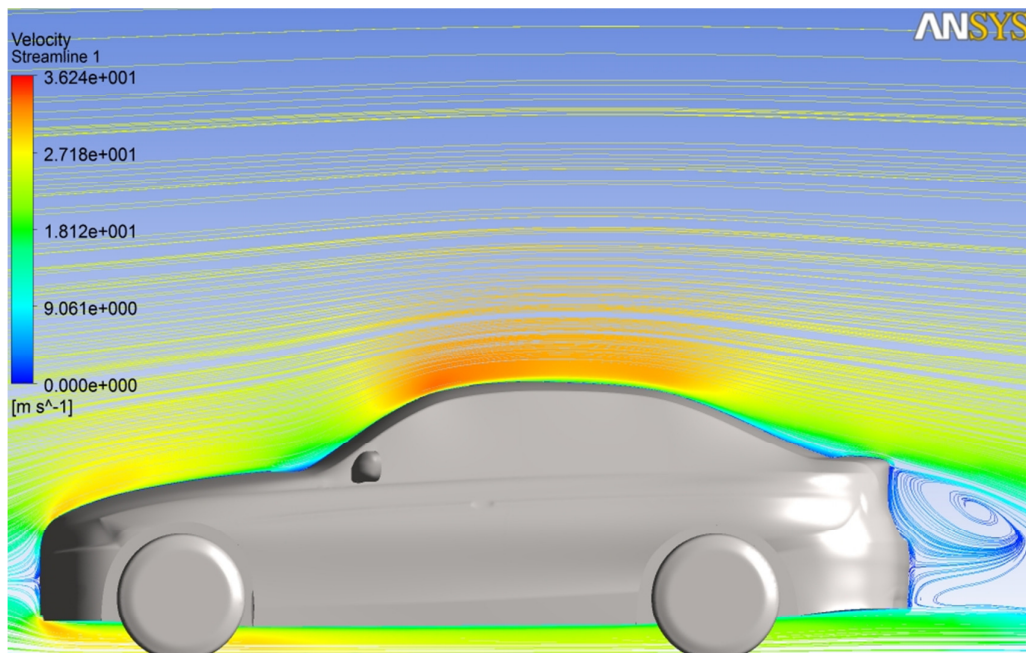


Figure 6.18 Streamlines at the symmetry plane (Realizable $k-\varepsilon$ model)

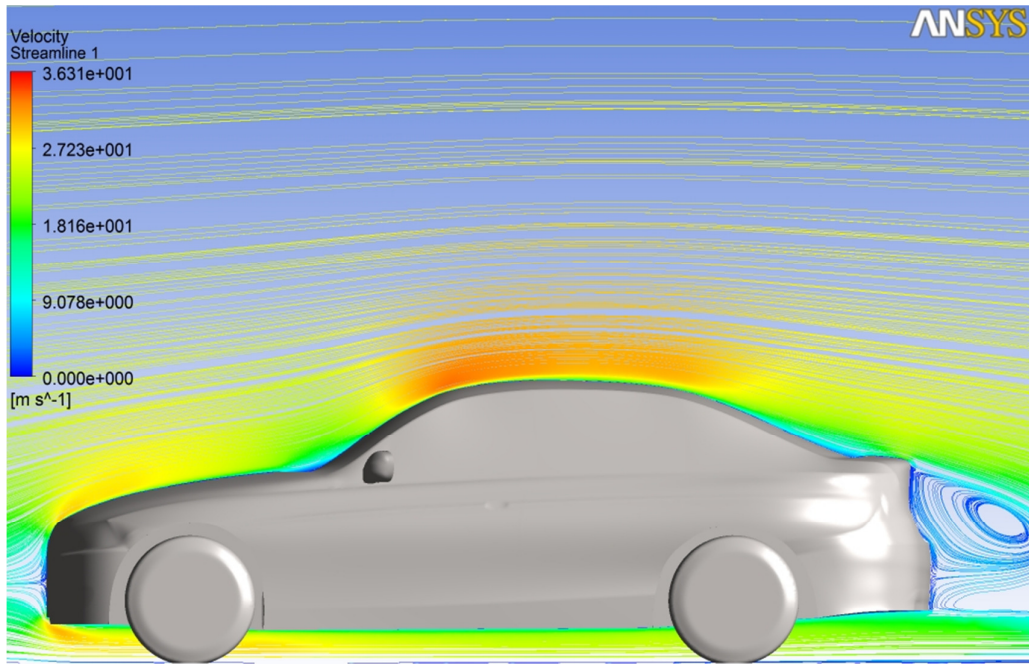


Figure 6.19 Streamlines at the symmetry plane (RNG $k-\varepsilon$ model)

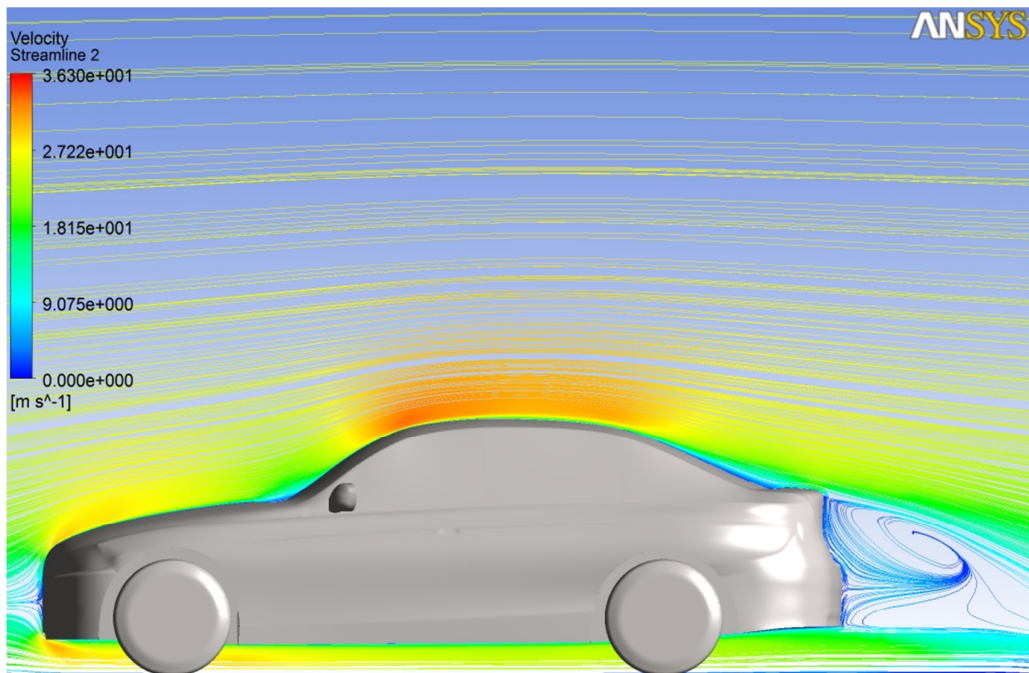


Figure 6.20 Streamlines at the symmetry plane (Reynolds stress model)

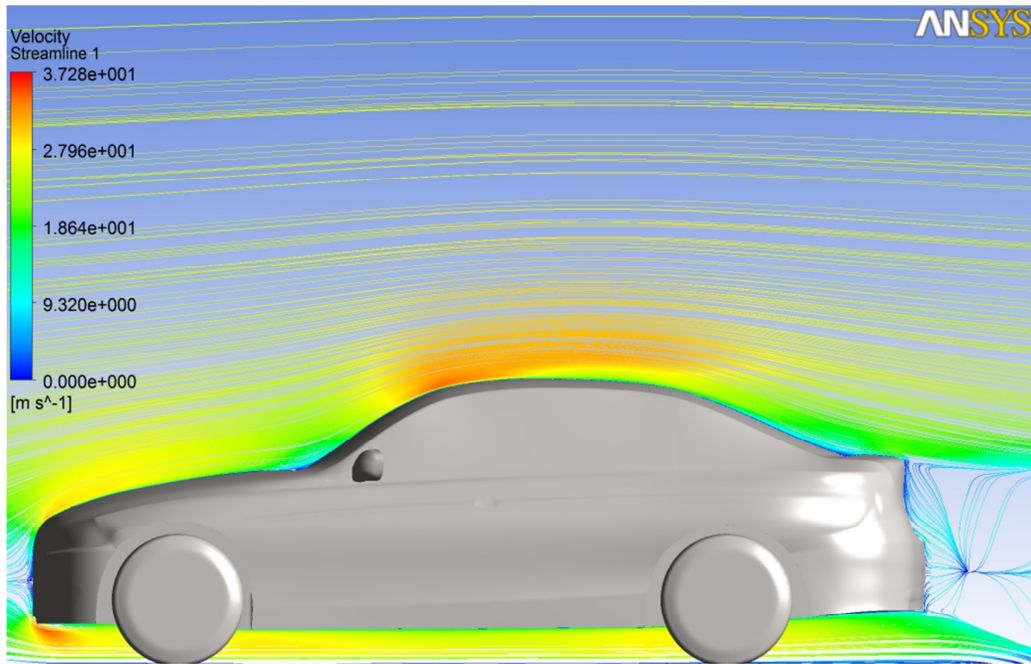


Figure 6.21 Streamlines at the symmetry plane (Spalart-Allmaras model)

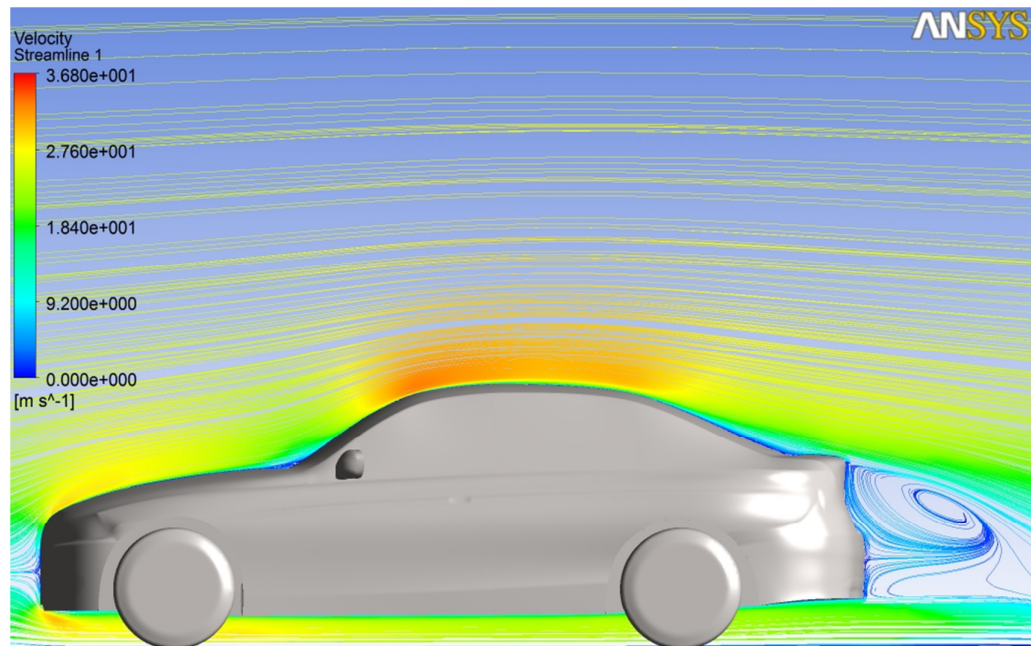


Figure 6.22 Streamlines at the symmetry plane (SST $k-\omega$ model)

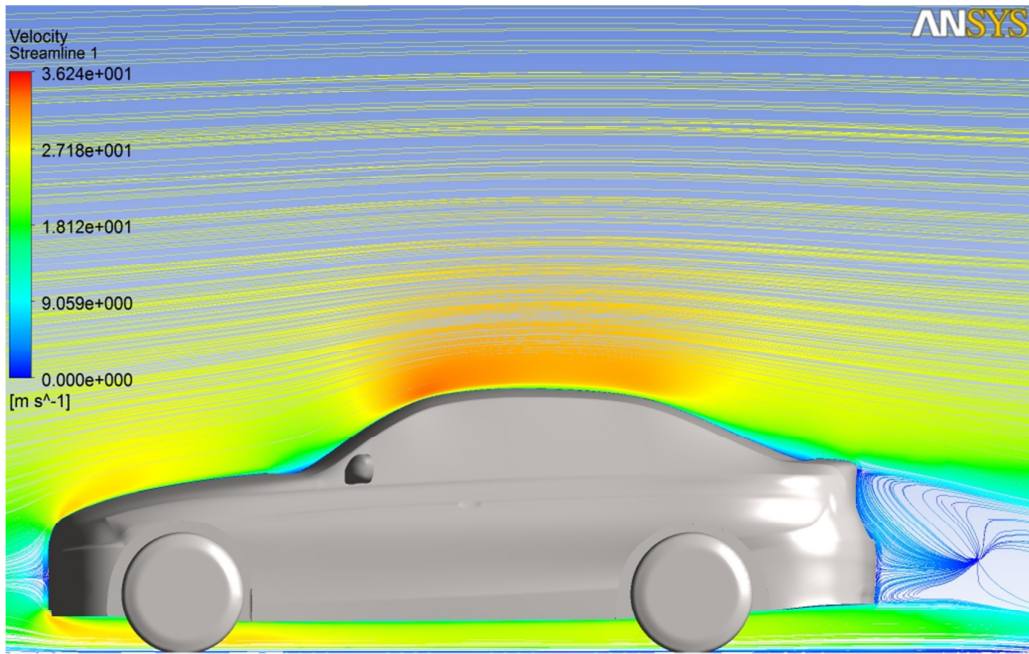


Figure 6.23 Streamlines at the symmetry plane (Standard $k-\varepsilon$ model)

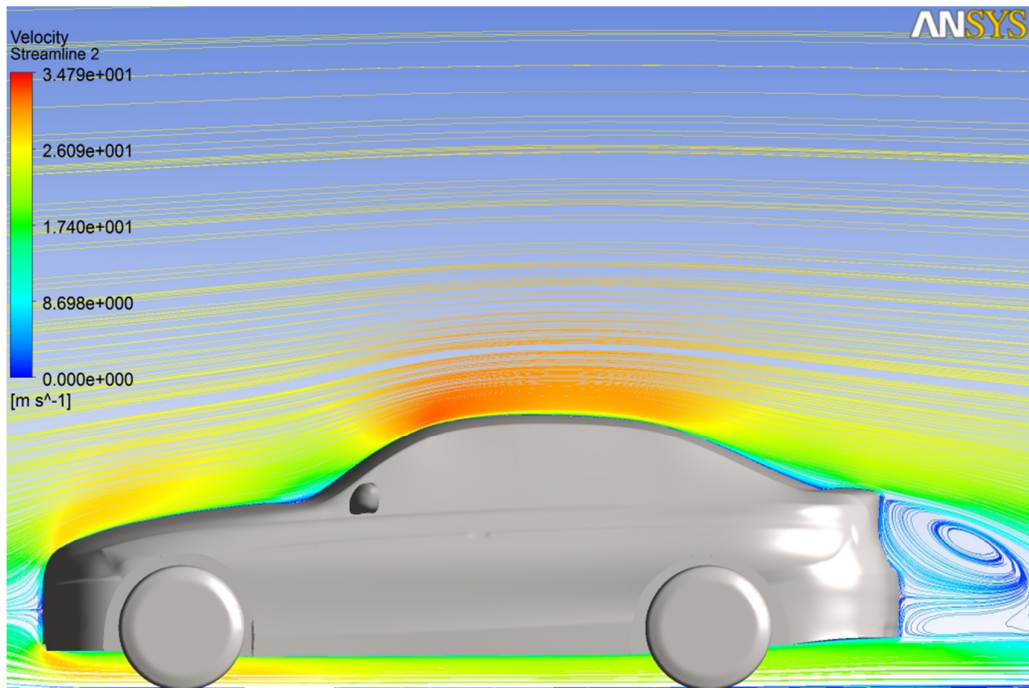


Figure 6.24 Streamlines at the symmetry plane (Standard $k-\omega$ model)

Following comments can be made according to Figures 6.18 to 6.24. Uniform flow approaching to the car strikes at front bumper under the headlights and it creates a stagnation point then divides into two parts, one is flowing above the hood and the other part is flowing under the car. At the beginning, air passing under the car separates from the surface then reattaches and from this point forward flows at almost constant speed. On the other hand, air flowing above the hood loses its speed first and little standing vortex is formed at the beginning of the windshield according to some turbulence models. In standard $k-\omega$, SST $k-\omega$ and RSM models this vortex is observed while it is not for other models. After this point flow accelerates along the windshield and reaches its maximum speed at the region where windshield and ceiling intersect. In all turbulence models it is not observed any separation and vortex formation at this region. Air flows along the ceiling almost at constant speed and decelerates on the rear window. At 25 m/s velocity, all turbulence models predict attached flow over the rear window. On the other hand at lower velocities such as 5 m/s, standard $k-\omega$ and RSM predicts a separation on the rear window (Figure 6.27). At the downstream edge of the trunk flow separates from the surface and creates a turbulent wake region behind the car. This wake region is one of the basic study areas of the automobile aerodynamics. Although there is no experimental data to verify this wake region, it can be said that all turbulence models predicts realistic flow patterns except for standard $k-\varepsilon$ and Spalart-Allmaras models. Other models detect a vortex having a node point at the upperside of rear bumper. RNG $k-\varepsilon$ and standard $k-\omega$ models predict this vortex stronger and also recirculation region larger. Also in Figure 6.25 and 6.26 the surface streamlines and velocity vectors obtained at parallel to xz -plane ($y = -0.019\text{ m}$) can be seen. Two counter-rotating horseshoe vortices computed by RNG $k-\varepsilon$ and standard $k-\omega$ are very realistic flow patterns for this type of cars.

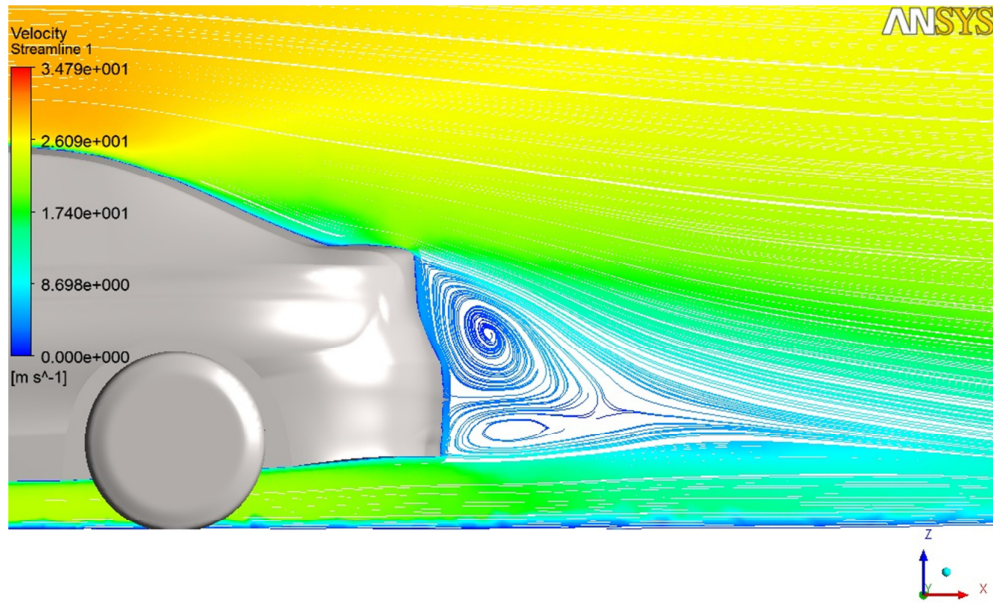


Figure 6.25 Vortices at the wake obtained with RNG $k-\epsilon$ (streamlines)

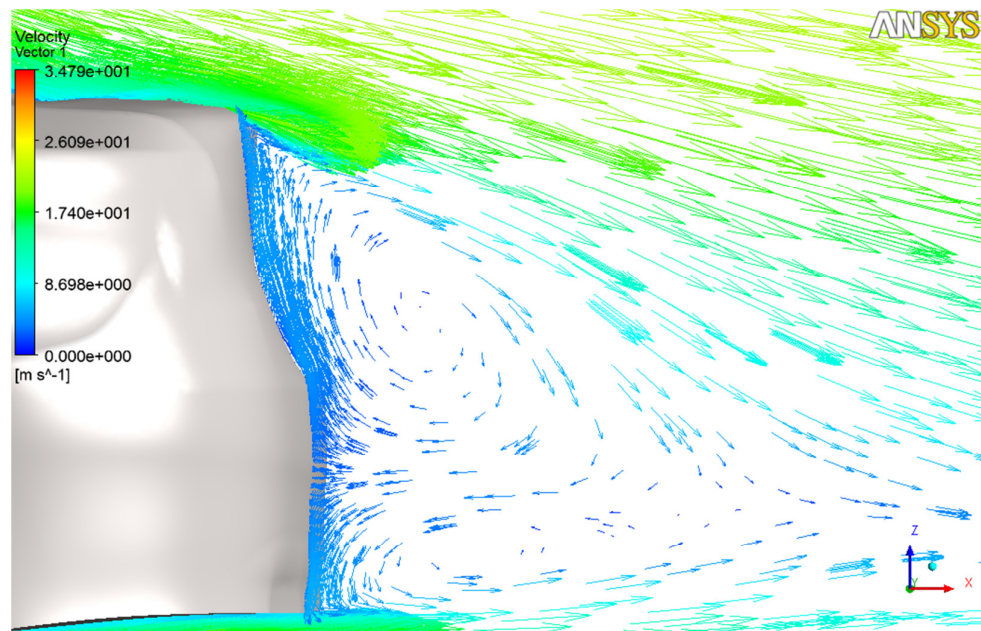


Figure 6.26 Vortices at the wake obtained with RNG $k-\epsilon$ (velocity vectors)

In Figure 6.27, separated flow predicted by SST $k-\omega$ model at 5m/s velocity on the rear window is presented. Separated flow reattaches to the car surface on the trunk.

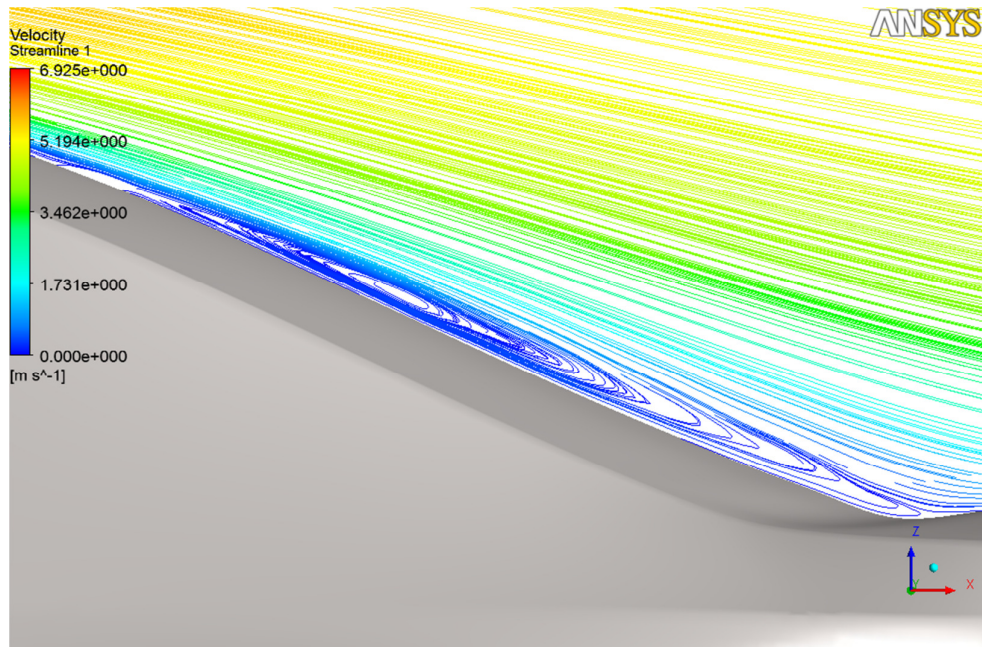


Figure 6.27 Separated flow on the rear window predicted by SST $k-\omega$ ($V=5\text{ m/s}$)

In Figure 6.28, a local standing vortex formed under the car can be seen. Although there are small differences in strengths, this vortex observed with all turbulence models.

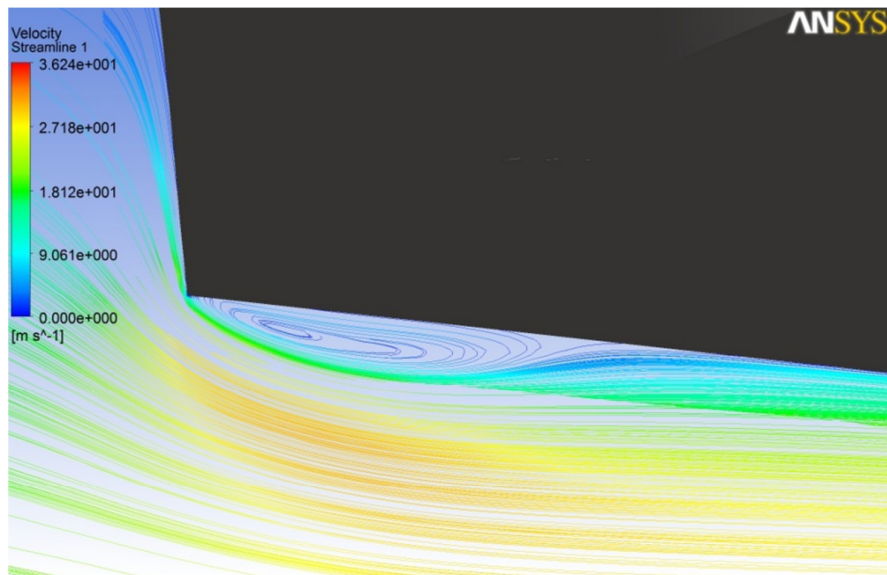


Figure 6.28 Standing vortex under the car (Realizable $k-\epsilon$ model)

Streamlines at the region between windshield and hood are shown in Figures 6.29 and 6.30. As it is seen, in standard $k-\varepsilon$ there is no separation and vortex formation observed while standard $k-\omega$ model detects a separation at this region.

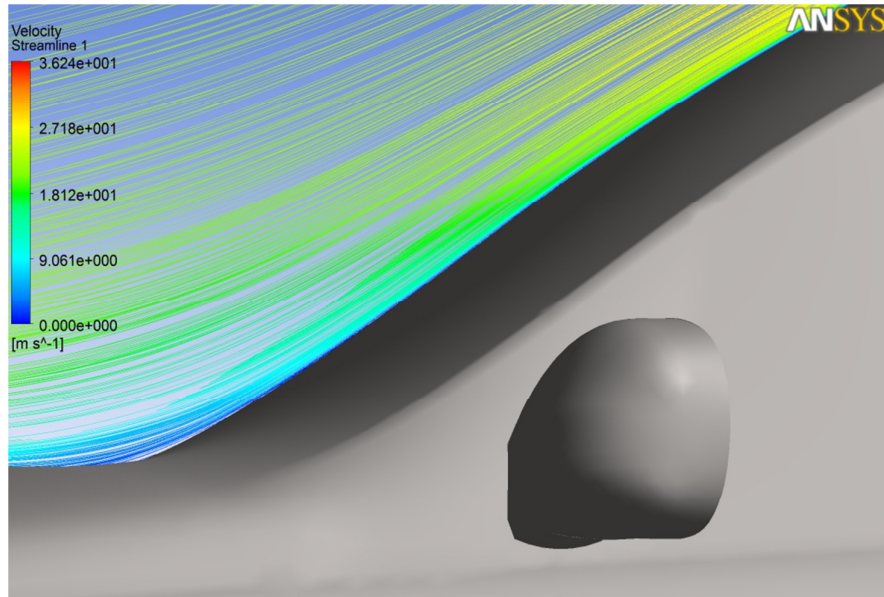


Figure 6.29 Streamlines on the windshield predicted by standard $k-\varepsilon$

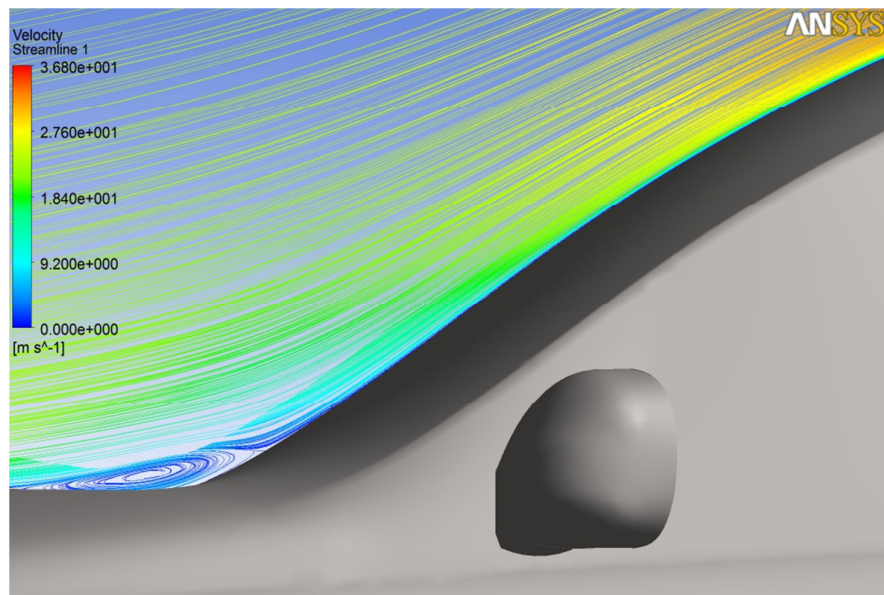


Figure 6.30 Streamlines on the windshield predicted by standard $k-\omega$

Another contributor of drag force is side mirror. The wake region formed behind the side mirror obtained with SST $k-\omega$ and Spalart-Allmaras models is presented in

Figures 6.31 and 6.32 respectively. All turbulence models predicted a vortex with different strengths and node points behind side mirror. Separated flow at that region reattaches car surface afterwards.

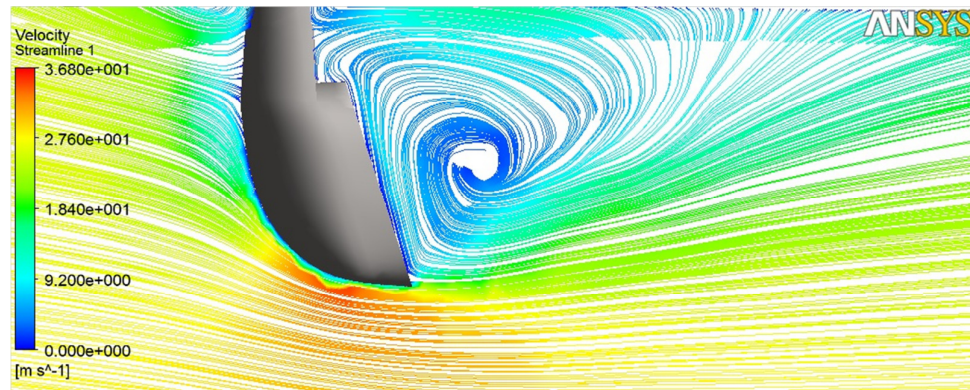


Figure 6.31 Wake region formed behind the side mirror (SST $k-\omega$)

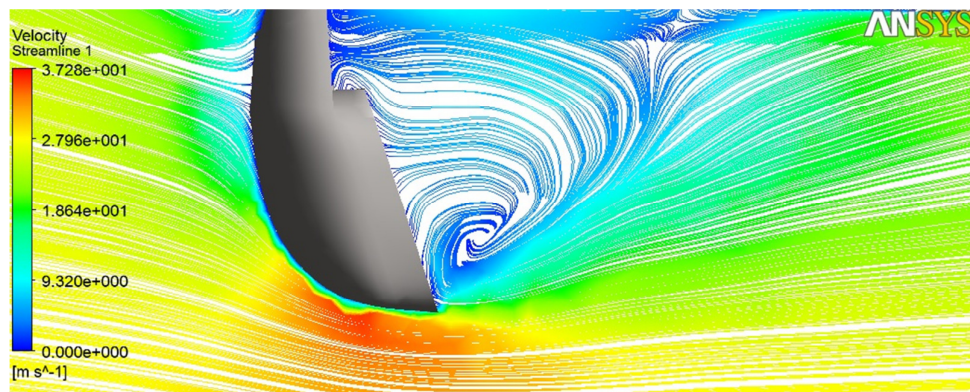


Figure 6.32 Wake region formed behind the side mirror (Spalart-Allmaras)

The turbulent wake flow (Figures 6.18 to 6.24) formed behind the car can be understood better with investigating this region by three-dimensional streamlines. Predicted streamlines at that region are presented in Figures 6.33 to 6.39.

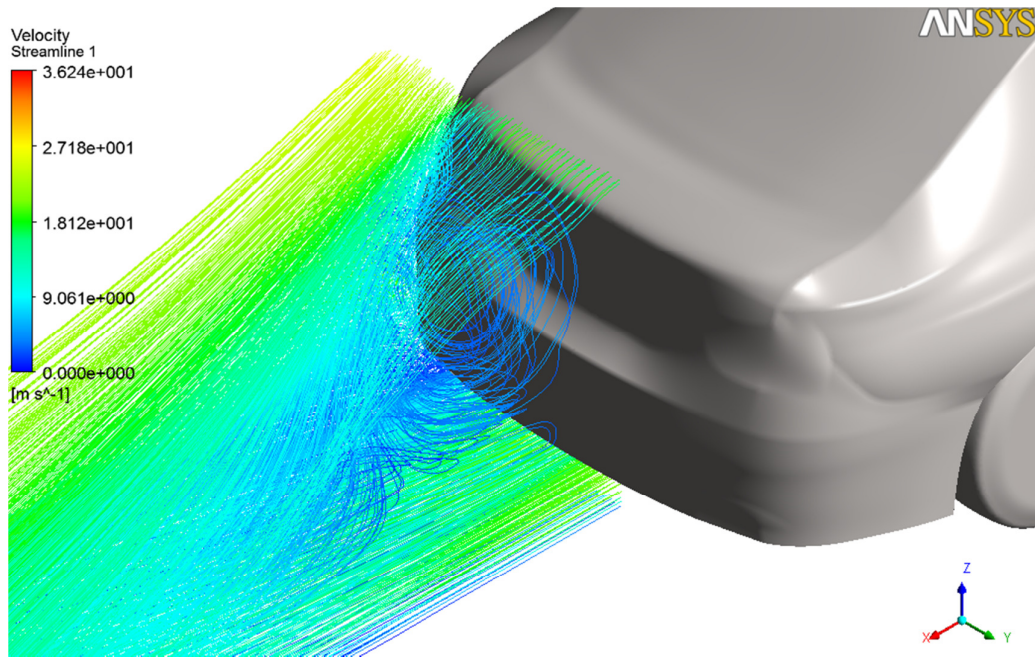


Figure 6.33 3-D streamlines at the wake region predicted by realizable $k-\epsilon$

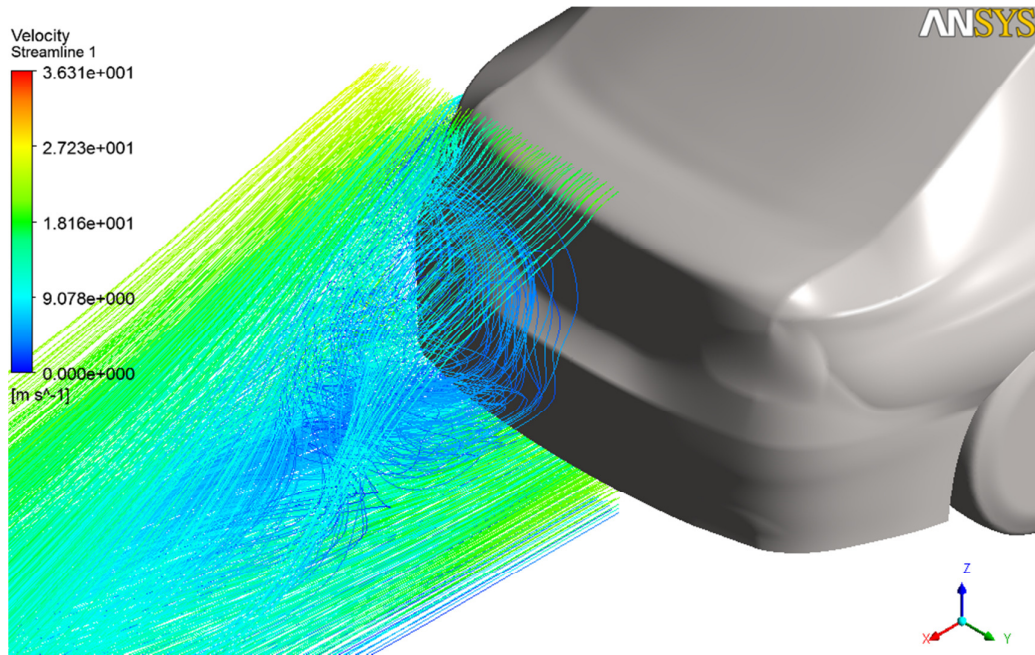


Figure 6.34 3-D streamlines at the wake region predicted by RNG $k-\epsilon$

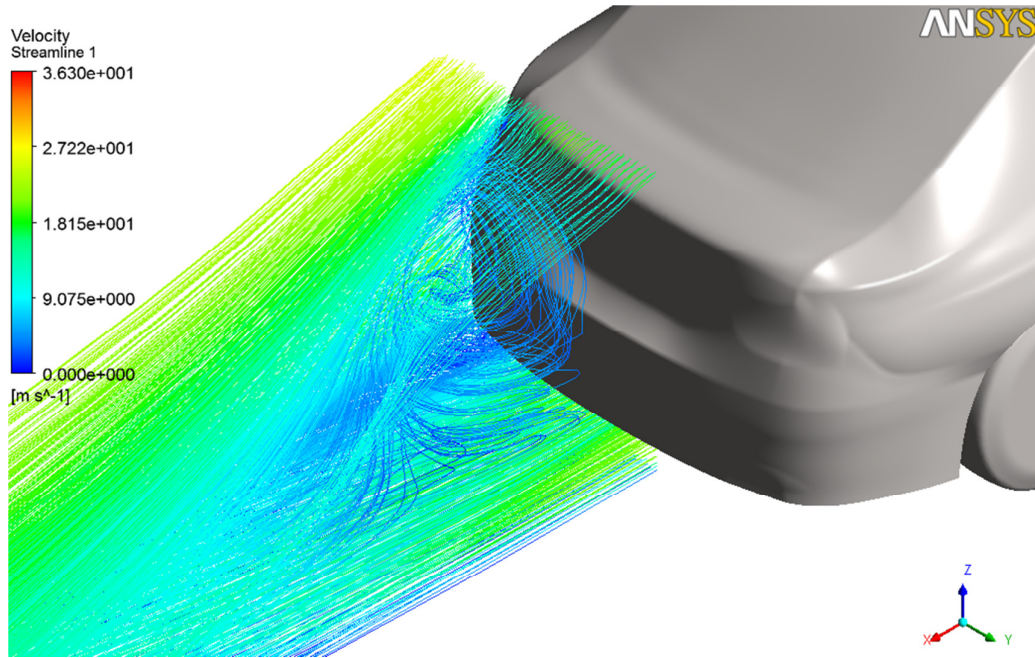


Figure 6.35 3-D streamlines at the wake region predicted by RSM

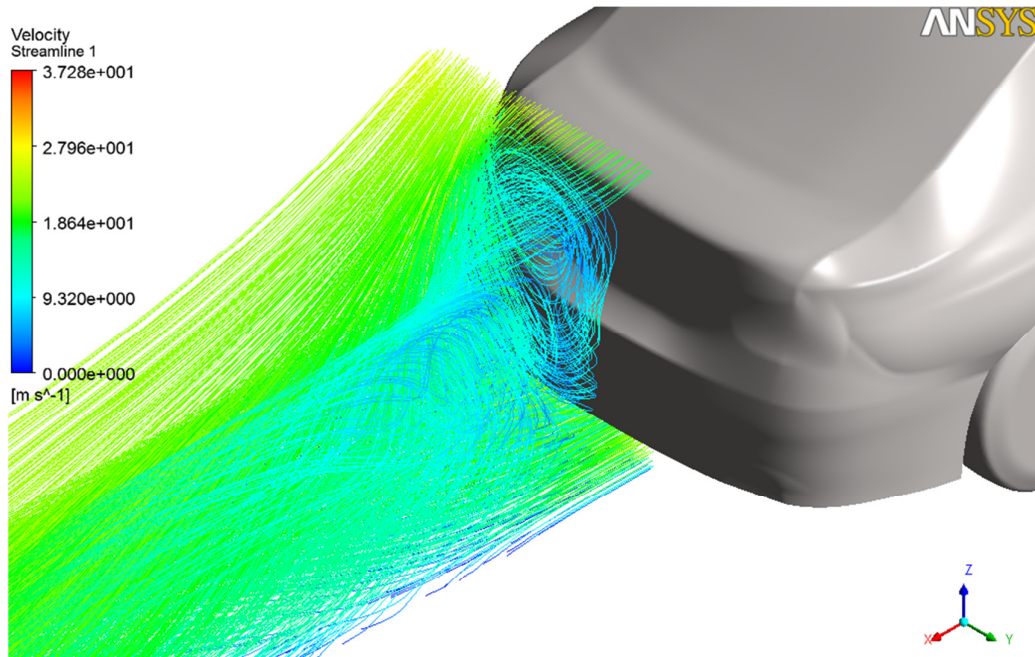


Figure 6.36 3-D streamlines at the wake region predicted by Spalart-Allmaras model

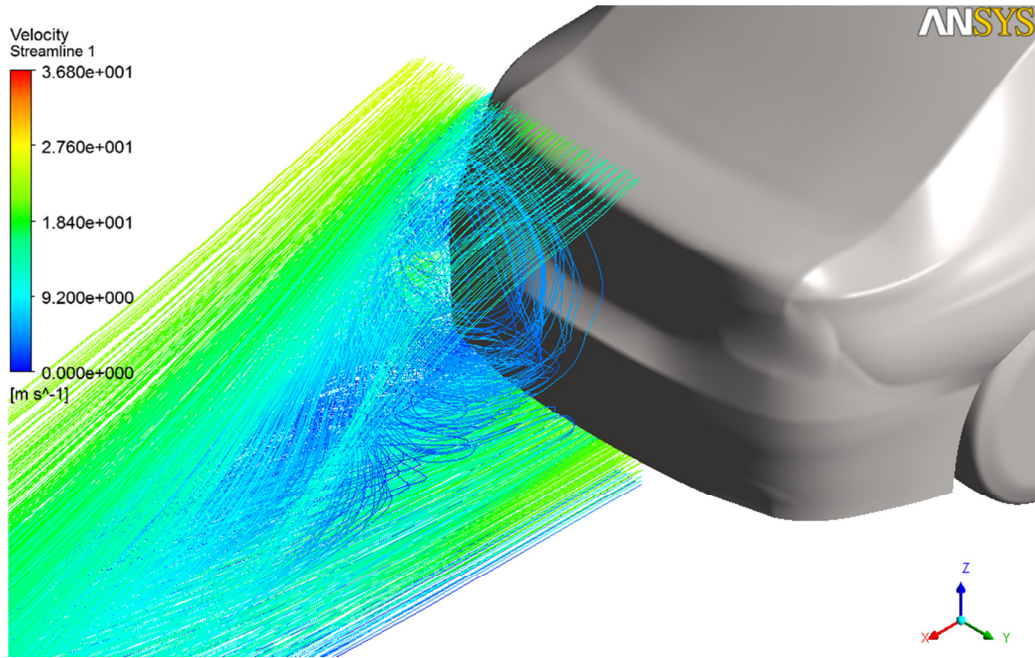


Figure 6.37 3-D streamlines at the wake region predicted by SST $k-\omega$

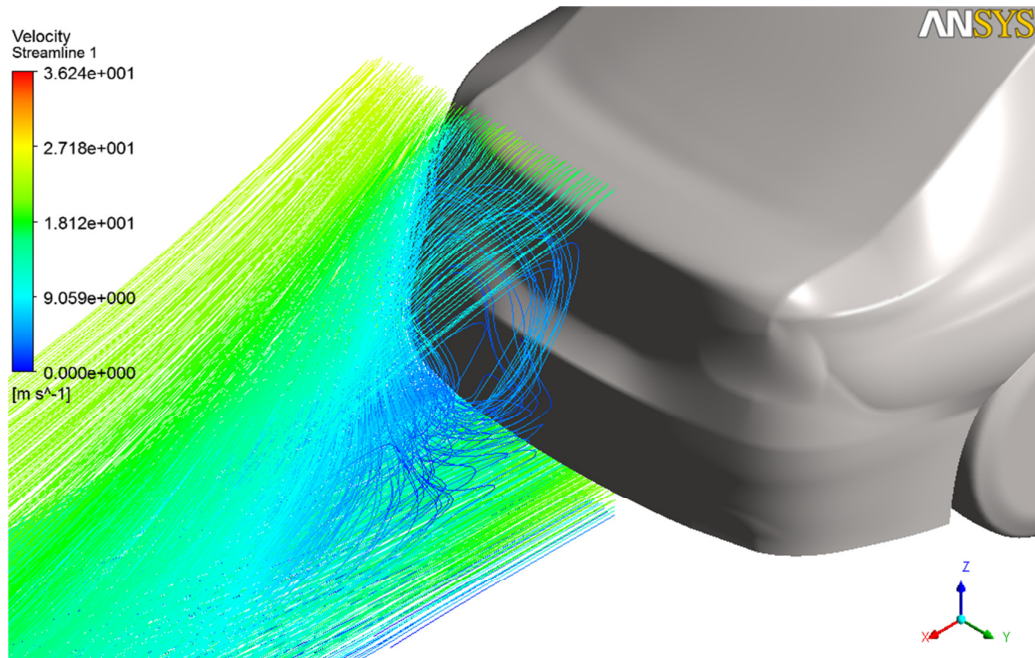


Figure 6.38 3-D streamlines at the wake region predicted by standard $k-\epsilon$

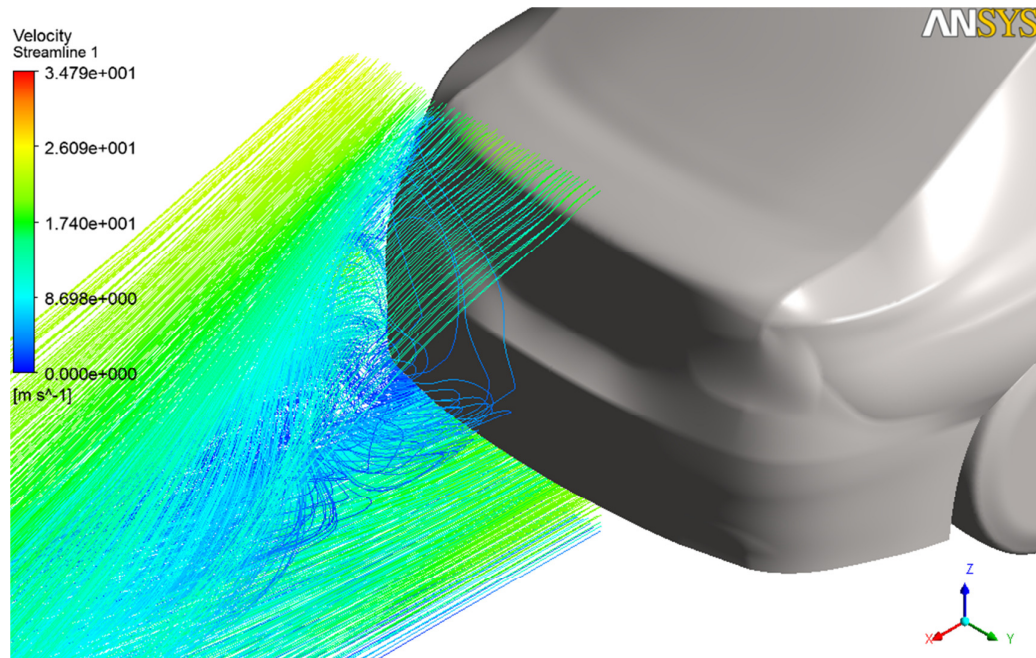


Figure 6.39 3-D streamlines at the wake region predicted by standard $k-\omega$

It can be said that turbulence models except for standard $k-\varepsilon$ and Spalart-Allmaras models, give realistic flow patterns and as it is seen in Figures 6.33, 6.34, 6.35, 6.37 and 6.39, vortices at the wake region interact with the flow leaving the trunk, side edge and the flow coming from under the body.

In Figures 6.40 to 6.46, surface streamlines obtained with different turbulence models in a plane parallel to xy -plane ($z = 0.02$ m) are presented. Half of these figures were obtained by using mirror imaging.

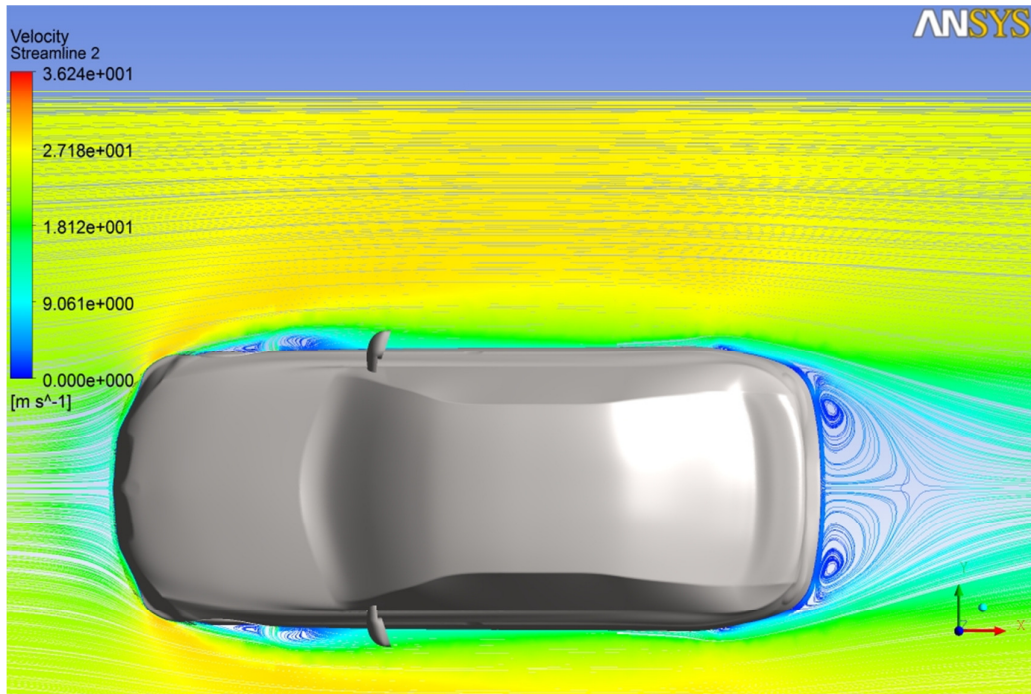


Figure 6.40 Streamlines predicted by realizable $k-\varepsilon$ model

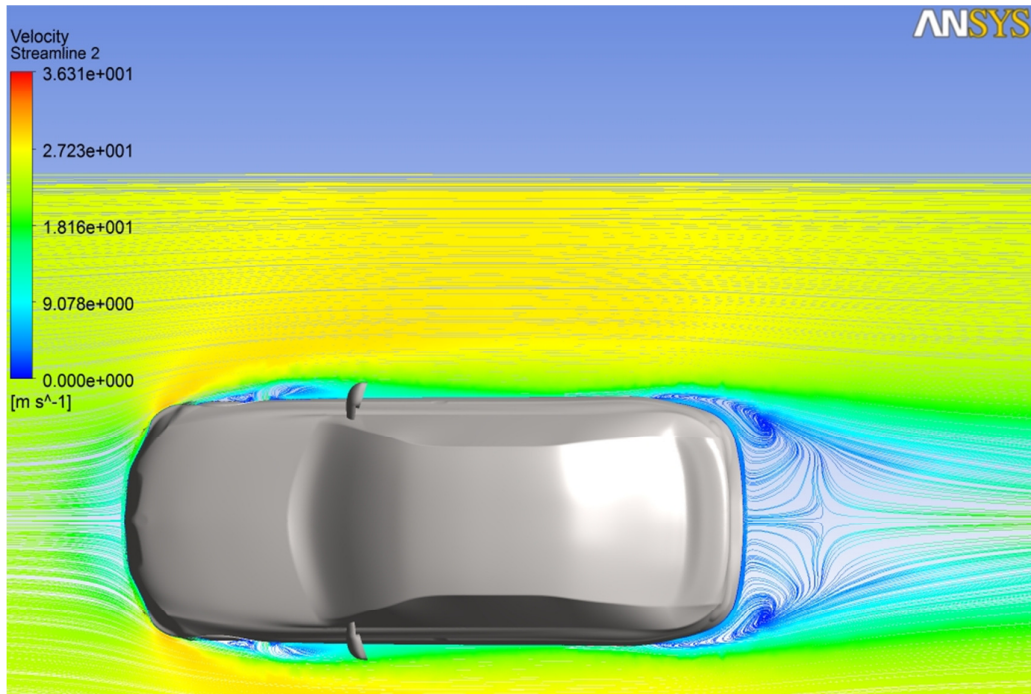


Figure 6.41 Streamlines predicted by RNG $k-\varepsilon$ model

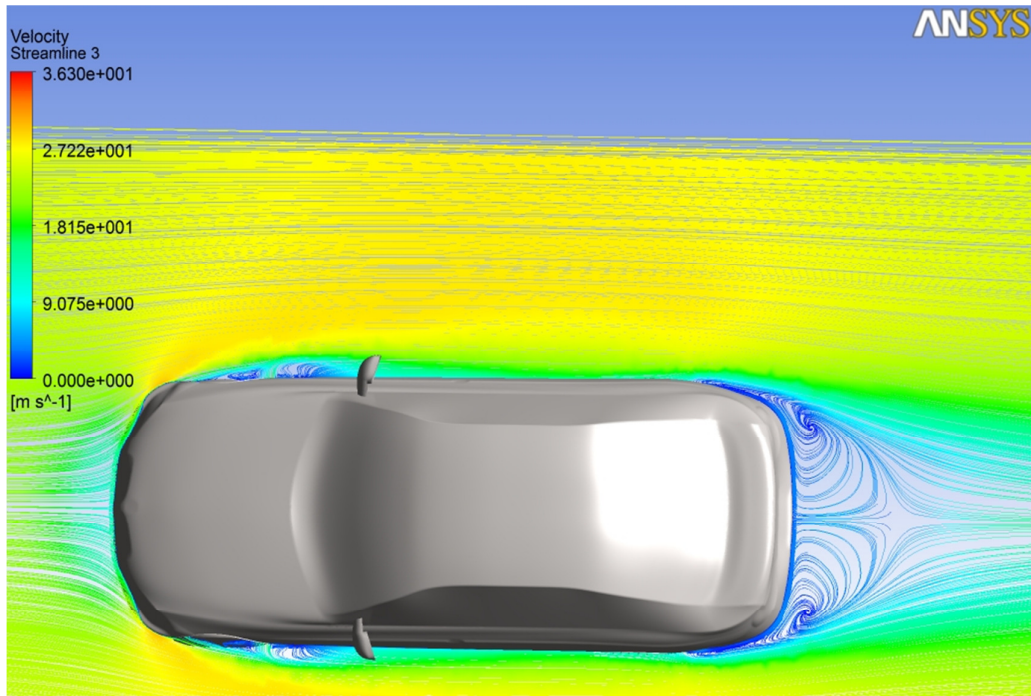


Figure 6.42 Streamlines predicted by Reynolds stress model

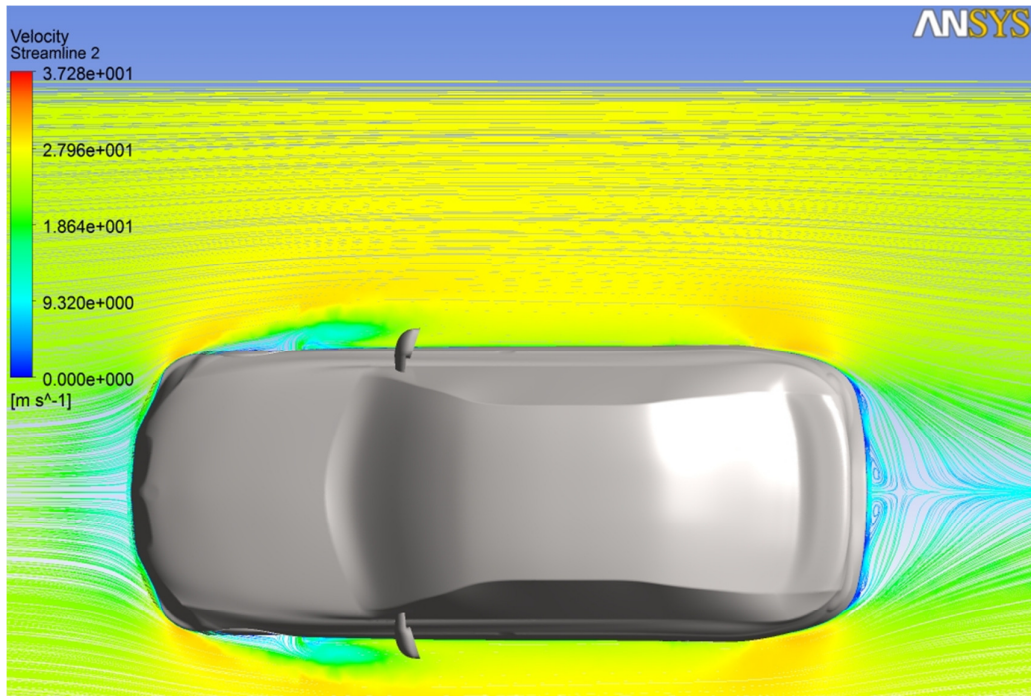


Figure 6.43 Streamlines predicted by Spalart-Allmaras model

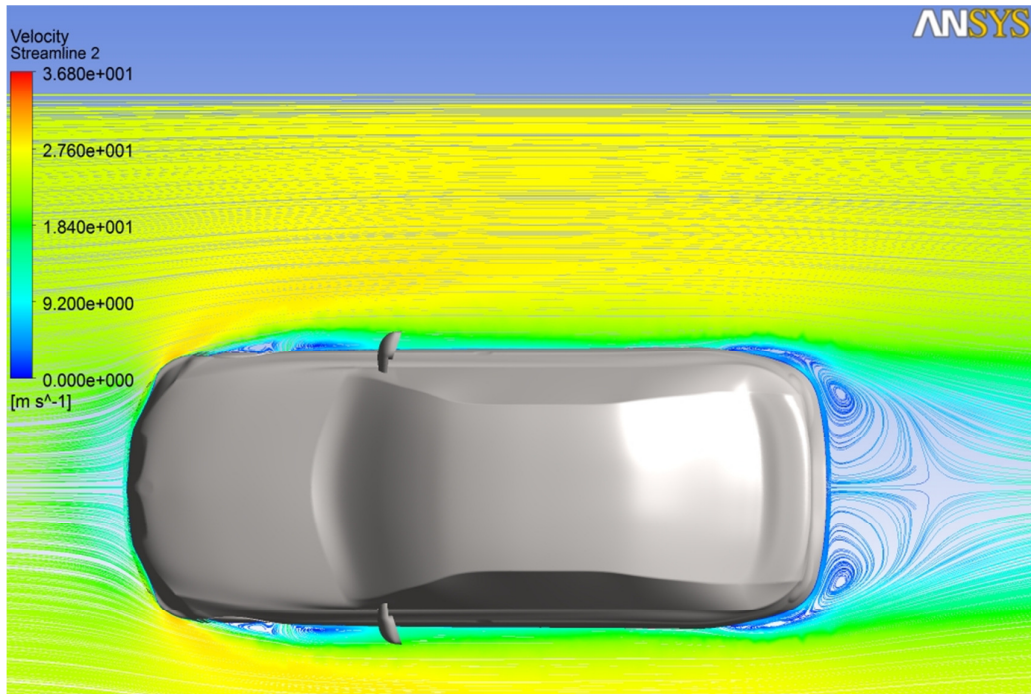


Figure 6.44 Streamlines predicted by SST $k-\omega$ model

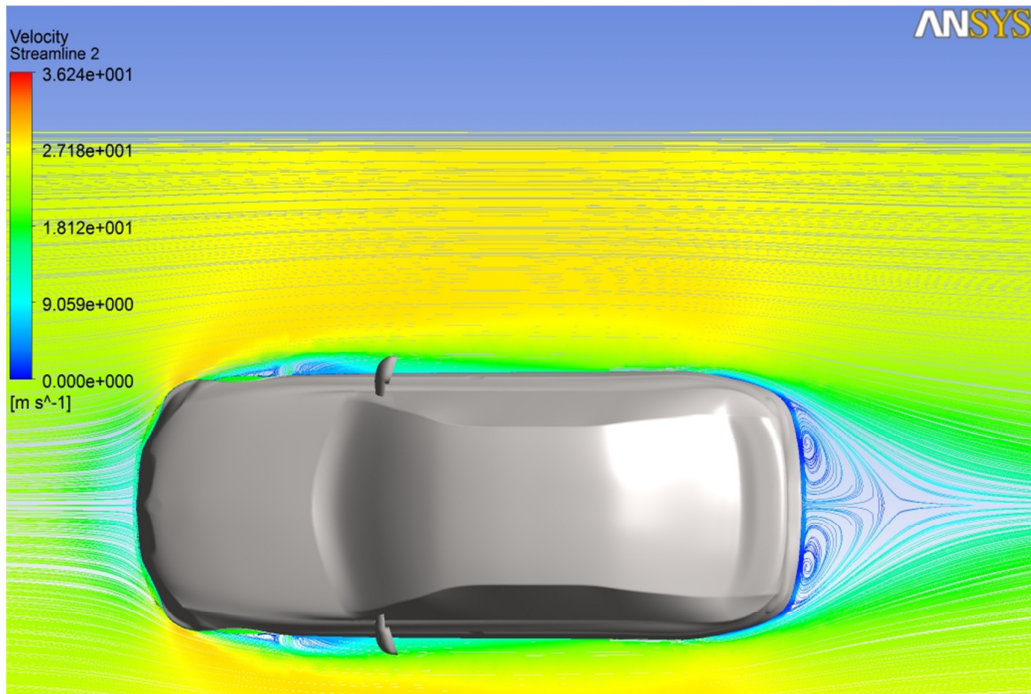


Figure 6.45 Streamlines predicted by standard $k-\epsilon$ model

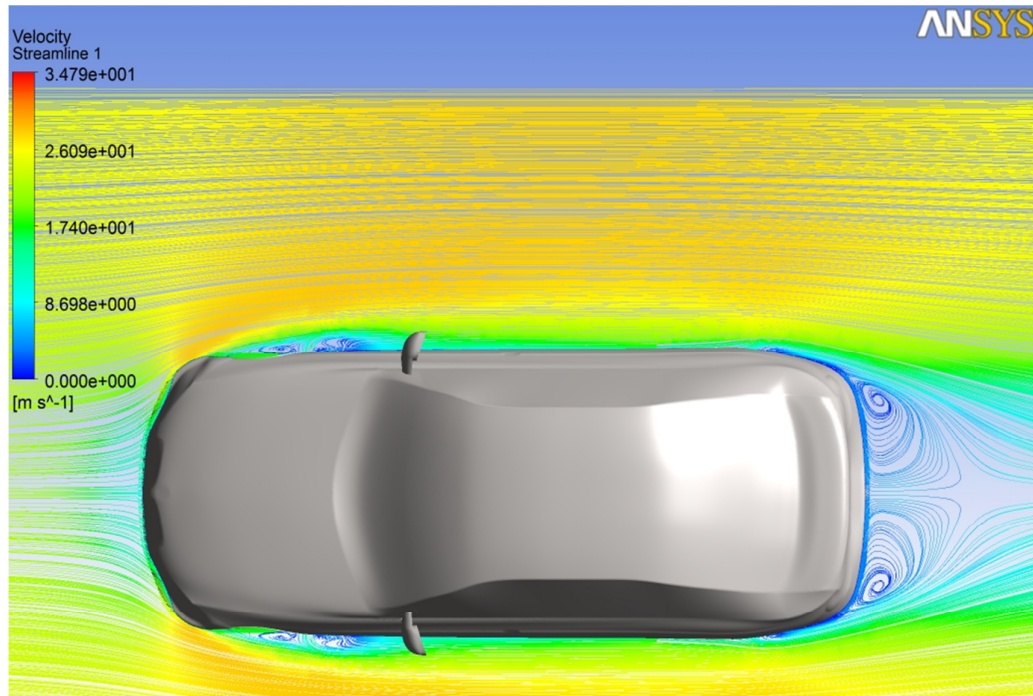


Figure 6.46 Streamlines predicted by standard $k-\omega$ model

As it is seen in Figures 6.40 to 6.46, flow separates from the side surface of the car where the front wheels are, then reattaches to surface at the beginning of the front door. This separation is not fully observed with Spalart-Allmaras model. Then flow follows the side surface at almost constant speed. It separates again where the back door finish line is and contributes the formation of vortices at wake region of the car by the suction effect in the low pressure zone. SST $k-\omega$, RNG $k-\varepsilon$ and RSM models predicted that region larger compared to other models. On the other hand, wake vortices practically were not observed with Spalart-Allmaras and it was observed very small wake region with standard $k-\varepsilon$ turbulence model.

In the evaluation of turbulence models, computational efforts are another important parameter. Because computational efforts is one of the important superiorities of CFD methods over experiments.

In Table 6.12, computational efforts required by each turbulence models are presented.

Table 6.11 Turbulence model evaluation based on computational efforts

Turbulence Model	Number of Iterations	Time	Allocated Memory
Realizable $k-\varepsilon$	2100~2700	10~15 hrs	~2 Gb
RNG $k-\varepsilon$	1600~2100	10~15 hrs	~2 Gb
Reynolds Stress	3800~4400	~2.5 days	~3 Gb
Spalart-Allmaras	800~1000	4~8 hrs	~1.5 Gb
SST $k-\omega$	2500~2700	14~19 hrs	~2 Gb
Standard $k-\varepsilon$	1700~2000	10~15 hrs	~2 Gb
Standard $k-\omega$	2200~2800	14~17 hrs	~2 Gb

By taking average of times and number of iterations required for different analyses with different velocities for the same turbulence models, following graphs are drawn (Figure 6.47 and 6.48).

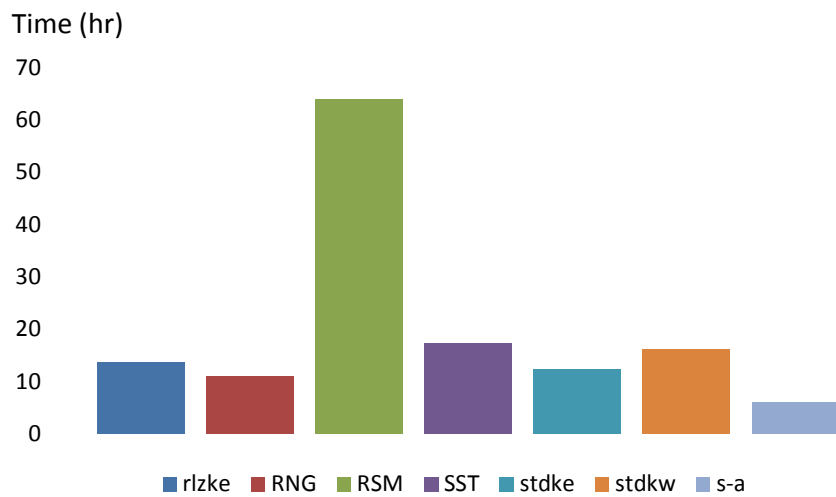


Figure 6.47 Average time required for turbulence models

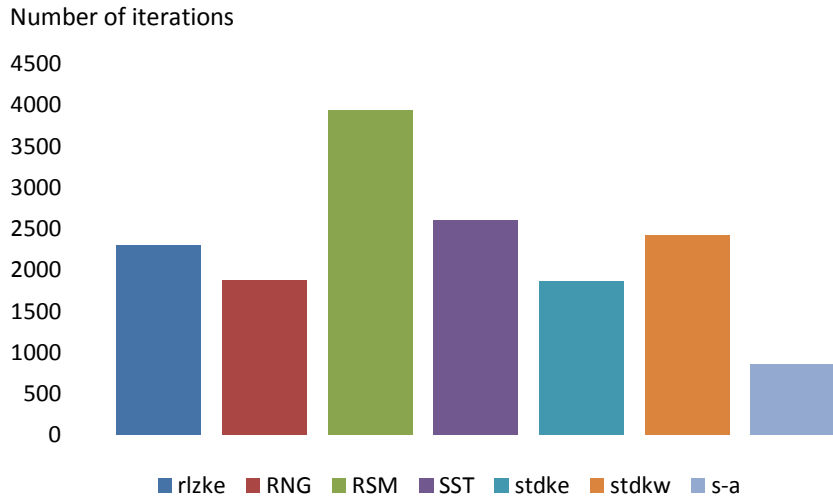


Figure 6.48 Average numbers of iterations for turbulence models

According to Table 6.12 and Figures 6.47 and 6.48, the most time and resources requiring model was the RSM. Although it required too much time and memory it did not excel the other turbulence models. As it was stated in Chapter 2, RSM may be used in simulations containing challenging flow and geometrical conditions. In practical engineering applications, especially in automobile industry, it can be said that RSM is not practical for CFD analysis.

Among the models that accurately predicted the drag and pressure coefficients and flow patterns around the car, standard $k-\omega$ and RNG $k-\varepsilon$ models required less computational effort.

The other model that should be remarked is the Spalart-Allmaras model. In the literature it has been stated that this model is relatively new and still needs to be verified and improved [15]. But in terms of time and memory requirements, it was the most economical model in the analyses.

It can be said that, CFD analysis for automobile aerodynamics require high computer properties (memory, processor etc.). Therefore, efficiency and economy are the features that are looked for in turbulence models of course with accuracy.

According to all analyses presented in this section, the following brief comments on tested turbulence models can be made.

Standard $k-\varepsilon$ Model

- Drag results are not satisfactory. C_D is overestimated for 5m/s and 9m/s about 35% and 10% respectively. And it is underestimated for high velocities 21 m/s and 25 m/s about 5% and 9% respectively.
- Pressure coefficient results are on the average of other models except for port6. At this port the most inaccurate C_P result among other models is obtained. The error is 66%.
- General flow pattern around the car is predicted unrealistically. In the wake region, any vortex is not fully sensed. Also no separation and vortex formation are observed at the sides of the car.
- Time and memory usage of this model is good. In terms of computational cost, this model is very economical compared to other models.

RNG $k-\varepsilon$ Model

- Drag results are on the average of other models.
- In terms of general trend of pressure coefficient variation this model is the most accurate one. Pressure coefficients at challenging ports 6 and 11 are relatively accurate. The error is 47% and 18% at those ports respectively.
- General flow pattern around the car is predicted realistically. Two counter rotating vortices at the wake are observed. These vortices are very common for the type of automobiles which is considered in this study. At the sides of the car two local separation and reattachment zones are also observed. Furthermore separated flow on the rear window is observed at lower velocities.
- In terms of computational cost, this model is one of the most economical models.

Realizable $k-\varepsilon$ Model

- Drag results is under the average of other models in terms of accuracy.
- Pressure coefficient results are on the average of other models. Like other models, pressure peak at port 6 is not sensed and pressure at port 11 is overestimated.
- General flow pattern around the car is predicted realistically.
- Computational cost of this model is a bit high compared to other $k-\varepsilon$ models. Despite higher computational cost, this model does not excel RNG $k-\varepsilon$ model.

Standard $k-\omega$ Model

- In terms of drag results, this model gives most accurate results. For velocities between 13-25 m/s, error at C_D is under 2%.
- Pressure distribution is relatively accurate. Pressure coefficient at port 11 calculated more accurately compared to other models. Error is 23% at that port.
- Wake vortex is predicted as much stronger and recirculation region at the wake is predicted as larger compared to other models. Furthermore at the beginning of the windshield a little vortex formation is observed under local separation bubble. Flow at the sides is predicted as similar to other models.
- Computational cost is higher than $k-\varepsilon$ models. But this model excels $k-\varepsilon$ models according to overall results.

SST $k-\omega$ Model

- Drag results are on the average of other models.
- Pressure coefficient results are on the average of other models. Like other models, pressure peak at port 6 is not sensed and pressure at port 11 is overestimated.
- General flow pattern around the car is predicted realistically. Contribution of side flow separation to recirculation region at the wake is predicted as much stronger compared to other models.

- This model is the most computational efforts requiring two equation model tested in this study. But computational time is not very far to average value of other two equation models

Reynolds Stress Model

- Drag results are on the average of other models.
- Pressure coefficient results are on the average of other models.
- General flow pattern around the car is predicted realistically. A little vortex formation inside separation bubble is observed at the beginning of the windshield. Also, separated flow on the rear window is observed at lower velocities. Unlike standard $k-\omega$, Spalart-Allmaras and $k-\varepsilon$ models, separation at the rear side edge of the car is predicted early.
- According to the results, RSM is the most time and memory consuming model. However, it has no clear superiority over $k-\omega$ models.

Spalart-Allmaras Model

- Most inaccurate drag results are obtained with this model.
- Pressures coefficients obtained at ports 9 and 11 as completely inaccurate. At port 11 pressure coefficient value contains 39% error.
- General flow pattern around the car is predicted unrealistically. Wake region predicted very unrealistically. At this region it is not captured any vortex. Also it is not observed any separation bubble at the sides of the car.
- This is the most economical turbulence model tested in this study. Computational time is far behind the average of other models.

CHAPTER 7

CONCLUSION AND RECOMMENDATIONS

7.1 Conclusion

Investigating the turbulence models and comparing their reliabilities and performances on the CFD simulations of aerodynamics of passenger cars were the main aims in this study. In this context firstly, past studies were investigated. Then general comments of some turbulence models were given in Chapter 2.

In Chapter 3, fundamentals of aerodynamics and aerodynamic characteristics of passenger cars were mentioned. In this chapter it was seen that; aerodynamic characteristics affect directly the important parameters of cars such as economy, performance, visibility.

In Chapter 4 and Chapter 5, fundamental equations for fluid flow and the properties and modeling of turbulent flows were investigated elaborately. Then turbulence models were evaluated based on their theories, historical developments and availabilities on engineering applications.

Lastly in Chapter 6, in order to test the reliability of turbulence models and to compare the performances of them; an aerodynamic CFD analysis with several turbulence models of a model car was made by simulating the wind tunnel tests of Aka [4] which was conducted with the same car model. At the end of analyses, results were investigated in terms of drag coefficient, pressure and velocity distributions, computational efforts and general flow pattern around the car.

In the determination of drag coefficient, it was seen that standard $k-\omega$ model gives more accurate results in terms of C_D .

Pressure coefficient at different ports located on the car along its symmetry plane was determined for 25 m/s velocity. It was observed that general trend of pressure variation accurately predicted except for some regions. All turbulence models could not capture the pressure peak at the beginning of the ceiling. Relatively good results were obtained with RNG $k-\varepsilon$ compared to other models at that region. Turbulence models also overpredicted the pressure at back of the car (port 11) about 25%. Relatively good results were obtained at that port by using RNG $k-\varepsilon$ and standard $k-\omega$ models.

Thereafter turbulence models were compared by presenting streamlines and velocity vectors around the car. Although there was no experimental data on flow pattern around the car, differences of flow patterns obtained by different turbulence models were investigated. It was seen that Spalart-Allmaras and standard $k-\varepsilon$ models gave unrealistic flow patterns at the wake.

Lastly turbulence models were evaluated in terms of computational efforts. In this context; required time, number of iterations and allocated memory for turbulence models were investigated. It was observed that, most time and memory consuming model was RSM and most economical one was Spalart-Allmaras model.

According to results it can be said that, RNG $k-\varepsilon$ and standard $k-\omega$ models stand one step ahead of the other models. Relatively accurate drag and pressure results were obtained with those models. Also they gave realistic flow patterns around the car. Their computational costs were average compared to other two-equation models.

In a general perspective, most of the turbulence models give relatively reliable results for determining aerodynamic properties of BMW 3-series car. But it should be emphasized that the car geometry under consideration is less challenging for turbulence models when it compared to that of truck, van or bus etc. Therefore it is possible to say that all turbulence models may not predict the aerodynamic characteristics of these vehicles accurately. But in recent years, most of the passenger cars have been producing in such a way that they give little disturbance to the flow around the car as the one investigated in this study.

It is seen that although some turbulence models (Spalart-Allmaras, standard k- ϵ) predicted drag coefficient not too bad, they gave very unrealistic wake pattern.

7.2 Future Work Recommendations

The following recommendations can be taken into consideration as a future work.

Because of the limited memory sources, no grid refinement study was made in this study. The same analyses may be made again with systematic grid adaption cycles for understanding the effect of mesh resolution. Usage of finer mesh will also offer to user to use of enhanced wall treatment option of Fluent. Hence the obstacles of wall functions will be eliminated and near wall region will be solved to its viscous sublayer.

Except for the turbulence models that used in this study, some other turbulence models that cannot be in Fluent as default, can be implemented and tested by using Fluent's user-defined function (UDF) property. Also, an unsteady analysis can be made by using LES for better understanding of the wake flow properties.

Besides the drag force, lift force and pitching moment can be investigated and compared with experimental results.

The turbulence models which are used in this study can be tested in determination of aerodynamic characteristics of different vehicle types such as trucks, buses and trains. And obtained data can be compared with the results of this study.

The future works mentioned in this section will be more efficient with the support of commercial automotive companies.

REFERENCES

- [1] Çakmak, M. A., “Kara Taşıtlarının Aerodinamik Bakımdan İncelenmesi” Mühendis ve Makine Dergisi, 489: 15-25, 2000
- [2] Wong, J. Y., “Theory of Ground Vehicles”, John Wiley & Sons, Canada, 221-239, 2008
- [3] Örselli E., “Computation of Drag Force on Single and Close-Following Vehicles”, MSc Thesis, METU, Ankara, September, 2006
- [4] Aka H., “Study on aerodynamic characteristics of a passenger car in a wind tunnel”, MSc Thesis, Gazi University, Ankara, 2003
- [5] Ahmed, S. R., Ramm, G. and Faltin, G., “Some salient features of the time averaged ground vehicle wake” SAE Transactions, Volume 93, Part 2, 473-503, 1984
- [6] Moser. A., Liu. Y., “Numerical modeling of airflow over the Ahmed Body”, Proceedings of the 11th Annual Conference of the CFD Society of Canada, Vancouver, BC, Canada, May 28-30, 2003
- [7] Durand, L., Kuntz, M., Menter, F., “Validation of CFX-5 for the Ahmed Car Body”, 10th joint ERCOFTAC (SIG-15)-IAHR-QNET/CFD Workshop on Refined Turbulence Modeling University of Poitiers, France, October 10-11, 2002
- [8] Barbone, L., Gattei, L., Rossi, R., “Identification and analysis of turbulent structures around a simplified car body”, 2nd European CFD Conference, Frankfurt, Germany, 2005

- [9] Han, T., “Computational analysis of three-dimensional turbulent flow around a bluff body in ground proximity”, AIAA J. (27-9), pp. 1213-1219, 1989
- [10] Han, T., Sumantran, V., Haris, C., Kuzmanov, T., Huebler, M., Zak, T., “Flowfield simulations of three simplified vehicle shapes and comparisons with experimental measurements”, SAE Technical Paper Series 960678, 820-835, 1996
- [11] Perzon, S., Janson, J., Höglin, L., “On comparisons between CFD methods and wind tunnel tests on a bluff body”, SAE Technical Paper Series, 1999-01-0805, 1-11, 1999
- [12] Makowski, F.T., Kim, S.E., “Advances in external-aero simulation of ground vehicles using the steady RANS equations”, SAE Technical Paper Series, 2000-01-0484, 1-13, 2000
- [13] Şahin C., “Prediction of Aerodynamic Drag Coefficient for Heavy Vehicles with Computational Fluid Dynamics Method”, MSc Thesis, ITU, 2008
- [14] İnce, T. İ., “Aerodynamic Analysis of GTD Model Administrative Service Vehicle”, PhD. Thesis, Gazi University, Ankara, 2007
- [15] ANSYS Fluent 13, User Guide
- [16] Barnard, B. H., “Road Vehicle Aerodynamic Design”, Longman, London, 1-50, 255-270, 1996
- [17] Çengel, Y. A. and Cimbala, J. M., “Fluid Mechanics” McGraw Hill, 170-200, 299-300, 2008
- [18] Houghton, E. L. and Carpenter, P. W., “Aerodynamics For Engineering Students”, Butterworths, London, 29-65, 2003

- [19] Gillespie, T.D., “Fundamentals of vehicle dynamics” 4th ed., Book News, Inc., Portland, OR, 79-123, 1992
- [20] Demircioğlu, T. K., “Aerodynamic Analysis of a Vehicle Model and its Simulation with Finite Element Method”, MSc Thesis, Balıkesir University, 6-9, 2007
- [21] Hucho, W. H., “Aerodynamics Of Road Vehicles”, Butterworths, London, 1-46, 106-214, 1987
- [22] Hucho, W. H., “Aerodynamics Of Road Vehicles-State of the Art and Task for the Future”, Presentation, Steyr, 25-27.06.2003
- [23] J.H. Ferziger and M. Peric, “Computational Methods for Fluid Dynamics”, 3rd ed., Springer, 2002
- [24] Fu-Hung Hsu, “Design of Tractor-Trailer Add-On Drag Reduction Devices Using CFD”, PhD Thesis, University of California, 29-36, 2009
- [25] Versteeg, H. K., Malalasekera, W. “An introduction to computational fluid dynamics- The finite volume method”, Longman Scientific & Technical, London, 10-84, 1995
- [26] Autospeed,
http://autospeed.com/cms/title_Aero-Testing-Part-4/A_108676/article.html,
 last access on: 23.08.2011
- [27] Kasravi,
<http://www.kasravi.com/cmu/tec452/Aerodynamics/VehicleAero.htm>,
 last access on: 18.08.2011
- [28] Cortana, http://www.cortana.com/Drag_Description.htm, last access on: 18.08.2011
- [29] “Turbulence theory gets a bit choppy”, USA Today, September 10, 2006,
http://www.usatoday.com/tech/science/columnist/vergano/2006-09-10-turbulence_x.htm, last access on: 18.08.2011

- [30] University of Kentucky, Advanced CFD Group, "Lecture Notes", www.engr.uky.edu/~acfd/lctr-notes634.pdf, last access on: 18.08.2011
- [31] Karman, T. von. "Some remarks on the statistical theory of turbulence", Proc. 5th Int. Congr. Appl. Mech., Cambridge, MA, 347, 1938
- [32] Hinze, J. O., "Turbulence", McGraw-Hill, New York, 1959
- [33] Nurul Muiz Murad, "Computational Fluid Dynamics of vehicle aerodynamics and associated acoustics", Phd Thesis, Swinburne University of Technology, Melbourne, Australia, 54-75, 2009
- [34] Free Dictionary, <http://encyclopedia2.thefreedictionary.com/Turbulent+Flow>, last access on: 18.08.2011
- [35] Amolife, <http://amolife.com/image/landscapes/volcanic-eruption-photography.html>: last access on: 18.08.2011
- [36] Sky-Chaser, <http://www.sky-chaser.com/mwcl2005.htm>: last access on: 18.08.2011
- [37] Argonne National Laboratory, http://www.anl.gov/Media_Center/logos20-2/blood01.htm, last access on: 18.08.2011
- [38] Ecomodder, <http://ecomodder.com/forum/showthread.php/hood-splitter-my-vw-16607-5.html>, last access on: 18.08.2011
- [39] C. G. Speziale, "Analytical methods for the development of Reynolds stress closures in turbulence", Annual Review of Fluid Mechanics, Volume 123, 107-157, 1991
- [40] Bradshaw, P., Cebeci, T. and Whitelaw, J. H., "Engineering calculation methods for turbulent flow", Academic Press, London, 1981

- [41] Baldwin, B. S. and Lomax, H., “Thin layer approximation and algebraic model for separated turbulent flow”, AIAA Paper, 78-257, 1978

- [42] Cebeci, T. and Smith, A. M. O., “Analysis of boundary layers”, Applied Mathematics and Mechanics, Vol. 15, Academic Press, Newyork, 1974

- [43] ANSYS Fluent Training Manual, Figes, Bursa, 2010

- [44] Tennekes, H. and Lumley, J. L., “A first course in turbulence”, MIT Press, Cambridge, MA., 1972

- [45] Launder, B. E. and Spalding, D. B., “The numerical computation of turbulent flows”, Comput. Methods Appl. Mech. Eng., Vol.3, pp. 269-289, 1974

- [46] Launder, B. E., Reece, G. J. and Rodi, W., “Progress in the development of a Reynolds stress turbulence closure”, J. Fluid. Mech., Vol. 68, Pt. 3, pp. 537-566, 1975

- [47] Schlichting, H. “Boundary layer theory”, 7th ed., McGraw Hill, Newyork, 1979

- [48] Lanfrit, M., “Best Practice Guidelines for Handling Automotive External Aerodynamics with Fluent v.1.2”, Fluent Deutschland GmbH, Darmstadt, Germany, 2005

- [47] Motor Industries Research Association Ltd., “MIRA: Automotive Engineering Test and Design World Leaders”, June 2006

- [48] Kapadia et. al., “DES over a reference Ahmed Car Model” AIAA Paper 03-0857, January, 2003

APPENDIX A

AHMED BODY STUDIES

In this section, CFD simulations on Ahmed Body will be presented. Ahmed Body is a well-known car shaped bluff body (Figure A.1). In CFD analyses, the original experiments of Ahmed [5] were simulated in Fluent software to investigate the wake formations and variation of drag coefficient with slant angle.

CAD model of Ahmed Body is shown in Figure A.1.

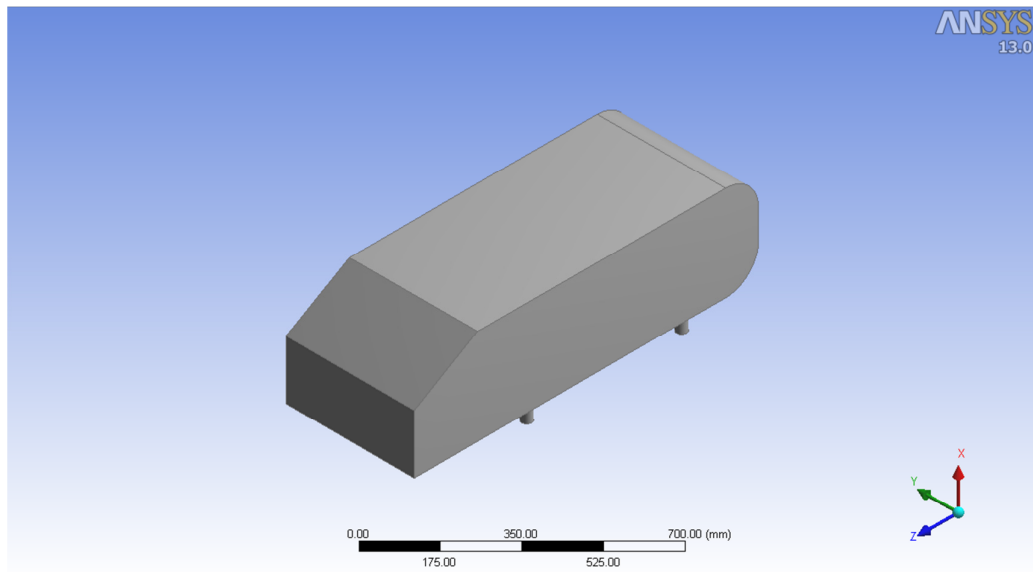


Figure A.1 CAD Model of Ahmed Body

Computational domain for Ahmed Body simulations was constituted faithfully to the original test section of Ahmed's experiments. To reduce the computational cost, halves of the vehicle and test section were utilized. Half domain dimensions are $w \times h \times l = 1.5 \times 2.75 \times 5$ meters.

The grid was generated similarly as in the Section 6.3 and it is shown in Figure A.2.

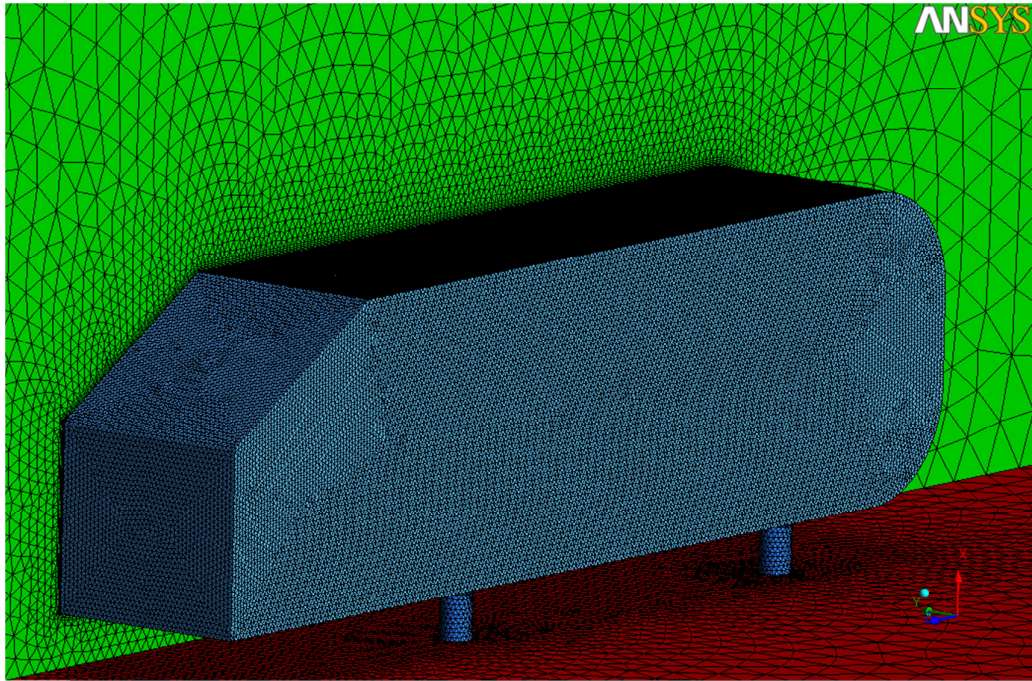


Figure A.2 The grid on the body, symmetry plane and road

Defined boundary conditions for CFD simulations are shown in Figure A.3

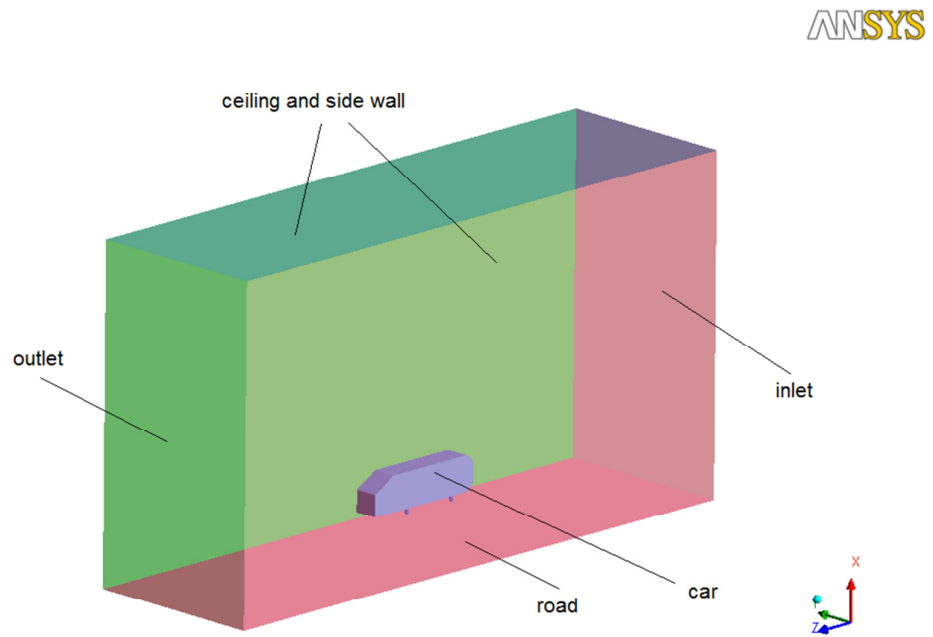


Figure A.3 Defined boundary conditions

Inlet of the domain was specified as velocity outlet. Outlet of the domain was specified as pressure outlet. The side-wall, ceiling and symmetry plane were specified as symmetry boundary condition because test section was open type in the experiments. The road and car were defined as no-slip walls.

The settings for the CFD simulations are shown in Table A.1

Table A.1 Settings for the boundary conditions

Test Section ($w \times h \times l$) m	1.5×2.75×5
Velocity (m/s)	60
ρ (kg/m ³)	1.18 @20 ⁰ C
μ (kg/ms)	1.837×10 ⁻⁵ @20 ⁰ C
Hydraulic diameter (m)	1.941
Turbulence intensity (%)	0.5
Frontal area (m ²)	0.0058

CFD analyses were made firstly for 25°, 30° and 35° slant angles. Drag results are presented in Table A.2.

Table A.2 Drag Results of Ahmed Body

	25° Slant Angle		30° Slant Angle		35° Slant Angle	
	C _D	Error (%)	C _D	Error (%)	C _D	Error (%)
Standard $k-\omega$	0.288	1.0	0.340	-10.0	0.278	6.9
Realizable $k-\varepsilon$	0.290	1.7	0.295	-21.9	0.293	12.7
Spalart-Allmaras	0.294	3.2	0.298	-21.2	0.301	15.8
Reynolds Stress	0.288	1.0	0.326	-13.7	0.291	11.9
Kapadia et.al. [48]	0.281	-1.4	-	-	0.252	-3.0
Barbone et. al. [8]	0.293	2.8	-	-	0.284	9.2
Experiment [5]	0.285	-	0.378	-	0.260	-

As it is seen in Table A.2, most accurate results were obtained for 25° slant.

In 25° slant mode, all turbulence models predicted drag coefficient accurately. And the error in the C_D values was lower than 4%. But all turbulence models predicted attached flow on the slant. Therefore a little separation bubble formed on the slant reported in the original experiments of Ahmed [5] was not captured by turbulence models. In Figure A.4, attached flow on the slant predicted by standard $k-\omega$ model is presented as streamlines on the symmetry plane. On the other hand turbulence models except for Spalart-Allmaras model predicted two counter rotating vortices at the back of the body realistically.

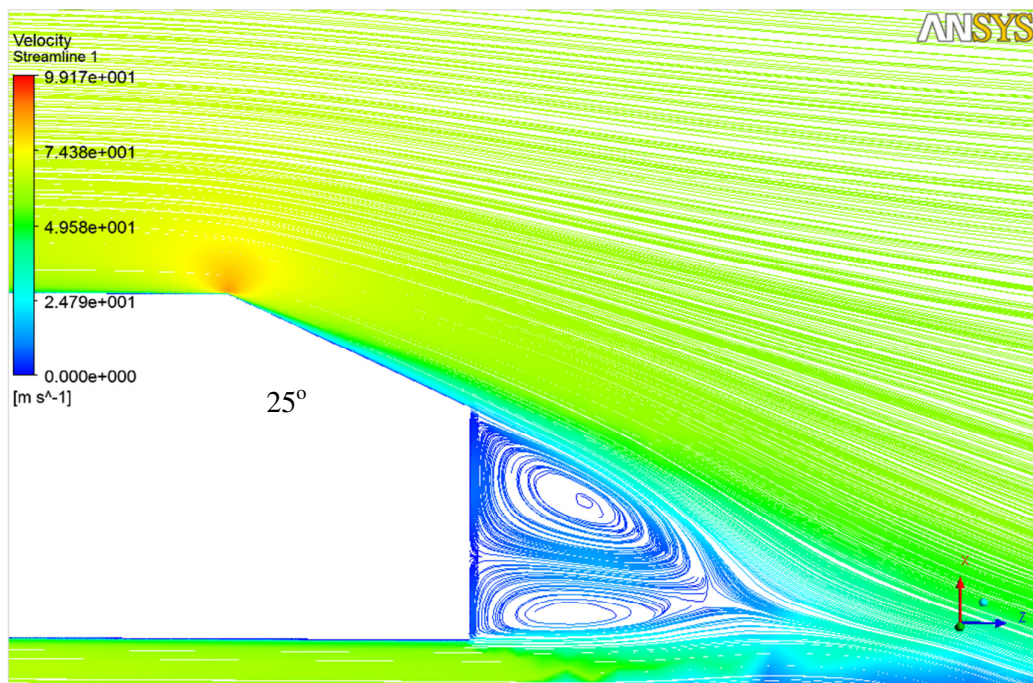


Figure A.4 Attached flow on the slant predicted by standard $k-\omega$

30° slant is the critical slant mode for the Ahmed Body. Because in the experiments, it was observed that for 30° slant mode, separation bubble on the slant reaches downstream edge of the slant and combines the vortices at the back of the body. Therefore this mechanism cause drag coefficient to have a peak at 30°. This peak was not sensed by realizable $k-\varepsilon$ and Spalart-Allmaras models. On the other hand with standard $k-\omega$ and Reynolds Stress turbulence models a reasonable peak in C_D was observed in the CFD simulations. Furthermore, with standard $k-\omega$ turbulence model

the separation bubble reported in Ahmed's experiments predicted realistically (Figure A.5). Nevertheless, the experimental peak value of the C_D was not captured exactly. Most accurate C_D value is 10% lower than the experimental value. Therefore in order to capture the peak value of C_D ; in addition to 25° , 30° and 35° slant angles, intermediate slant angles (27° , 29° , 31° and 33°) were investigated. Results of drag coefficients of intermediate slant angles are presented in Table A.3.

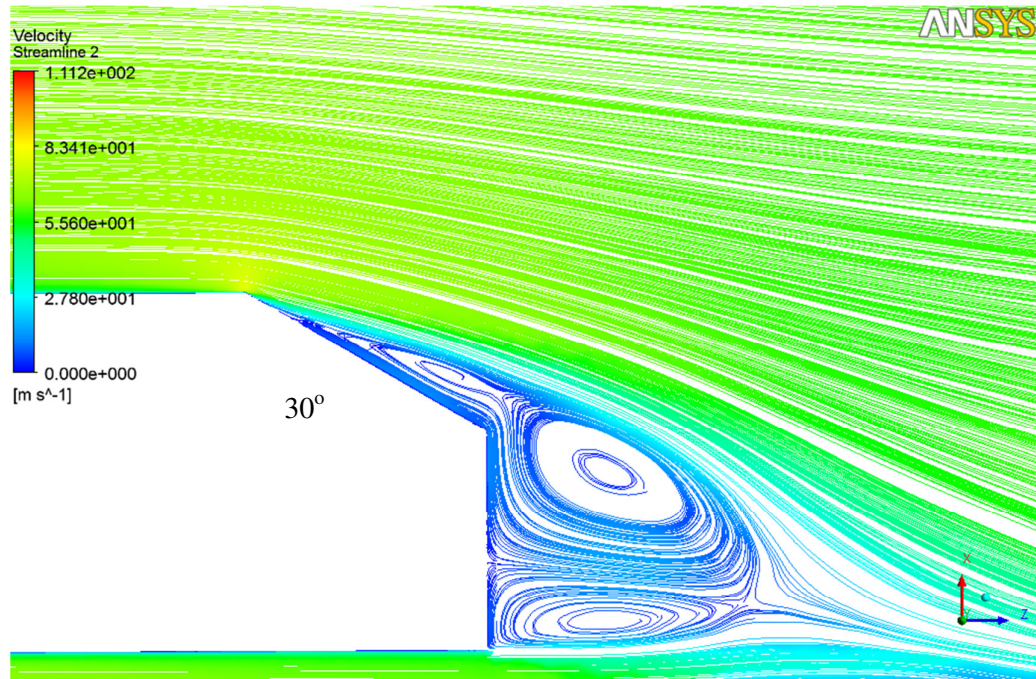


Figure A.5 Separated flow on the slant predicted by standard $k-\omega$

Table A.3 C_D Results for all slant angles

Slant Angle / Turbulence Model	25°	27°	29°	30°	31°	33°	35°
Standard $k-\omega$ Model	0.288	0.291	0.294	0.340	0.302	0.281	0.278
Realizable $k-\varepsilon$ Model	0.290	0.297	0.298	0.295	0.291	0.290	0.293
Spalart-Allmaras Model	0.294	0.292	0.295	0.298	0.290	0.301	0.301
Reynolds Stress Model	0.288	0.290	0.306	0.316	0.298	0.294	0.291

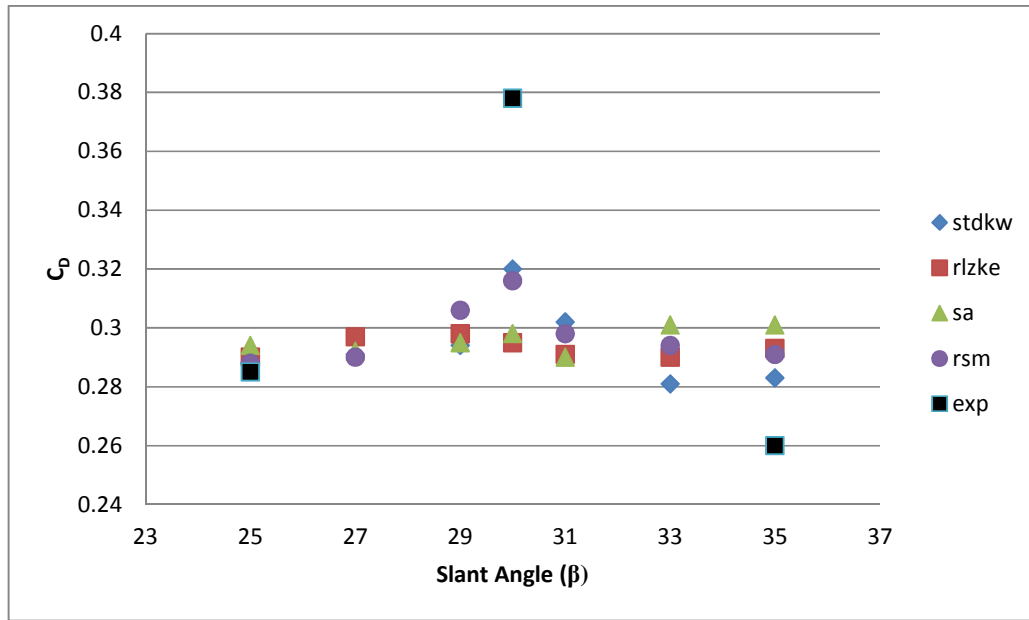


Figure A.6 Variation of drag coefficient with slant angle

According to all C_D results; it can be said that, the peak at the C_D was obtained for 30° slant mode as in the Ahmed's experiments but the value of C_D was underestimated by all turbulence models. Most accurate C_D results were obtained by using standard $k-\omega$ and RSM turbulence models.

For 35° slant C_D results obtained with turbulence models were satisfactory. Most accurate C_D result obtained with standard $k-\omega$ model which has 7% error. Wake formation obtained by that model is presented in Figure A.7.

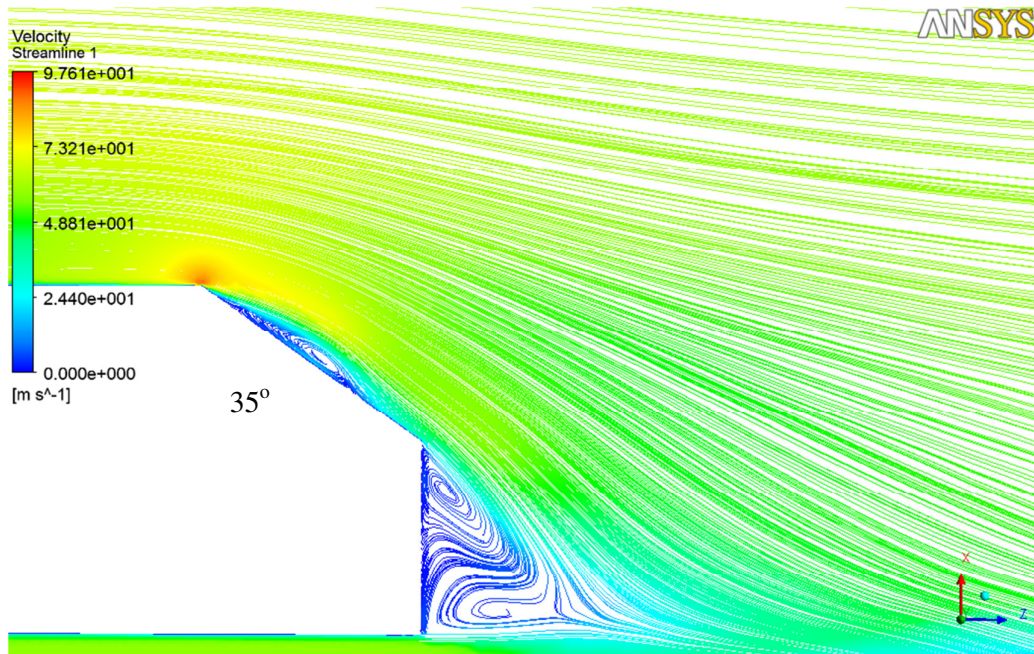


Figure A.7 Wake flow formation obtained with standard $k-\omega$ model

In Figure A.8 all turbulence models predictions on wake flow for critical slant angle 30° are presented.

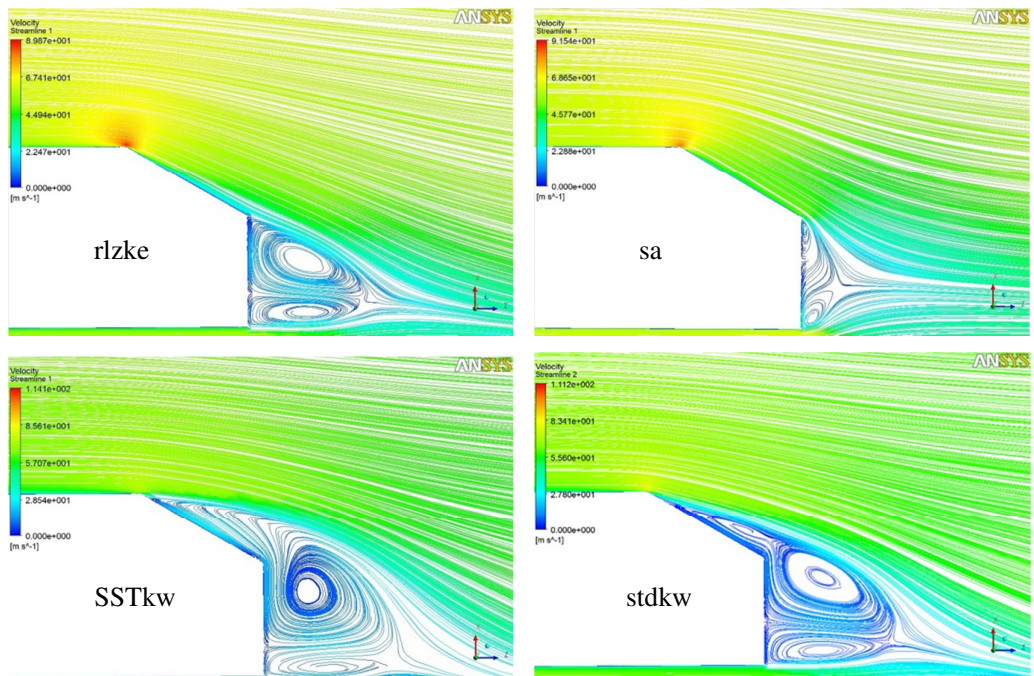


Figure A.8 Turbulence models predictions of wake flow at critical slant angle 30°

APPENDIX B

PRELIMINARY STUDIES

Preliminary studies are useful in many aspects. The effect of solution parameters and settings on the results can be seen by changing them in a controlled manner. Also it helps the user to check his/her capabilities in flow modeling. Due to these reasons, some preliminary studies with simplified car model known as MIRA (Figure B.1) were performed before beginning the actual analyses in this study.

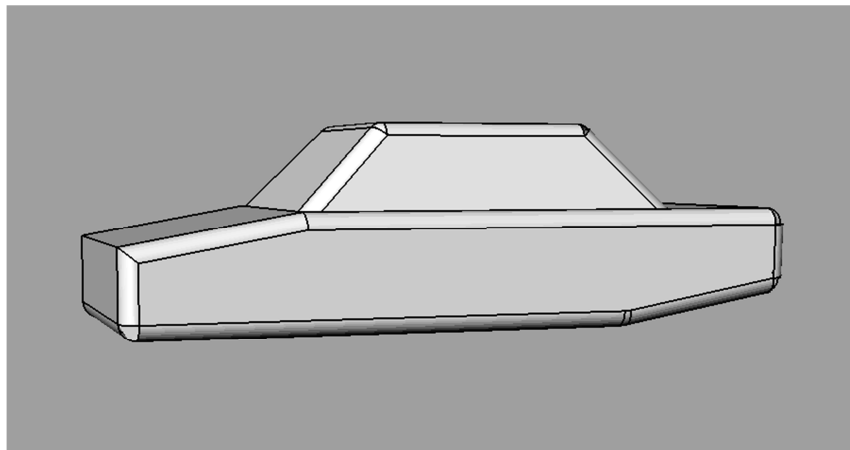


Figure B.1 MIRA Model

In preliminary studies;

- The effect of first order and second order discretization schemes
- The effect of standard and non-equilibrium wall functions

on the results were investigated.

In order to prevent comparison difficulties, only one type of turbulence model (Realizable $k-\varepsilon$) was utilized.

Four different analyses were conducted:

Case A: First order scheme, standard wall functions

Case B: Second order scheme, standard wall functions

Case C: First order scheme, non-equilibrium wall functions

Case D: Second order scheme, non-equilibrium wall functions

All cases were analysed with the settings written below;

Table B.1 Settings for preliminary studies

Test section	0.375×0.3×1
Velocity	19 m/s
ρ	1.10 kg/m ³
μ	1.807×10 ⁻⁵
Hydraulic diameter	0.335 m
Turbulence intensity [3]	0.22%
Outlet pressure [3]	-274 Pa
Reynolds number	2.9×10 ⁵
Frontal area	2.95×10 ⁻³ m ²

In Table B.2 the drag results of MIRA model for different cases are presented.

Table B.2 Drag results for different cases

Case	A	B	C	D	Exp [3]
C _D	0.385	0.355	0.295	0.313	0.327
Error (%)	17.7	8.6	-9.8	-4.3	-

Superior results were obtained by using second order discretization with non-equilibrium wall functions in case D. Errors in drag coefficient values obtained by using first order scheme (Case A and C) were out of acceptable limit. This result supports the references [3], [15] and [48].

APPENDIX C

EXPERIMENTAL LITERATURE RESULTS OF BMW MODEL CAR

All results of wind tunnel tests of Aka [4] are presented in Tables C.1 to C.9.

Table C.1 Pressure values measured on pressure ports 1-4

Velocity (m/s)	Re	Port 1		Port 2		Port 3		Port 4	
		ΔP_{avg}	C_P	ΔP_{avg}	C_P	ΔP_{avg}	C_P	ΔP_{avg}	C_P
3	57283	-0.3	-0.05	-10.3	-1.88	-6.3	-1.15	-6.7	-1.22
5	95472	0.3	0.02	-14.7	-0.96	-10.3	-0.68	-12.7	-0.83
7	133661	0.7	0.02	-25.3	-0.85	-17.7	-0.59	-24.0	-0.80
9	171850	0.7	0.01	-45.0	-0.87	-29.3	-0.57	-43.0	-0.83
11	210039	1.3	0.02	-60.0	-0.88	-37.3	-0.54	-56.0	-0.82
13	248228	1.3	0.01	-90.3	-0.88	-52.3	-0.51	-83.3	-0.81
15	286417	2.0	0.01	-121.7	-0.90	-66.7	-0.49	-111.7	-0.82
17	324606	3.3	0.02	-159.3	-0.93	-82.0	-0.48	-142.0	-0.82
19	362795	4.0	0.02	-204.3	-0.93	-102.0	-0.46	-185.0	-0.84
21	400984	4.0	0.01	-248.7	-0.92	-125.3	-0.47	-223.3	-0.83
23	439173	5.0	0.02	-302.0	-0.94	-149.0	-0.46	-269.3	-0.83
25	477362	6.0	0.02	-358.0	-0.94	-176.0	-0.46	-321.0	-0.84

Table C.2 Pressure values measured on pressure ports 5-8

Velocity (m/s)	Re	Port 5		Port 6		Port 7		Port 8	
		ΔP_{avg}	C_P	ΔP_{avg}	C_P	ΔP_{avg}	C_P	ΔP_{avg}	C_P
3	57283	-7.7	-1.40	-6.7	-1.22	-14.7	-2.68	-6.3	-1.15
5	95472	-22.0	-1.44	-15.3	-1.00	-26.7	-1.75	-20.0	-1.31
7	133661	-44.0	-1.47	-27.3	-0.91	-45.7	-1.53	-42.0	-1.41
9	171850	-74.0	-1.43	-49.3	-0.95	-76.7	-1.49	-71.7	-1.39
11	210039	-99.3	-1.45	-64.0	-0.93	-102.0	-1.49	-96.3	-1.41
13	248228	-148.7	-1.44	-96.0	-0.93	-155.3	-1.51	-144.3	-1.40
15	286417	-195.7	-1.45	-126.0	-0.93	-204.0	-1.51	-188.0	-1.39
17	324606	-246.3	-1.43	-160.0	-0.93	-259.7	-1.51	-239.0	-1.39
19	362795	-316.7	-1.44	-202.7	-0.92	-335.3	-1.52	-304.0	-1.38
21	400984	-387.0	-1.44	-243.7	-0.91	-412.3	-1.53	-373.3	-1.39
23	439173	-462.7	-1.43	-290.7	-0.90	-493.0	-1.53	-446.3	-1.38
25	477362	-549.7	-1.44	-341.7	-0.90	-582.7	-1.53	-524.3	-1.38

Table C.3 Pressure values measured on pressure ports 9-11

Velocity (m/s)	Re	Port 9		Port 10		Port 11	
		ΔP_{avg}	C_P	ΔP_{avg}	C_P	ΔP_{avg}	C_P
3	57283	-3.3	-0.60	-2.7	-0.49	-7.7	-1.40
5	95472	-14.3	-0.94	-14.3	-0.94	-19.0	-1.25
7	133661	-32.0	-1.07	-28.7	-0.96	-36.0	-1.20
9	171850	-55.7	-1.08	-50.0	-0.97	-59.0	-1.14
11	210039	-75.3	-1.10	-67.0	-0.98	-80.0	-1.17
13	248228	-114.7	-1.11	-100.0	-0.97	-119.7	-1.16
15	286417	-150.3	-1.11	-132.0	-0.97	-158.3	-1.17
17	324606	-191.7	-1.11	-162.7	-0.95	-200.0	-1.16
19	362795	-245.0	-1.11	-207.7	-0.94	-256.3	-1.16
21	400984	-298.7	-1.11	-253.3	-0.94	-314.0	-1.17
23	439173	-356.3	-1.10	-300.3	-0.93	-374.7	-1.16
25	477362	-423.0	-1.11	-352.7	-0.93	-446.7	-1.17

Table C.4 Drag results for different velocities

Velocity (m/s)	Re	Series 1		Series 2		Series 3	
		F_D	C_D	F_D	C_D	F_D	C_D
5	95472	0.02	0.14	0.01	0.07	0.04	0.28
7	133661	0.08	0.28	0.08	0.28	0.10	0.35
9	171850	0.15	0.32	0.15	0.32	0.18	0.38
11	210039	0.23	0.33	0.24	0.34	0.26	0.37
13	248228	0.34	0.35	0.35	0.36	0.35	0.36
15	286417	0.46	0.35	0.48	0.37	0.46	0.35
17	324606	0.61	0.36	0.60	0.36	0.58	0.35
19	362795	0.73	0.35	0.74	0.35	0.74	0.35
21	400984	0.90	0.35	0.92	0.36	0.92	0.36
23	439173	1.09	0.36	1.08	0.35	1.10	0.36
25	477362	1.26	0.35	1.28	0.35	1.29	0.36

Table C.5 Drag results for different velocities-cont.

Velocity (m/s)	Re	Series 4		Series 5		Series 6	
		F _D	C _D	F _D	C _D	F _D	C _D
5	95472	0.07	0.48	0.07	0.48	0.07	0.48
7	133661	0.11	0.39	0.09	0.32	0.10	0.35
9	171850	0.18	0.38	0.17	0.36	0.17	0.36
11	210039	0.28	0.40	0.25	0.36	0.25	0.36
13	248228	0.38	0.39	0.34	0.35	0.36	0.37
15	286417	0.48	0.37	0.46	0.35	0.47	0.36
17	324606	0.59	0.35	0.61	0.36	0.59	0.35
19	362795	0.75	0.36	0.75	0.36	0.74	0.35
21	400984	0.92	0.36	0.90	0.35	0.91	0.36
23	439173	1.11	0.36	1.10	0.36	1.09	0.36
25	477362	1.30	0.36	1.26	0.35	1.29	0.36